SCUOLA
NORMALE
SUPERIORE

Quantum Transport in Wires and Nanoelectromechanical Systems

Ph.D. thesis

Stefano Pugnetti

Under the supervision of Prof. Rosario Fazio and Dr. Fabrizio Dolcini

Contents

Introduction

The rapid progress of nanotechnology has been of the utmost importance in modern Physics. Nanotechnology has an important role in the development of new electronic devices able to perform difficult tasks in increasingly short time, making it possible to realize faster and more sensitive detectors at larger scales. Additionally the high quality of the nanofabricated samples together with modern cooling techniques allows us to realize setups in which quantum mechanics can be used as a resource for performing specific tasks, therefore opening the field of quantum technology. In this latter spirit, nanodevices can also be regarded as a test-bed for quantum physics, in particular for those predictions regarding exotic states of matter such as entangled states or macroscopic superposition of states.

In probing the physics of nanodevices, an important role is played by transport measurements. Electric currents and potential can now be generated and detected with very high accuracy and sensitivity. Moreover fluctuations due to finite temperature can be reduced enough so that current and voltage fluctuations across a nanodevice can be used as a probe for the physics of the setup. Beside dc signals, alternate currents and voltages can be used to drive a device so that with transport one can also perform spectroscopic measurements.

In view of such new possibilities, in the present work we have studied several quantum properties of two different types of nanodevices that have been attracting much attention in the research community in the last few years because of their interest in both quantum technologies and fundamental physics: quantum nanowires and quantum NanoElectroMechanical Systems (referred to as NEMS). The probe employed in this study is that of transport, namely we study properties that can be inferred by measuring current-voltage characteristic curves or their derivatives in particular circumstances, giving, where possible, a physical interpretation of the results.

The first class of nanodevices focused on is that of quantum nanowires. The possibility of producing such devices is due to progress witnessed in nanolithographic technologies that dates back to the 1980's. Further advances in

the 1990's have allowed the production of new higher-quality samples based on several different kind of implementations, but all sharing common characteristics. In quantum nanowires, delocalized electrons of a metal or of a semiconducting material are restricted to move in a single direction due to strong confinement in the other two independent directions. It is now possible to realize nanowires of very high quality, with virtually no defects or impurities on the scale of 1μm; it also rather simple to cool such devices to temperatures below 100mK, where many interesting quantum effects can be tested.

One long-known issue related to conducting one-dimensional (1D) systems is the role of electron-electron interaction. In one dimension, the celebrated Fermi Liquid model for low-energy excitations in conducting materials breaks down, and electron-electron interaction modifies the low-energy picture of such systems in a dramatic way. For instance, the elementary excitations are no longer free fermionic quasi-particles, whose lifetime is longer the closer their energy is to the Fermi level, but rather free bosonic particle-hole excitations; indeed, as long as only low-energy phenomena are of interest, such bosonic excitations can be used to describe the whole Hilbert space of states and give therefore an *exact* representation of the spectrum of the system. The low energy physics of 1D interacting electrons is well described by the Tomonaga-Luttinger model.

While the theoretical picture of the physics of 1D systems can be considered satisfactory, experimental detection of Luttinger-liquid physics in quantum nanowires has long been elusive. In particular, first measurements of the conductance of quantum nanowires free of impurities have found a result compatible with that of a non-interacting system; this was rather unexpected, given the deep modifications interaction was known to bring about in 1D systems. However, a refinement of the Luttinger-liquid model, the so-called Inhomogeneous Luttinger Liquid model, taking into account in a more thorough way the physics of the leads, was able to explain such results for the conductance, opening the way to new studies about the physics of the charge transport in quantum nanowires.

The bosonic particle-hole excitations travel in a quantum wire at a speed that depends on the strength of electron-electron interaction. In the inhomogeneous-Luttinger-liquid model, interaction is taken to vary from a bulk value well inside the wire, to zero well inside the leads. A varying speed of propagation results in the partial reflection of the bosonic field at the position of the contacts. However, in clean wires the summation of all multiply-reflected waves produces no net effect and no backscattering is observed for electrons flowing through the leads. These reflections can be observed only if some localized impurity is present, as it seems correct to assume for a realistic

setup at the contacts. However, in the presence of weak contact impurities, reflection of electrons takes place also in a non-interacting wire, making it difficult to distinguish between the simple electron reflections (like in Fabry-Pérot cavities for photons) and bosonic field reflections (often referred to as *Andreev-like reflections*). In order to distinguish the two contributions to the transport, we propose and study a three terminal setup in which a tunnel probe faces an interacting quantum nanowire.

The second class of nanodevices that we study is that of nanoelectromechanical systems, another fruit of nanolithographic techniques. These devices are nanocircuits in which electrical degrees of freedom are coupled by some means to the position or velocity of some small object integrated on the chip, typically a cantilever or a microbridge. At very low temperatures the electrical degrees of freedom reach the quantum regime and quantum circuits have now been studied for many years. Beside their interest for fundamental physics, they also have important technological applications. On the one hand they are the hardware in many implementations for quantum computation; on the other hand, their quantum behavior has proven to be very useful for realizing new very sensitive detectors. Just to mention a few examples, the single-electron transistor and the superconducting quantum interference device (SQUID) are respectively among the most sensitive charge and flux detectors.

Reaching a good coupling between a nanomechanical oscillator and a coherent circuit allows the pursuit of different interesting results. First of all, if the quantum circuit is used as a sensitive detector, position and momentum of the nanomechanical oscillator can be monitored to a high degree of accuracy and some interesting predictions of quantum mechanics can be tested. Secondly, the feedback of the quantum circuit onto the nanomechanical oscillator can be used to cool it down, below the temperature of its environment. Finally, coupled quantum circuits and quantum nanomechanical oscillators can have applications in quantum computing (quantum buses and quantum memories based on quantum nanomechanical oscillators have been proposed). In view of the interest in coupled superconducting quantum NEMS, we study the coupled dynamics of a SQUID and a nanomechanical oscillator in both the classical and quantum regime.

Another aspect of the physics of nanomechanical resonators that has received much attention recently is the non-linear dynamics of these objects in both the classical and quantum regime. The nonlinearitity in a mechanical oscillator arises basically in two regimes: one in which the amplitude of the oscillations becomes so large that the non-linear part of the restoring force starts to play an important role and one in which the oscillator is coupled to a non-linear system. The latter configuration has been studied and the

quantum regime of an oscillator coupled to a coherent two-level system has been demonstrated. In view of the rapid progress in this field, in this thesis we propose an efficient scheme to detect the non-linearity of a mechanical oscillator in its quantum regime.

***

This thesis is divided in three parts. In the first part we address the effects of eletron-electron interaction in an interacting quantum wire with a third terminal. In chapter 1 we present a brief review of quantum transport in one-dimensional systems and introduce the bosonization technique to deal with interaction; we also introduce the inhomogeneous Luttinger liquid model. Chapter 2 is devoted to a detailed study of a setup made of an interacting nanowire with non-adiabatic contacts and a facing tunnel probe acting as a third terminal. In the second part we study the dynamics of two different superconducting nanoelectromechanical systems; more precisely we address the study of the classical and quantum coupled dynamics of a SQUID and a linear nanomechanical oscillator and the quantum dynamics of a non-linear oscillator coupled to a superconducting microwave cavity. In chapter 3 we give a brief introduction to nanomechanical systems and some detection techniques, with particular attention to those techniques involving detection via a superconducting circuit. Chapters 4 and 5 are devoted to the study of the coupled dynamics of a SQUID with an oscillating arm, in the classical and quantum regime respectively. In chapter 6 we describe an efficient scheme to demonstrate phonon blockade in a quantum non-linear mechanical oscillator by coupling it to a superconducting microwave cavity. The third part of this thesis comprises the appendices, where some technical details are given.

Part I

Quantum Transport Through Nanowires

Chapter 1

Transport in quantum wires

1.1 Coherence effects in transport

Electron transport in macroscopic conductors is governed by Ohm's laws:

1. The current I flowing through a sample is proportional to the voltage difference V applied to it: $I = GV$.

2. The propotionality constant G is directly proportional to the section S of the sample and inversely proportional to its length L: $G \propto \frac{S}{L}$.

This empiric relation can be given a theoretical account within Boltzmann's theory of transport. This theory treats charge carriers by introducing a function describing an average density over mascroscopic volumes of phase-space and deducing for it an evolution equation. The main ingredients of Boltzmann's theory are microscopic scattering rates and the thermal distributions of the concerned quantities. Thus, within this approach, only some aspects of quantum theory (such as the Pauli principle) are taken into account, while the wave-like nature of electrons is completely neglected. In this sense, electrical charges are treated as *semiclassical* particles.

As the size of the devices scales down, new experimental facts may arise that cannot be described by Boltzmann's theory. For instance, if the size of the sample is smaller than the momentum relaxation length l_m then charge carriers will move like free particles in a vacuum (*ballistic regime*), aside from some renormalization of their dynamical parameters. Momentum relaxation is due to scattering processes that can change the momentum of the carrier, such as impurity or phonon scattering; while l_m is reduced by such processes, electron-electron scattering produces no net change in the total momentum and hence it does not affect its relaxation length. The realization of high-mobility two-dimensional electron gases in semiconductor-based

heterostructures has made the ballistic regime easily achievable. The conductance G of a device has a fixed value when its length is less than l_m and does not grow indefinitely; this is a point in which Ohm's second law fails.

Another relevant length scale is the phase-relaxation length l_φ. By definition this is the length below which charge carriers may exhibit effects due to quantum interference. Indeed, when the device is phase-coherent the wave-like behaviour of the charge carriers becomes apparent (this could not be captured by Boltzmann's theory). If the total path of a charge carrier traversing the device is shorter than l_φ, then quantum interference becomes relevant for transport; in a non-ballistic sample an electron may undergo several scattering processes before reaching the end, in which case the total path can be much longer than the distance between the leads. Differently from what happens for l_m, the phase relaxation length is not affected by interactions with static scatterers; the relevant scattering processes determining l_φ are phonon scattering and electron-electron scattering, as well as inelastic impurity scattering.

A typical example of the effects of quantum coherence on transport can be found in two-path interferometers; they can be ring-shaped conductors contacted at two opposite points of the ring. The electron wave function is split as it enters the ring and the two parts follow different paths; if these are shorter then l_φ, then the probability of finding an electron at the end of the interferometer is $|\psi_1 + \psi_2|^2 = |\psi_1|^2 + |\psi_2|^2 + 2\Re\{\psi_1^* \psi_2\}$ where ψ_1 and ψ_2 are the wave functions of electrons travelling in arm 1 and 2 respectively. The last term of the r.h.s. oscillates as the relative phase of the two wave functions varies (this is apparent if one writes ψ_i in the form $e^{i\varphi_i(x)} f(x)$ where $\varphi_(x)$ is real and $f(x_{\text{out}})$ is also real). In a macroscopic system, where the sample size is much bigger than l_φ, the inelastic scattering randomizes the phase, so that this term effectively washes out. In contrast, in a system where phase coherence is preserved, said term is present and it directly affects the total electron transmission through the ring. The phase acquired when the two parts of the wave function reach the exit lead depends on the path: $\Delta\varphi_{1,2} = \int_{\gamma_{1,2}} \mathbf{k} \cdot \mathbf{dl}$, where $\mathbf{k}$ is the wave vector and $\gamma_{1,2}$ are the two paths. If a magnetic flux Φ threads the ring, then the vector potential $\mathbf{A}$ cannot be gauged away in all the space, and the phase difference gets an additional term $\int_{\gamma_{1,2}} \frac{e}{\hbar} \mathbf{A}(\mathbf{x}) \cdot \mathbf{dl}$. The phase difference then reads

$$\Delta\varphi_2 - \Delta\varphi_1 = \frac{e}{\hbar} \int_\gamma \mathbf{A} \cdot \mathbf{dl} = 2\pi \frac{\Phi}{\Phi_0} \tag{1.1}$$

where γ is the contour of the ring and $\Phi_0 = h/e$ is the flux quantum. Variations in Φ result in oscillations in the current flowing through the ring that

have a period Φ_0. This effect is completely parallel to the one seen in a Mach-Zender interferometer and is possible only in coherent devices.

In many cases, the study of transport in microscopic samples cannot be conducted relying only on a classical description of the system; in principle a complete quantum description may be required. We now briefly review the techniques we use in the present work to address the quantum description of a particular microscopic device, namely a quantum nanowire, which will be thoroughly described in the next chapter.

1.2 Landauer-Büttiker Theory

In many cases, a quantum description of transport can be gained by taking into account only single-particle effects, captured by the transmission and reflection coefficient for the process of traversing the device. In practice the sample is treated as a single fixed elastic scatterer. The crossing of the device can be represented by a scattering matrix that relates the outgoing states to the incoming states of the electrons; the relation between the currents flowing in each terminal of a conducting sample and the scattering matrix is known as the Landauer-Büttiker formula. This description applies, for instance, to the case of a ballistic conductor in which the charge carriers are considered to be non-interacting.[1]

An interesting point is how the geometry of the sample enters the calculation: it determines the free-particle states, both incoming and outgoing. Indeed if we think of the sample as a narrow rectangular region in a clean 2DEG, free states will be plane waves with quantized wave vector: $\psi = \exp\{i(k_x x + k_y y)\}$, $k_x = 2N\pi/L$ and $k_y = n\pi/W$ (L is the length of the sample, W its width, N and n are integers); the energy of the particle $\varepsilon_n = \hbar^2(k_x^2 + k_y^2)/2m$ varies with the transverse wave vector k_y, which can already have large values for low n, since π/W is large. Then it is customary to group these states into sub-bands, each of them corresponding to a fixed n (transverse mode), and with a parabolic dispersion relation $\varepsilon_n(k_x)$ between the energy and the longitudinal wave vector. If the sample is narrow enough, the energy separation between the bands can be so large that only the lowest transverse excitation number n is relevant for transport; this is the case, for example, if the voltage difference V across the device is smaller than the band separation: $eV < h^2/8mW^2$. In this regime both the in-coming and the outgoing states are parametrized by a single component (k_x) of the wave vector, so charge carriers behave as if they lived in a one-dimensional space.

[1] The range of applicability of this approach is discussed for instance in [1].

A difference in the Fermi levels of the two leads (say the right lead has a lower Fermi energy than the left lead) produces a current as a result of two unbalanced particle flows, one flowing from the left to the right and the other from the right to the left. For each electron leaving the right lead there is a corresponding electron on the left lead, but that is not true for left-lead electrons with energy between μ_R and μ_L; those unbalanced electrons result in a net current

$$I = \frac{2e^2}{h} T(\mu_L - \mu_R) = G(\mu_L - \mu_R) \tag{1.2}$$

Where T is the transmission probability for the scattering process inside the device. Note that the conductance is finite even in the case of perfect transmission and that the result does not depend on the length of the sample, so in this case we have a breakdown of Ohm's second law; moreover the conductance as a function of width is not linear, but rather proceeds in steps of height $2e^2/h$ (the factor 2 is due to the two possible spin states available to the charge carrier, while e^2/h is called the *conductance quantum*). This is because as each sub-band enters the transport, it contributes a single quantum to the total conductance; again this is a failure of Ohm's second law. Eq. (1.2) is known as Landauer's formula, and it can be generalized to the case in which several sub-bands are involved in both leads. A further extension, due to Büttiker, takes into account a situation in which more terminals face the sample:

$$I_i = \frac{2e}{h} \int d\varepsilon \sum_j |S_{i,j}|^2 [f_j(\varepsilon) - f_i(\varepsilon)] \tag{1.3}$$

where $S_{i,j}$ is the scattering matrix relating the outgoing state of lead i to the incoming state of lead j and f_i is the thermal energy distribution of electrons in lead i. Here only one sub-band has been considered for each terminal.

In the case of two terminal devices, the formalism of Landauer-Büttiker formula is quite practical for composite scattering. As an example we study the conductance of a one-dimensional single-channel sample with two impurities at a distance L. The impurities will be modeled with a repulsive δ potential. To each impurity one can associate a scattering matrix; eventually one can easily combine all of these matrices. The single-particle Hamiltonian for a single impurity reads:

$$H = \frac{p^2}{2m} + \Lambda\delta(x) \tag{1.4}$$

If one looks for solution of the form:

$$\psi(x) = \begin{cases} a_L e^{ikx} + b_L e^{-ikx} & x < 0 \\ a_R e^{-ikx} + b_R r^{ikx} & x \geq 0 \end{cases} \tag{1.5}$$

then the scattering matrix S relates the coefficients of the solution:

$$\begin{pmatrix} b_R \\ b_L \end{pmatrix} = S \begin{pmatrix} a_R \\ a_L \end{pmatrix} \tag{1.6}$$

At this stage however it is more useful to evaluate the transfer matrix T defined by:

$$\begin{pmatrix} b_R \\ a_R \end{pmatrix} = T \begin{pmatrix} a_L \\ b_L \end{pmatrix} \tag{1.7}$$

The reason for doing this is that with a transfer matrix we can connect the states at the right of one scatterer with those at the left of the next; if, as in our example, there are more than one scatterer it is sufficient to multiply the transfer matrices of each one. This of course would not be the case for the scattering matrix. For a δ-like impurity one finds:

$$T_\Lambda = \begin{pmatrix} 1 - i\frac{m\Lambda}{\hbar^2 k} & -i\frac{m\Lambda}{\hbar^2 k} \\ i\frac{m\Lambda}{\hbar^2 k} & 1 + i\frac{m\Lambda}{\hbar^2 k} \end{pmatrix} \tag{1.8}$$

The transfer matrix for an impurity placed at a distance L from the origin can be found simply by transforming T_Λ according to a translation in the coordinate axis $x \to x - L$:

$$T'_\Lambda = \begin{pmatrix} e^{-ikL} & 0 \\ 0 & e^{ikL} \end{pmatrix} T_\Lambda \begin{pmatrix} e^{ikL} & 0 \\ 0 & e^{-ikL} \end{pmatrix} \tag{1.9}$$

The total transfer matrix is $T = T'_{\Lambda_2} T_{\Lambda_1}$. The scattering matrix can be recovered from:

$$S = \frac{1}{T_{22}} \begin{pmatrix} T_{12} & 1 \\ 1 & -T_{21} \end{pmatrix} \tag{1.10}$$

where we have used $\det T = 1$. In this case the scattering matrix depends on the energy through the wave vector $k = \sqrt{2m\varepsilon/\hbar^2}$. Using Eq. (1.3) we can see that the zero-temperature differential conductance dI/dV is simply:

$$\frac{e^2}{h} |S_{21}(\varepsilon_F + eV)|^2 \tag{1.11}$$

The transmission coefficient is quasi-periodic in k and resembles that of a Fabry-Pérot interferometer, with peaks in correspondence of values of the wave vector that are resonant with the "cavity" formed by the two impurities (see Fig. 1.1).

Landauer-Büttiker formula is a very useful tool for describing transport through many kinds of systems. However, it has long been know that in one-dimensional (or quasi one-dimensional) systems, as in quantum wires,

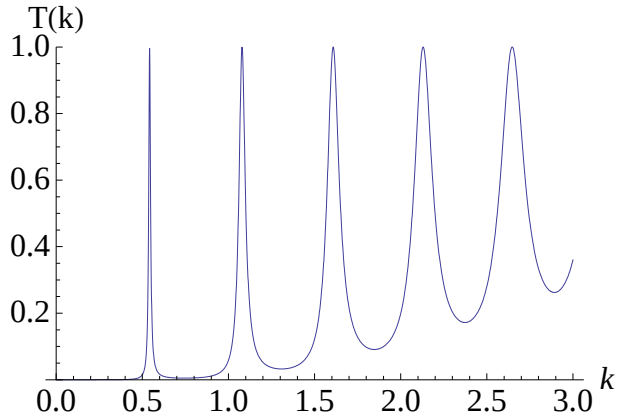

Figure 1.1: Transmission coefficient of a ballistic conductor with two impurities; the wave vector is expressed in units of $2\pi/L$ and the rescaled impurity strength is $\lambda = 2\pi 2m\Lambda/\hbar^2 L = 2$.

electron-electron interaction *does* matter, and Landauer-Büttiker formula cannot be used. Therefore, in order to describe transport through an interacting quantum wire, we now introduce a different formalism that is more suitable to deal with the peculiar nature of interactions in 1D systems.

1.3 Interactions in one-dimensional electron systems

In bulk 2D and 3D materials Coulomb interaction can be dealt with within the Fermi Liquid model, and the excitations of the system can be described as weakly interacting fermionic quasi-particles, which are in one-to-one correspondence with the single-particle states of a non-interacting system. This is the reason why describing a metal as a system of independent electrons is successful. This is not the case for any interacting one-dimensional system.

One can picture this through the following classical example: while in 2 and 3 dimensions hard-core particles can move in a specific direction avoiding each other, in one dimension this is not possible and a moving particle must push its neighbours forward in order to proceed. What happens is that single-particle excitations rapidly decay into collective plasmonic modes; transport in 1D systems occurs through charged phonon-like quasi-particles. Another argument showing that the concept of particle-like excitation is not ideal for describing low-energy phenomena is that particle-hole excitations have a well defined energy-momentum relation, and can therefore be used

to describe the low-energy sector of the excitation spectrum. To see this, one can consider the energy of a particle-hole excitation in a non-interacting system, obtained by removing a particle in a state with momentum $\boldsymbol{k'}$ and energy $E(\boldsymbol{k'})$ (slightly below the Fermi energy), and adding a particle in a state with momentum $\boldsymbol{k}$ and energy $E(\boldsymbol{k})$ (slightly above the Fermi energy). In 1D systems, after linearizing the dispersion relation, one finds that $E(k) - E(k') = |E'(k_F)|(|k| - |k'|)$ (assuming that the Fermi velocity be the same in the two Fermi points); this can be considered as a definite energy-momentum relation, both if k and k' are close to the same Fermi point, and if they are close to opposite points; this is a hint of the fact that in 1D particle-hole excitations are good candidates for representing the excitation spectrum as quasi-particles, in much the same way as particle-like excitations in a Fermi Liquid. This fact is peculiar of 1D systems, since in two or more dimensions low-energy particle-hole excitations can have momenta of any modulus between $|\boldsymbol{k}| - |\boldsymbol{k'}|$ and $|\boldsymbol{k}| + |\boldsymbol{k'}|$.

One can show that a model Hamiltonian, the Tomonaga-Luttinger model, can describe the low-energy properties of electronic 1D systems in an appropriate way, differently from what is possible with the Fermi Liquid model. In the case of short range interactions, such as screened Coulomb interaction in gated wires, the Tomonaga-Luttinger model is parametrized by a single quantity g: $g = 1$ corresponds to a non-interacting system (Fermi gas), $g > 1$ corresponds to attractive interactions while $g < 1$ corresponds to repulsive interaction. As an example consider Carbon Nanotubes: by now they can be efficiently contacted with metallic leads in order to perform transport measurements; there are indications that these systems act like Luttinger Liquids with strong interactions ($g = 0.3$) [2].

In the remaining part of this chapter, we give a quick overview on the formalism needed to deal with the Tomonaga-Luttinger model and on a few facts relevant for contextualizing our work; further technical details are given in the appendices.

1.4 Bosonization

The Luttinger liquid model deals with the low-energy excitations of a one-dimensional fermionic system, in much the same way as the Fermi liquid theory does for higher dimensional systems. In order to introduce the basic tool for dealing with the Luttinger model, namely bosonization, we first introduce some simplifications and definitions that apply to non-interacting 1D Fermi systems.

A key simplification for building a low-energy model of a uniform 1D

fermionic system is to replace the one-particle energy-momentum (dispersion) relation $E(p)$ by a linearized version $E_F + dE(\pm p_F)/dp\,(p \pm p_F)$ (depending on which of the two Fermi points $\pm p_F$ the state labelled by p is close to). In higher dimensional systems, the Fermi velocity $\boldsymbol{v_F} = \boldsymbol{\nabla_p} E(\boldsymbol{p_F})$ depends on the direction within the p-space, so that the linearization procedure is not quite so simple.

The linearization procedure produces two distinct dispersion relations, one corresponding to a particle moving at velocity v_F and the other to a particle moving with velocity $-v_F$. It is natural then to introduce two kind of particles, each characterized by one of the two dispersion relations; this can be done, for instance, at the level of the fermionic field operator by writing:

$$\Psi(x) \simeq e^{ik_F x}\Psi_R(x) + e^{-ik_F x}\Psi_L(x)\,. \tag{1.12}$$

Each chiral field is defined in such a way as to have only low-wavelength components:

$$\Psi_r(x) = \sum_{|k|<1/\Lambda} e^{irkx} a_{r,k}\,, \qquad r = R, L = +1, -1\,. \tag{1.13}$$

The truncation of the sum is usually done by replacing $\sum_k$ with $\sum_k e^{-\Lambda|k|/2}$ and taking the limit $\Lambda \to 0$ as the last step of a calculation. The physical meaning of this procedure is that linearization of the dispersion relation can only be used to reproduce the low-energy physics of the systems; therefore, everything that comes from states with high $|k|$ is outside the scope of the model.

The second quantized form of a free fermion Hamiltonian in the approximation of linear dispersion is:

$$H = \int dx \sum_r \hbar v_F r\, :\Psi_r^\dagger(x)(-i\partial_x)\Psi_r(x):\,, \tag{1.14}$$

where $:\ldots:$ denotes the normal ordering of the product within the colons; in this context, the normal-ordered version of a product of operators is the difference between the product in the original order and its expectation value on a state called the "Fermi sea", *i.e.* a state in which all the single-particle states below the Fermi energy are occupied, while the others are empty. This complication is necessary because of the linearization procedure; indeed a Hamiltonian with a linear dispersion relation in a system with unbounded k is not bounded from below.

For analogous reasons, the electron density is better defined as a difference with respect to the ground state density. A key property of 1D systems

with a linear spectrum is the fact that, although direct calculation of the commutator of the density operator at different points yields zero, taking its average over the ground state for an infinite number of particles produces a non-zero result (this is the so-called *anomalous commutator*). To show this, one can first compute the density correlation function:

$$\begin{aligned} J_r(x,t) =& \langle T\{\Psi_r^\dagger(x,t)\Psi_r(x,t)\Psi_r^\dagger(0,0)\Psi_r(0,0)\}\rangle = \\ \simeq& \langle T\{\Psi_r^\dagger(x,t)\Psi_r(0,0)\}\rangle\langle T\{\Psi_r(x,t)\Psi_r^\dagger(0,0)\}\rangle = \\ =& -iG_r(-x,-t)iG_r(x,t) \end{aligned} \tag{1.15}$$

(on the second line, diverging terms have been dropped since they represent an artifact of the linearization procedure); the Green's function $G_r(x,t)$ is defined as:

$$\begin{aligned} G_r(x-x',t-t') \equiv& (-i)\langle T\{\Psi_r(x,t)\Psi_r^\dagger(x',t')\}\rangle = \\ =& \lim_{\Lambda\to 0^+} \frac{1}{2\pi}\frac{1}{rx - v_F t + i\Lambda\,\mathrm{sgn}(t)}\,. \end{aligned} \tag{1.16}$$

The final result is:

$$\begin{aligned} [:\Psi_r^\dagger(x)\Psi_r(x):, :\Psi_r^\dagger(x')\Psi_r(x'):] =& \lim_{t\to 0^+}[J_r(x-x',t) - J_r(x-x',-t)] = \\ =& -\frac{ri}{2\pi}\partial_x\delta(x-x')\,. \end{aligned} \tag{1.17}$$

The anomalous commutator of the density operator reflects the fact that in one-dimensional fermionic systems the low energy excitations are of particle-hole type. Eq. (1.17) is the starting point for demonstrating a very useful relation that holds for one-dimensional systems with a linear spectrum, namely the bosonization identity. It aims at describing all the properties of this simplified model in terms of a bosonic field representing particle-hole excitations; this new field replaces the standard electron field.

Let us first consider the fields

$$\Phi_r(x) = \sqrt{\pi}\int_{x_{\min}}^{x} :\Psi_r^\dagger(x')\Psi_r(x'):\, dx'\,; \tag{1.18}$$

due to the anomalous commutator, they obey the following commutation relations:

$$[\Phi_r(x), \Phi_r(x')] = -\frac{ir}{2}\theta(x'-x)\,. \tag{1.19}$$

Because of Eq. (1.19), the commutator of Φ_r and Ψ_r, namely

$$[\Phi_r(x), \Psi_{r'}(x')] = -\sqrt{\pi}\theta(x-x')\Psi_r(x')\,, \tag{1.20}$$

can be exactly reproduced if one takes:

$$\Psi_r(x) = e^{ir\sqrt{4\pi}\Phi_r(x)} \tag{1.21}$$

However, Eq. (1.21) cannot be correct as an operator identity, because the two sides of the equation have different commutation properties with respect to the number operator N; indeed, the left-hand side acts as a lowering operator for the electrons, whereas the right-hand side does not. One can show (see for instance [3, 4]) that the correct version of identity (1.21) is

$$\Psi_r(x) = \frac{\kappa_r}{\sqrt{2\pi\Lambda}} e^{ir\sqrt{4\pi}\Phi_r(x)}\,, \tag{1.22}$$

where the *Klein factor* κ_r is defined as an operator that decreases the number of particles by unity and commutes with all of the bosonic operators. In order to reproduce the correct dynamics, one has to specify the Hamiltonian of the new field. This is better done for the combination:

$$\Phi(x) = \Phi_L(x) + \Phi_R(x)\,; \tag{1.23}$$

the field

$$\Pi(x) = \partial_x[\Phi_L(x) - \Phi_R(x)] \tag{1.24}$$

obeys the commutation relation of the field conjugate to Φ. Moreover one has:

$$\partial_t\Phi(x,t) = -v_F(-\partial_x\Phi_L + \partial_x\Phi_R) = v_F\Pi \tag{1.25}$$

It can be shown that the Hamiltonian is:

$$H_\Phi = \frac{\hbar v_F}{2}\int dx\left\{\Pi(x)^2 + [\partial_x\Phi(x)]^2\right\}\,, \tag{1.26}$$

and that Φ and Π are conjugate fields. The physical interpretation of these two fields is rather straightforward.

$$\frac{1}{\sqrt{\pi}}\partial_x\Phi = \sum_r :\Psi_r^\dagger\Psi_r: \tag{1.27}$$

is the long-wavelength component of the normal-ordered density, whereas

$$-\frac{v_F}{\sqrt{\pi}}\Pi = v_F\sum_r r :\Psi_r^\dagger\Psi_r: \tag{1.28}$$

is the long-wavelength component of the normal-ordered current.

A general two-body interaction is usually taken into account by including an interaction term in the Hamiltonian:

$$H_{\text{int}} = \frac{1}{2}\int dx dx' \Psi^\dagger(x)\Psi^\dagger(x')U(x-x')\Psi(x')\Psi(x)\,. \tag{1.29}$$

It turns out that for describing the physics involving only low energy scales it suffices to retain only long-wavelength components of the interaction potential. Therefore, H_{int} can be written in term of ρ_r only:

$$H_{\text{int}} \approx \frac{1}{2\pi}\int dx dx' \partial_x\Phi(x)U(x-x')\partial_{x'}\Phi(x')\,. \tag{1.30}$$

Moreover, U is usually taken to be short-ranged; the physical motivation for this is the usual presence of a metallic gate facing the device where the 1D system is realized and screening electric fields (this is true in particular for quantum nanowires). Taking this into account by writing $U(x-x') = U_0\delta(x-x')$, one eventually finds:

$$H = \frac{\hbar v_F}{2}\int dx \left\{\Pi(x) + \left(1+\frac{U_0}{\hbar\pi v_F}\right)\left[\partial_x\Phi(x)\right]^2\right\} \tag{1.31}$$

Eq. (1.31) means that all the effects of a short-ranged interaction between electrons in the low-energy physics of a 1D system are captured by a single parameter, usually defined as

$$g = \sqrt{\frac{1}{1+\frac{U_0}{\hbar\pi v_F}}}\,, \tag{1.32}$$

and that they do not change the description of the system as one of free bosons. However, the parameter g renormalizes many standard thermodynamic quantities, such as compressibility.

The fact that the Hamiltonian remains quadratic in the bosonic fields depends on two assumptions that we have taken: 1) we neglect spin, *i.e.* we take the charge carriers to be fully polarized; 2) we are interested only in the low-energy processes. With these two assumptions it can be shown that the terms we retained are the only ones that matter. In principle, density-density interaction could also produce backscattering of charge carriers, from one side of the dispersion relation to the other side; moreover, if the spin can vary, then there are also spin-flip terms. Both of these types of processes would be described by terms which are not simply quadratic and in this case the model would be no longer exactly solvable. However, in our case the Hamiltonian is quadratic in the bosonic fields and this is one of the key ingredients of the success of the Tomonaga-Luttinger paradigm. Indeed, the

model describes interaction between electrons, no matter how strong they are, effectively as just a reparametrization of the free-boson Hamiltonian. In the language of second quantization, one can show that the interacting Hamiltonian is quadratic in the creation and annihilation operators of the original bosonic field; upon a Bogolioubov transformation, one can turn the interacting Hamiltonian into a non-interacting one for new creation and annihilation operators that are related to the previous ones by a linear transformation. This means that right- and left-moving plasmonic excitations are no longer the most elementary excitations of the system, for these are rather a linear combination of right- and left-moving excitation.

1.5 Transport in interacting wires

In the next chapter we will apply the Tomonaga-Luttinger model to study transport in a setup comprising an interacting quantum wire. Therefore we now briefly sketch some basic results of the physics of transport through Luttinger liquids.

As we have seen in the previous section, a consequence of interaction is that elementary excitations are a superposition of right- and left-moving charge carriers. In view of this fact, one should expect that injection of right- or left-moving excitation into a Luttinger Liquid (such as an electron tunnelling in from one lead) might result in a creation of both right- and left-moving excitation, what could be interpreted as a backscattering.

Applying Kubo's linear-response theory, one can compute the linear conductance of an interacting Luttinger liquid with no impurities in the limit of low bias voltage. A static voltage contributes a term

$$H_{\text{pot}} = \int dx V(x) \frac{e}{\sqrt{\pi}} \partial_x \Phi(x) \tag{1.33}$$

to the Hamiltonian of the system; here $V(x)$ is the electrical potential and e is the (negative) charge of the electron. Therefore, the zero-temperature average current reads:

$$I(x,t) = -\frac{e v_F}{\sqrt{\pi}} \langle \Pi(x,t) \rangle \simeq -\frac{e^2 v_F}{\pi} \frac{i}{\hbar} \int_{-\infty}^{t} dt' \int dx' V(x') \langle [\partial_{x'} \Phi(x',t'), \Pi(x,t)] \rangle \,. \tag{1.34}$$

Following Mahan[5], the advanced correlation function $i\theta(t-t')\langle[\Phi(x',t'),\Pi(x,t)]\rangle$ can be computed from the expression of the temperature Green's function

$$\mathscr{G}(x',x;\tau) = -\langle T_\tau(\Phi(x',\tau)\Pi(x,0))\rangle \tag{1.35}$$

by means of the analytic continuation $i\omega \to \omega - i0^+$ of its Fourier transform $\tilde{\mathscr{G}}(x', x; \omega)$, which in turn can be computed by noticing that it is a solution of the problem:

$$\begin{cases} \left(-\omega^2 + \dfrac{v_F^2}{g^2}\partial_{x'}^2\right)\tilde{\mathscr{G}}(x', x; \omega) = \omega\delta(x' - x) \\ \dfrac{v_F^2}{g^2}\partial_{x'}\,\tilde{\mathscr{G}}(x', x; \omega)\Big|_{x=+x-\epsilon}^{x'=x+\epsilon} = \omega \end{cases} . \tag{1.36}$$

The final result is

$$i\theta(t - t')\langle[\Phi(x', t')\Pi(x, t)]\rangle = \lim_{\epsilon\to 0^+} \frac{1}{2}\frac{g}{v_F}\delta\left(t' - t + \frac{g}{v_F}|x' - x|\right) e^{-\epsilon\frac{g}{v_F}|x'-x|} \tag{1.37}$$

and

$$I(x, t) = g\frac{e^2}{h}\int dx'\partial_{x'}V(x') = g\frac{e^2}{h}[V(+\infty) - V(-\infty)]\,. \tag{1.38}$$

This result shows that the conductance of an interacting Luttinger liquid with no impurity is renormalized by interaction, and should no longer be e^2/h, the quantum of conductance. The reduction of the conductance with respect to a non-interacting system can be interpreted as a consequence of the backscattering introduced by interaction: since elementary excitations have no definite right- or left-moving character, injection of a (say) right-moving electron results in a creation of both right- and left-moving excitations and this fact leads to a reduction in the current, even in the absence of backscattering impurities.

However, the first accurate measurements of the conductance of clean nanowires revealed a mismatch between the value of g measured through the conductance and the one measured by other means[6]. In particular the conductance of clean wires was found to be consistent with the value $2e^2/h$, the theoretical result for ballistic non-interacting quasi-1D devices (taking into account electronic spin).

1.6 Effects due to the leads

The solution to this puzzle was found by I. Safi and H. Schulz [7] and also by other researchers independently [8, 9]. The key is in taking into consideration the effects of the leads, an aspect that the naïve calculation of section 1.5 did not take into account. In fact, the leads cannot be considered as interacting 1D systems since their transverse dimensions must eventually increase untill

they start behaving as bulk conductors; interactions then result in the usual Fermi-liquid picture. Within the language of the Tomonaga-Luttinger model, they can be modeled in an effective way as non-interacting wires. Technically, this means that the interaction parameter g in the Hamiltonian is to be taken as a function $g(x)$ of the position and must equal 1 in the leads while it should be different from 1 well inside the wire. A non-uniform value of g can also be a consequence of a particular geometry of the gate that screens the interactions in the wire.

A sharp change in the width of the wire or the geometry of the gate will in general result in some backscattering at the position of the sudden change. Therefore, in order to describe a clean wire attached to non-interacting leads through transparent contacts, one should in principle take $g(x)$ to be a smooth function of position. However, for the sake of simplicity and as a first approximation, in the literature $g(x)$ has been taken to be piecewise constant, with steps at the positions of the leads; this approximation has been shown to be good enough to explain the value of the conductance.

In [7] it has been shown that by taking

$$g(x) = \begin{cases} 1 & \text{for } |x| > L/2 \\ g & \text{for } |x| < L/2 \end{cases} , \tag{1.39}$$

(L is the wire's length and the origin of the x axis is in the middle of the wire) the field Φ is reflected at the interface between the lead and the interacting wire, with a reflection coefficient

$$\gamma = \frac{1-g}{1+g} . \tag{1.40}$$

This fact has a simple interpretation for $g > 1$, *i.e.* for attractive interactions; in this case one finds $\gamma < 0$, namely, a positive charge impinging on the contact is reflected as a negative charge. Since for $g > 1$ the electrons in the wire have a tendency to pairing, one can interpret this as an instance of Andreev reflection, the reflection of an electron as a hole at the interface between a normal conductor and a superconductor. Following this interpretation, one names this reflection of the field Φ *Andreev-type reflection*, even when $g < 1$. One has to keep in mind, however, that Andreev-type reflection in inhomogeneous Luttinger liquids is not the reflection of an electron into an electron or into a hole; indeed the amount of charge that is reflected is usually different from the electron charge.

In [7] it was shown that when the two contacts are taken into account, in the absence of backscattering impurities, the sum of all the partially reflected waves amounts to zero, no matter what the value of g is; in other words, all

of the charge impinging on the wire is completely transmitted, so that the conductance of an nanowire with non-interacting leads is the same for interacting and non-interacting wires. This is an explanation of the experimental results in [6], despite the apparently rough approximation of a step-like $g(x)$ function.

***

Although the inhomogeneous Luttinger-Liquid model correctly describes the transport properties in clean wires, the question arises whether these Andreev-like reflections can be directly revealed by some measurements. The case of a wire with a single δ-like impurity has been addressed in [10] and it was proved that the current-voltage characteristic of the device features some oscillations that are related to Andreev-like reflection. This indicates that wires with non-adiabatic contacts may exhibit some interesting features as well. However, in two-terminal devices with non-adiabatic contacts oscillations in the conductance due to quantum interference (as in Fabry-Pérot interferometers) occurs as well, and since these are present also in non-interacting systems, these devices are not ideal for measuring effects specific to interacting systems.

In the following we show what happens when a third terminal faces a quantum wire with non-adiabatic contacts; we study the case of a tunneling junction, which is a good description, for example, of what happens when the tip of a Scanning Tunnel Microscope is used to scan a quantum wire.

Chapter 2

Electron tunneling into a quantum wire in the Fabry-Pérot regime

Electron scanning of a conductor with a probe terminal is a customary technique for investigating its local properties. The local density of states can be gained from the dependence of the tunneling current on the applied bias. Nowadays, atomically resolved images are obtained both with scanning tunnel microscopes (STM) and atomic force microscopes (AFM).[11, 12, 13, 14, 15] So far, most of the efforts of the scientific community have focused on improving the resolution power of the probe terminal. For instance, the recent realization of stable and sharp superconducting STM tips exploits the singularity in the quasiparticle density of states to this purpose.[16, 17, 18, 19] A probe terminal, however, may also be used as a "handle", *i.e.* as an active component to tune the transport properties of the conductor. Recent works in this direction have shown that the sign of the supercurrent can be changed when a third terminal injects electrons into a Josephson junction under appropriate conditions [20, 21, 22, 23, 24, 25], that the conductance of a quantum dot can be tuned by moving an AFM tip over the sample [26], or that a single-electron transistor can be used to cool down a nanomechanical resonator, or to drive it into a squeezed state [27, 28].

The promising applications of scanning probes in the study of transport properties of nanodevices require a theoretical analysis of electron transport in a three-terminal set-up, a subject which thus far has been only partially explored. In particular, most of the available investigations are restricted to the case of non-interacting conductors[29, 30, 31, 32, 33, 34], whereas relatively little attention has been devoted to those nanodevices in which electronic correlations play a dominant role. This is the case for one-dimensional (1D)

conductors, such as semiconductor heterostructure quantum wires [35, 36] and single-walled carbon nanotubes [37, 38]. There, electron-electron interaction dramatically affects the dynamics of charge injection. The response of the system to the scanning probe is quite different from that of ordinary three dimensional metals, since in 1D electronic correlations lead to a breakdown of the Fermi liquid picture. Semiconductor quantum wires and carbon nanotubes rather exhibit Luttinger liquid (LL) behavior [39, 40, 41, 42, 2, 43, 44]. While for this type of system two-terminal electron transport has been widely analyzed in the last 15 years[35, 36, 37, 39, 40, 41, 42, 2, 43, 38, 44], the electric current and noise in a three-terminal set-up, including source and drain electrodes and a tip, have remained mostly unexplored.

There are, however, a few notable works in this direction. The case where a bias is applied between a tip and a semi-infinite LL was investigated by Eggert [45], and by Ussishkin and Glazman [46]. Martin and co-workers [47, 48] have recently analyzed the electric noise of the current injected from a tip into a nanotube adiabatically contacted at each end to grounded metallic leads.

In this chapter we extend these investigations to a quite general three-terminal set-up. We shall thus explore the non-equilibrium current in all three terminals in presence of a transport voltage between the source and drain electrodes, an applied tip voltage, and also a tunable gate voltage. This enables us to address various physical phenomena that are of relevance for recent experiments. Among other effects, we discuss the influence of the tip on the transport along the interacting wire, even when no net current is injected from the tip into the wire. In particular, we focus on the Fabry-Pérot transport regime of the wire, which could be recently observed in carbon nanotubes [38, 44, 49, 50], and analyze how Fabry-Pérot oscillations are modified by both the presence of the tip and the electron-electron interaction. To this purpose, the finite length of the wire, the contact resistances at the interfaces between the wire and the side electrodes, as well as an arbitrary position of the tip along the 1D wire are taken into account in our model. Furthermore, inspired by recent experiments on semiconductor quantum wires [41, 42, 51], we allow for an asymmetry in electron tunneling from the tip, and investigate how the presence of side electrodes affects the fractionalization of charges injected by the tip into an interacting wire. Finally, regarding the experimental observation of interaction effects, we discuss the advantages of a three-terminal set-up over a two-terminal one.

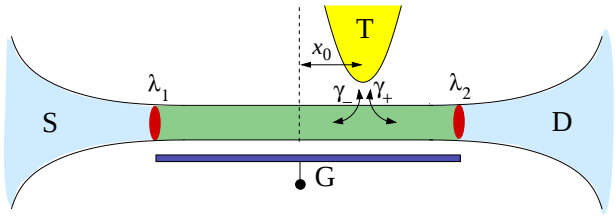

Figure 2.1: A sketch of the typical setup we want to model. A quantum wire (green area) is connected to a source and a drain electrode, made of non-interacting metals (depicted in light cyan). Two further electrodes are present: an extended gate (in blue) and a localized tunnel tip (in yellow). The picture further illustrates the asymmetric tunnel coupling between the tip and the wire (see the text for a definition of γ_+ and γ_-) and the presence of scattering impurities at the contact with respective strength λ_1 and λ_2 (again, see the text for a definition).

2.1 The model

We consider a single channel spinless quantum wire connected, as sketched in Fig. 2.1, to two metallic electrodes, source (S) and drain (D), as well as to a third sharp electrode, henceforth denoted as tip (T). The wire has a finite length L and for the x coordinate along it we choose the origin in the middle of the wire so that the interfaces to the S and D electrodes are located at $x_1 = -L/2$ and $x_2 = +L/2$, respectively. Electron backscattering at the side contacts due to non-adiabatic coupling is modeled by two delta-like scatterers. The tip is described as a semi-infinite non-interacting Fermi liquid, and $y \leq 0$ denotes the coordinate axis along the tip orthogonal to the wire, the origin corresponding to the injection point on the tip. The latter is located at position x_0 with respect to the middle of the wire, and electron injection is modeled by a tunnel Hamiltonian. We also envisage the presence of a metallic gate (G), biased at a voltage V_G. Screening by this gate yields an effectively short-ranged electron-electron interaction potential within the wire, for which the LL model applies.[1] [7, 8] The total Hamiltonian of the system reads

$$\mathcal{H} = \mathcal{H}_W + \mathcal{H}_T + \mathcal{H}_{tun} \tag{2.1}$$

where the first term describes the wire and its coupling to the S and D electrodes as well as to the gate. The second term accounts for the tip, and the last one describes wire-tip tunneling.

[1] Due to the effectively short-ranged interaction induced by the gate, a Wigner crystal regime does not arise in the situation discussed here.

As far as the wire is concerned, we shall address here the low-energy regime, where the wire electron band can be linearized around the Fermi level. Then the wire electron operator $\Psi(x)$ can be decomposed into right- and left-moving components $\Psi_+(x)$ and $\Psi_-(x)$

$$\Psi(x) = \mathrm{e}^{+ik_{\mathrm{W}}x}\Psi_+(x) \,+\, \mathrm{e}^{-ik_{\mathrm{W}}x}\Psi_-(x) \tag{2.2}$$

where k_{W} denotes the equilibrium Fermi momentum of the wire. By definition, this is the Fermi momentum when the electrochemical potentials of all electrodes, source, drain, tip and gate, are identical. This corresponds to vanishing applied voltages. Explicitly the Hamiltonian of the wire reads

$$\mathcal{H}_{\mathrm{W}} = \mathcal{H}_{\mathrm{kin,W}} \,+\, \mathcal{H}_{\lambda} \,+\, \mathcal{H}_{\mu_{\mathrm{W}}} \,+\, \mathcal{H}_{U}\,. \tag{2.3}$$

In Eq. (2.3) the first term

$$\begin{aligned}\mathcal{H}_{\mathrm{kin,W}} \;\; = \;\; -i\hbar v_{\mathrm{W}} \int_{-\infty}^{\infty} dx \,\Big[&: \Psi_+^{\dagger}(x)\partial_x\Psi_+(x) : - \\ &- : \Psi_-^{\dagger}(x)\partial_x\Psi_-(x) :\Big]\end{aligned} \tag{2.4}$$

describes the band energy linearized around the wire Fermi points $\pm k_{\mathrm{W}}$ and characterized by a Fermi velocity v_{W}. The symbol : : stands for normal ordering with respect to the equilibrium ground state. The second term models scatterers at the interfaces [52, 53] with the S and D electrodes

$$\mathcal{H}_{\lambda} = \hbar v_{\mathrm{W}} \sum_{i=1,2} \lambda_i \rho(x_i) \tag{2.5}$$

where the dimensionless parameters $\lambda_i \geq 0$ denote the impurity strengths at the contacts x_i, and the term $\rho(x)=\, :\Psi^{\dagger}(x)\Psi(x):$ is the electron density fluctuation with respect to the equilibrium value. The third term in Eq. (2.3),

$$\mathcal{H}_{\mu_{\mathrm{W}}} = \int_{-\infty}^{+\infty} \mu_{\mathrm{W}}(x)\rho(x)\, dx \tag{2.6}$$

with

$$\mu_{\mathrm{W}}(x) = \begin{cases} eV_{\mathrm{S}} & \text{for } x < -L/2 \\ eV_{\mathrm{G}} & \text{for } -L/2 < x < L/2 \\ eV_{\mathrm{D}} & \text{for } x > L/2 \end{cases}, \tag{2.7}$$

accounts for the bias V_{S} and V_{D} of the source and drain electrodes, as well as for the gate voltage V_{G}. The applied transport voltage is then $V = V_{\mathrm{S}} - V_{\mathrm{D}}$. Finally, the last term

$$\mathcal{H}_{U} = \frac{U}{2} \int_{-L/2}^{L/2} dx \sum_{r,r'=\pm} : \rho_r(x)\rho_{r'}(x) : \tag{2.8}$$

describes the screened Coulomb interaction in the wire,[7, 8] where $\rho_r(x) = :\Psi_r^\dagger(x)\Psi_r(x):$ is the density fluctuation of r-moving electrons. As is customary in LL theory, in the sequel, we characterize the interaction strength by the dimensionless coupling constant

$$g = \left(1 + \frac{U}{\pi\hbar v_{\rm W}}\right)^{-\frac{1}{2}} . \tag{2.9}$$

The Hamiltonian of the tip, the second term in Eq. (2.1), reads

$$\mathcal{H}_{\rm T} = \mathcal{H}_{\rm kin,T} + \mathcal{H}_{\mu_{\rm T}} . \tag{2.10}$$

Here

$$\mathcal{H}_{\rm kin,T} = -i\hbar v_{\rm T} \int_{-\infty}^{\infty} dy \ : c^\dagger(y)\partial_y c(y) : \tag{2.11}$$

describes the (linearized) band energy with respect to the equilibrium Fermi points $\pm k_{\rm T}$ of the tip, and $v_{\rm T}$ denotes the Fermi velocity. Notice that the integral runs also over the positive y-axis, since right- and left-moving electron operators along the physical tip axis $y < 0$ have been unfolded into one chiral (right-moving) operator $c(y)$ defined on the whole y-axis. The second term in Eq. (2.10) describes the bias $V_{\rm T}$ applied to the tip which affects the incoming electrons according to

$$\mathcal{H}_{\mu_{\rm T}} = eV_{\rm T} \int_{-\infty}^{0} dy \ : c^\dagger(y)c(y) : \quad . \tag{2.12}$$

Finally, the third term in Eq. (2.1) accounts for the wire-tip electron tunneling and reads

$$\mathcal{H}_{\rm tun} = \hbar\sqrt{v_{\rm W}v_{\rm T}} \sum_{r=\pm} \gamma_r \left(\mathrm{e}^{-irk_{\rm W}x_0}\Psi_r^\dagger(x_0)c(0) + \text{h.c.}\right) \tag{2.13}$$

where γ_r is the dimensionless tunneling amplitude for r-moving electrons, and $x = x_0$ [$y = 0$] is the coordinate of the injection point along the wire [tip]. Here, we have allowed for a right/left asymmetry of electron tunneling between the tip and the wire, which can arise from the presence of a magnetic field[41, 42, 51, 54]. Note that for $\gamma_+ \neq \gamma_-$ the Hamiltonian is not invariant under time-reversal symmetry.

In the following sections the electron current will be evaluated in the three terminals of the described set-up. Explicitly we shall compute

$$I(x,t) = ev_{\rm W} \left\langle : \Psi_+^\dagger(x,t)\Psi_+(x,t) : - : \Psi_-^\dagger(x,t)\Psi_-(x,t) : \right\rangle \tag{2.14}$$

where x, with $|x| > L/2$, is a measurement point located in the S or D leads. As far as the tip is concerned, due to the unfolding procedure described above, the electron current flowing in the tip at a point $y \leq 0$ acquires the form

$$I(y,t) = ev_{\rm T} \left\langle : c^\dagger(y,t)c(y,t) : - : c^\dagger(-y,t)c(-y,t) : \right\rangle . \tag{2.15}$$

In Eqs. (2.14) and (2.15) the averages are computed with respect to the stationary state in the presence of the applied dc voltages $V_{\rm S}$, $V_{\rm D}$, $V_{\rm T}$ and $V_{\rm G}$.

Under these conditions, the current in each electrode is actually independent of the measurement point. We thus denote by $I_{\rm S}$ and $I_{\rm D}$ the currents flowing in the source and drain electrodes. The current $I_{\rm S}$ is positive when flowing into the wire, while $I_{\rm D}$ is positive when flowing out of the wire. The current $I_{\rm T}$ flowing in the tip is positive when flowing in the direction of the tip-wire tunnel contact. Current conservation then implies $I_{\rm D} = I_{\rm S} + I_{\rm T}$, so that all currents can be expressed in terms of two independent quantities. One can write

$$I_{\rm S} = I_{\rm M} - I_{\rm T}/2 \tag{2.16}$$
$$I_{\rm D} = I_{\rm M} + I_{\rm T}/2 \tag{2.17}$$

where $I_{\rm M}$ describes the current flowing in the wire under the condition that no net current flows through the tip (voltage probe configuration). Importantly, $I_{\rm M}$ should *not* be identified with the two-terminal current flowing in the absence of the tip. Indeed, while $\gamma_\pm = 0$ implies that $I_{\rm T} = 0$, the opposite does not hold, so that $I_{\rm M}$ needs to be evaluated by accounting for the whole three-terminal set-up.

2.2 The non-interacting case

In this section we first discuss results for the case in which the electron interaction (2.8) is neglected. Then the Hamiltonian (2.1) of the whole system is quadratic in the fields $\Psi_\pm(x)$ and $c(y)$, and transport properties can be determined within the Landauer-Büttiker formalism. In the three-terminal set-up that we are considering, the scattering matrix $\mathsf{S}(E)$ is a 3×3 matrix which depends on the energy E measured with respect to the equilibrium wire-lead Fermi level. The currents $I_{\rm M}$ and $I_{\rm T}$ defined through Eq. (2.16)

and (2.17) read

$$\begin{aligned} I_{\rm M} &= \frac{e}{h}\Big[\frac{1}{2}\int_{-\infty}^{\infty}\big(|\mathsf{S}_{12}|^2+|\mathsf{S}_{21}|^2\big)\left(f_{\rm S}(E)-f_{\rm D}(E)\right)dE \\ &\quad +\frac{1}{2}\int_{-\infty}^{\infty}|\mathsf{S}_{13}|^2\left(f_{\rm S}(E)\,-\,f_{\rm T}(E)\right)dE \\ &\quad +\frac{1}{2}\int_{-\infty}^{\infty}|\mathsf{S}_{23}|^2\left(f_{\rm T}(E)\,-\,f_{\rm D}(E)\right)dE\Big] \end{aligned} \tag{2.18}$$

and

$$\begin{aligned} I_{\rm T} &= \frac{e}{h}\int_{-\infty}^{\infty}dE\left[|\mathsf{S}_{31}|^2\left(f_{\rm T}(E)-f_{\rm S}(E)\right)\right. \\ &\qquad \left.+|\mathsf{S}_{32}|^2\left(f_{\rm T}(E)-f_{\rm D}(E)\right)\right]. \end{aligned} \tag{2.19}$$

In the S-matrix elements appearing in Eqs. (2.18) and (2.19) the source, drain and tip electrodes are identified as 1, 2, and 3 respectively, whereas their Fermi functions are denoted as $f_{\rm S}$, $f_{\rm D}$ and $f_{\rm T}$. Note that the S-matrix is in general not symmetric, because time-reversal symmetry is broken for $\gamma_+ \neq \gamma_-$. The S-matrix can straightforwardly be evaluated with standard techniques by combining the transfer matrices M_{x_i} $(i=1,2)$ of the two side contacts

$$\mathsf{M}_{x_1,x_2} = \begin{pmatrix} {\rm e}^{-\frac{i}{2}u_{\rm G}}(1-i\lambda_{1,2}) & \pm i{\rm e}^{\pm\frac{i}{2}(2\varepsilon-u_{\rm G}+2\kappa_{\rm W})}\lambda_{1,2} & 0 \\ i{\rm e}^{\mp\frac{i}{2}(2\varepsilon-u_{\rm G}+2\kappa_{\rm W})}\lambda_{1,2} & {\rm e}^{\frac{i}{2}u_{\rm G}}(1+i\lambda_{1,2}) & 0 \\ 0 & 0 & 1 \end{pmatrix} \tag{2.20}$$

with the one, M_{x_0}, at the tip injection point

$$\begin{aligned} \mathsf{M}_{x_0} =& \frac{1}{1+(\gamma_+^2-\gamma_-^2)/4}\times \\ &\times\begin{pmatrix} 1-(\gamma_+^2+\gamma_-^2)/4 & -{\rm e}^{-2i(\varepsilon+\kappa_{\rm W}-u_{\rm G})\xi_0}\gamma_+\gamma_-/2 & -i{\rm e}^{-i(\varepsilon+\kappa_{\rm W}-u_{\rm G})\xi_0}\gamma_+ \\ {\rm e}^{2i(\varepsilon+\kappa_{\rm W}-u_{\rm G})\xi_0}\gamma_+\gamma_-/2 & 1+(\gamma_+^2+\gamma_-^2)/4 & i{\rm e}^{i(\varepsilon+\kappa_{\rm W}-u_{\rm G})\xi_0}\gamma_- \\ -i{\rm e}^{i(\varepsilon+\kappa_{\rm W}-u_{\rm G})\xi_0}\gamma_+ & -i{\rm e}^{-i(\varepsilon+\kappa_{\rm W}-u_{\rm G})\xi_0}\gamma_- & 1-(\gamma_+^2-\gamma_-^2)/4 \end{pmatrix}. \end{aligned} \tag{2.21}$$

We have introduced the ballistic frequency

$$\omega_L = \frac{v_{\rm F}}{L} \tag{2.22}$$

associated with the length of the wire, and the following dimensionless quantities

$$\xi_0 = \frac{x_0}{L}\,, \tag{2.23a}$$

$$\kappa_{\rm W} = k_{\rm W} L\,, \tag{2.23b}$$

$$u_{\rm G} = \frac{eV_{\rm G}}{\hbar\omega_L}\,, \tag{2.23c}$$

$$\varepsilon = \frac{E}{\hbar\omega_L}\,. \tag{2.23d}$$

The scattering matrix is obtained as a combination of the elements of the transmission matrix $\mathsf{M} = \mathsf{M}_{x_2}\mathsf{M}_{x_0}\mathsf{M}_{x_1}$ in the form

$$\begin{aligned} \mathsf{S} &= \mathsf{M}_{22}^{-1} \\ &\times \begin{pmatrix} -\mathsf{M}_{21} & 1 & -\mathsf{M}_{23} \\ \mathsf{M}_{11}\mathsf{M}_{22} - \mathsf{M}_{12}\mathsf{M}_{21} & \mathsf{M}_{12} & \mathsf{M}_{13}\mathsf{M}_{22} - \mathsf{M}_{12}\mathsf{M}_{23} \\ \mathsf{M}_{31}\mathsf{M}_{22} - \mathsf{M}_{21}\mathsf{M}_{32} & \mathsf{M}_{32} & \mathsf{M}_{33}\mathsf{M}_{22} - \mathsf{M}_{23}\mathsf{M}_{32} \end{pmatrix} \end{aligned} \tag{2.24}$$

where M_{ij} are the matrix elements of M.

2.2.1 Fabry-Pérot oscillations in a two-terminal set-up

Before discussing the influence of the STM tip, we shortly describe the transport properties in the absence of the tip, *i.e.* for $\gamma_\pm = 0$. In this case we have a two-terminal set-up with $I_{\rm T} = 0$ and $I_{\rm S} = I_{\rm D} = I_{\rm M}$. The solid line in Fig. 2.2 shows the two-terminal conductance $dI_{\rm M}/dV$ at zero temperature plotted in units of e^2/h as a function of the (dimensionless) source-drain bias

$$u = \frac{e(V_{\rm S} - V_{\rm D})}{\hbar\omega_L} \tag{2.25}$$

for identical contact impurity strengths $\lambda_1 = \lambda_2$. For $\lambda_i \ll 1$ the conductance shows the typical Fabry-Pérot oscillations with maximum values close to one. For carbon nanotubes the Fabry-Pérot regime of highly transparent contacts could be reached experimentally only recently due to progress achieved in device contacting [38, 44, 49, 50]. In the following, we will focus on this regime.

The electron current $I_{\rm S} = I_{\rm D} = I_{\rm M}$ can be written as

$$I_{\rm M} = I_0 + I_{\rm imp} \tag{2.26}$$

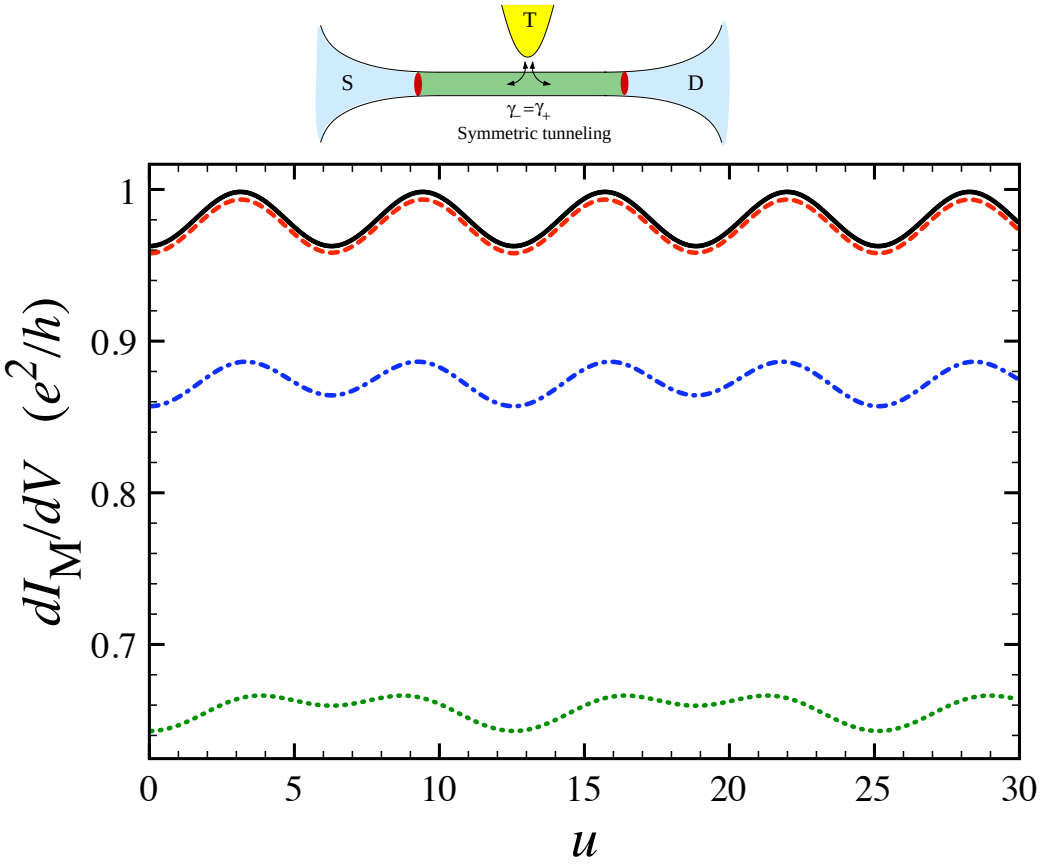

Figure 2.2: Zero temperature differential conductance as a function of the source-drain bias for a non-interacting wire characterized by contact impurity strengths $\lambda_1 = \lambda_2 = 0.1$ and a Fermi wavevector $\kappa_W = 0.3$. The tip is located in the middle of the wire and the tip voltage V_T is adjusted to fulfill the condition $I_T = 0$. Tunneling is symmetric ($\chi = 0$) and the tunneling strength has the values: $\gamma = 0$ (solid line), $\gamma = 0.1$ (dashed-line), $\gamma = 0.5$ (dashed-dotted line) and $\gamma = 1$ (dotted line). The gate is grounded ($V_G = 0$), and the bias is applied symmetrically ($V_{S/D} = \pm V/2$).

where $I_0 = (e^2/h)V$ represents the current of a perfectly contacted wire, and I_{imp} characterizes the (negative) correction due to the contact resistances. The exact expression for I_{imp}, which can be gained from the S-matrix, is not easily tractable for arbitrary impurity strengths and temperature. In the Fabry-Pérot regime at zero temperature, however, a simpler expression is obtained by expanding in terms of the impurity strengths. To third order

in the λ_i's one obtains

$$I_{\rm imp} = \frac{e\omega_L}{2\pi}\left(j_{\rm inc} + j_{\rm coh}\right) \tag{2.27}$$

where $j_{\rm inc}$ and $j_{\rm coh}$ are dimensionless quantities describing the incoherent and coherent contributions, respectively, to the reduction of the current by the contact impurities. The term

$$j_{\rm inc} = -\sum_{i=1,2}\lambda_i^2\, u\,, \tag{2.28}$$

is linear in the applied bias voltage, and the coefficient of proportionality is the "classical" series resistance of two impurities. In contrast, the term $j_{\rm coh}$ stems from quantum interference between scattering processes. This interference leads to the Fabry-Pérot oscillations of $j_{\rm coh}$. Explicitly,

$$j_{\rm coh} = j_{\rm coh}^{(2)} + j_{\rm coh}^{(3)} \tag{2.29}$$

where

$$j_{\rm coh}^{(2)} = -2\lambda_1\lambda_2\cos\left[2(u_{\rm W}+\kappa_{\rm W}-u_{\rm G})\right]\sin(u) \tag{2.30}$$

and

$$j_{\rm coh}^{(3)} = -2\left(\lambda_1\lambda_2^2+\lambda_1^2\lambda_2\right)\sin\left[2(u_{\rm W}+\kappa_{\rm W}-u_{\rm G})\right]\sin(u)\,, \tag{2.31}$$

where we have introduced

$$u_{\rm W} = \frac{e(V_{\rm S}+V_{\rm D})}{2\hbar\omega_L}\,. \tag{2.32}$$

From Eqs. (2.30)-(2.31) one can see that Fabry-Pérot oscillations arise both as a function of the source-drain bias u and as a function of the gate voltage $u_{\rm G}$. Note that for a non-interacting system the period in the former case is twice as large as the period in the latter case.

We also emphasize that $j_{\rm coh}^{(3)}$ originates from impurity forward-scattering processes (more precisely from second order in backward scattering and first order in forward scattering). Forward scattering processes are typically neglected in single impurity problems, where they can be gauged away. However, when two or more impurities are present they affect the coherent part of transport. Although this contribution is in general smaller than $j_{\rm coh}^{(2)}$, it becomes the dominant term for the Fabry-Pérot oscillations when $j_{\rm coh}^{(2)}$ vanishes, which is the case for

$$\frac{4}{\pi}\left(k_{\rm W}L + \frac{e(V_{\rm S}+V_{\rm D}-2V_{\rm G})}{2\hbar\omega_L}\right) \simeq \text{ odd integer}\,. \tag{2.33}$$

Thus, the third order term is crucial for certain values of the biasing voltage.

We conclude the discussion of the two-terminal case by emphasizing that for a non-interacting wire in the Fabry-Pérot regime the current depends not only on the difference $V_{\rm S} - V_{\rm D}$, but in general on $V_{\rm S}$ and $V_{\rm D}$ separately. This is simply due to the fact that Fabry-Pérot interference effects lead to an energy-dependent transmission coefficient and, hence, to non-linearity in the applied bias. Notice that Eqs. (2.28), (2.30) and (2.31) fulfill the gauge-invariance condition emphasized by Büttiker [55], since they are invariant under an overall shift of the potentials $V_p \to V_p + \text{const}$ ($p = \text{S}, \text{D}, \text{G}$).

2.2.2 Effects of the tip on Fabry-Pérot oscillations

In this section we shall address, within the non-interacting electron approximation, the effect of the STM tip on the Fabry-Pérot oscillations. When $\gamma_\pm \neq 0$, the currents $I_{\rm M}$ and $I_{\rm T}$ are non-vanishing for arbitrary values of the applied voltages $V_{\rm S}$, $V_{\rm D}$ and $V_{\rm T}$. We analyze the effects of the tip as a function of the total tunneling strength γ, defined through

$$\gamma^2 = \frac{\gamma_+^2 + \gamma_-^2}{2} \quad , \tag{2.34}$$

the tunneling asymmetry coefficient

$$\chi = \frac{\gamma_+^2 - \gamma_-^2}{\gamma_+^2 + \gamma_-^2} \qquad |\chi| \leq 1 \ , \tag{2.35}$$

and the position x_0 of the tip.

We start by considering the situation where the tip behaves as an electron injector: a bias is applied between the tip and the source and drain electrodes, which, for simplicity, are assumed to be at the same electrochemical potential. A quite standard calculation applies to the case of fully symmetric tunneling ($\chi = 0$), allowing, *e.g.*, to relate the local density of states in the wire to the non-linear conductance as a function of the tip-wire bias. Here, we shall instead focus on the case of fully asymmetric tunneling ($\chi = \pm 1$), which has become of particular interest due to recent experiments where only right-moving and/or only left-moving electrons could be selectively tunneled into a semiconductor quantum wire due to the presence of a magnetic field normal to the plane of the wire and the tip.[51] We find that novel physical aspects emerge from a tunneling asymmetry. In the first instance, a direct inspection of the scattering matrix (2.24) shows that its elements S_{ij} are independent of x_0, implying that, differently from the case of symmetric tunneling $\chi = 0$, the

lead currents $I_{\rm D}$ and $I_{\rm S}$ *do not* depend on the position of the tip. Furthermore, asymmetric tunneling can be used to extract the transmission coefficient of each contact. Indeed evaluating the asymmetry

$$\mathcal{A}(\chi) \doteq \left.\frac{|I_{\rm D}| - |I_{\rm S}|}{|I_{\rm D}| + |I_{\rm S}|}\right|_{\chi} \tag{2.36}$$

between $I_{\rm D}$ and $I_{\rm S}$ in the two cases of totally asymmetric injection only to the right ($\chi = 1$) and only to the left ($\chi = -1$), one obtains

$$\mathcal{A}_+ = \frac{1 + \lambda_1^2 - \lambda_2^2}{1 + \lambda_1^2 + \lambda_2^2} \tag{2.37}$$

and

$$\mathcal{A}_- = \frac{1 + \lambda_2^2 - \lambda_1^2}{1 + \lambda_1^2 + \lambda_2^2}\,. \tag{2.38}$$

where $\mathcal{A}_\pm = \pm\mathcal{A}(\pm 1)$. From these coefficients it is straightforward to extract the strengths of the contact impurities

$$\begin{aligned} \lambda_1^2 &= \frac{1 - \mathcal{A}_-}{\mathcal{A}_+ + \mathcal{A}_-} \\ \lambda_2^2 &= \frac{1 - \mathcal{A}_+}{\mathcal{A}_+ + \mathcal{A}_-}\,. \end{aligned} \tag{2.39}$$

as well as the transmission coefficients

$$\mathcal{T}_{1,2} \doteq \frac{1}{1 + \lambda_{1,2}^2} = \frac{\mathcal{A}_+ + \mathcal{A}_-}{1 + \mathcal{A}_\pm} \tag{2.40}$$

related to each of the two contacts.
Notice that, while $I_{\rm S}$ and $I_{\rm D}$ depend on the temperature T, Eqs. (2.37) and (2.38) are independent of T within the approximation of a linearized band. Interestingly, these equations also enable one to identify the relation between the current asymmetry coefficients $\mathcal{A}_\pm$ and the two-terminal conductance $G_{\rm 2t} = \partial I_{\rm M}/\partial V|_{\gamma=0}$. In Ref. [54], the equality $\mathcal{A}_\pm = G_{\rm 2t}/(e^2/h)$ is claimed to hold for a set-up with symmetric contacts to the leads, even in the presence of interactions. However, Eqs. (2.37) and (2.38) show that for a quantum wire in the Fabry-Pérot regime, even in the absence of interactions and with perfectly symmetric contacts $\lambda_1 = \lambda_2$, one has

$$\mathcal{A}_+ = \mathcal{A}_- \neq G_{\rm 2t}/(e^2/h) \tag{2.41}$$

since $\mathcal{A}_\pm = 1/(1+2\lambda_1^2)$ is a constant, whereas $G_{2\mathrm{t}}$ depends on temperature, source-drain bias and gate voltage. The equality sign in Eq. (2.41) holds only under the specific circumstances of perfectly transmitting contacts ($\lambda_{1,2} = 0$), or of a perfectly symmetric set-up ($\lambda_1 = \lambda_2 \neq 0$) at sufficiently high temperatures $k_\mathrm{B}T \gg \hbar\omega_L$, where Fabry-Pérot oscillations of $G_{2\mathrm{t}}$ wash out.

The second situation that we want to investigate is when the tip voltage V_T is set to an appropriate value $\bar{V}_\mathrm{T}$ so that no net current flows through the tip. This corresponds to a situation where the tip behaves as a voltage probe.[2] Notice that, even under the condition $I_\mathrm{T} = 0$, electrons can tunnel from the tip to the wire and vice versa, and therefore the tip *does* affect the electron transport between source and drain.

We start by describing the case of symmetric tunneling ($\chi = 0$) with the tip located in the middle of the wire ($x_0 = 0$). The differential conductance dI_M/dV, evaluated under the condition $I_\mathrm{T} = 0$, is depicted in Fig. 2.2 as a function of the source-drain bias (2.25), for different values of γ, ranging from weak to strong tunneling. The tip has three main effects on the Fabry-Pérot oscillations: i) an overall suppression of the conductance, ii) a modulation of the maxima and minima, and iii) a reduction of the visibility of the oscillations.

The origin of the first effect can be illustrated already in the case of a clean wire ($\lambda_i = 0$), where it is easy to show that the condition $I_\mathrm{T} = 0$ is fulfilled for a tip voltage $\bar{V}_\mathrm{T} = (V_\mathrm{S} + V_\mathrm{D})/2$, and that

$$I_\mathrm{M} = \frac{e^2}{h}\frac{V_\mathrm{S} - V_\mathrm{D}}{1+\gamma^2/2} \;<\; \frac{e^2}{h}(V_\mathrm{S} - V_\mathrm{D}), \tag{2.42}$$

Notice that a reduction of the conductance already shows up to order γ^2 in the tunneling strength. The reason for this suppression of the current is that a fraction of the electron flow originating from the source is diverted into the tip due to the tip-wire coupling. While the condition $I_\mathrm{T} = 0$ ensures that the same electron current is re-injected into the wire, for symmetric tunneling the tip injects with equal probabilities right- and left-moving electrons. Hence half of the injected current flows back to the source electrode, causing

[2]Here V_T is taken as an external parameter, and the choice of the value $\bar{V}_\mathrm{T}$ ensures a vanishing average current I_T. The term 'voltage probe' is sometimes also used in the literature for a terminal where the electrochemical potential dynamically changes to ensure that both the average current I_T and its current fluctuations vanish (see *e.g.* Refs. [32, 33, 34]). As far as the results for the average currents in the set-up are concerned, our definition of a voltage probe is equivalent to the latter choice. Differences may emerge for the current fluctuations, which are beyond the topic of the present work.

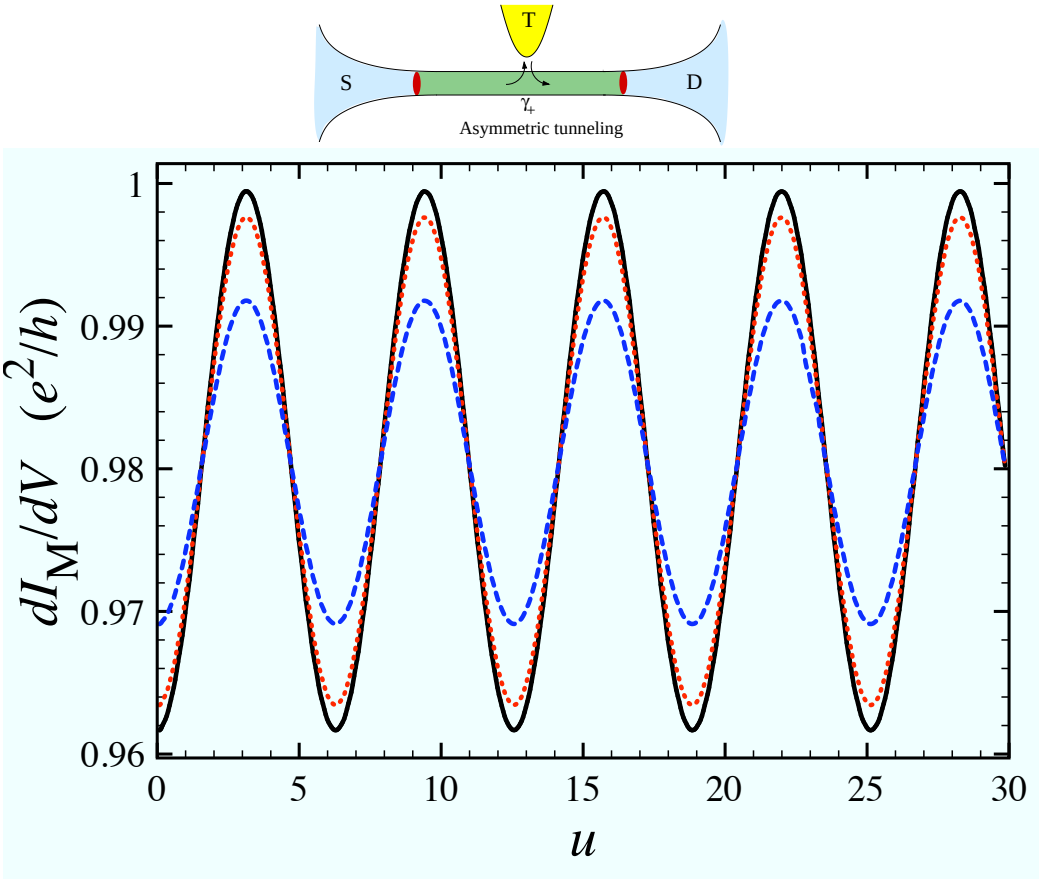

Figure 2.3: Zero temperature differential conductance as a function of the source-drain bias for a non-interacting wire with contact impurity strengths $\lambda_1 = \lambda_2 = 0.1$ in presence of a tip with an applied voltage V_T adjusted to fulfill the condition $I_T = 0$. Tunneling is totally asymmetric ($\chi = 1$) and the tunneling strength has the values $\gamma = 0.3$ (dotted line) and $\gamma = 0.7$ (dashed line).

the reduction of the two-terminal conductance. As we shall see below, the situation is different in the case of asymmetric tunneling.

The second feature that can be observed in Fig. 2.2 is an alternating depth of the Fabry-Pérot minima. This modulation originates from the interference between different paths that are possible for an electron ejected from the tip. For instance, the path of an electron ejected as a right-mover towards the drain can interfere with the path starting as a left-mover towards the source followed by an elastic backscattering at the source contact. The difference in length between these paths corresponds to a new frequency in the oscillations, which causes the modulation of the peaks. In the case of Fig. 2.2, where the

tip is located in the middle, this additional frequency equals twice the Fabry-Pérot frequency, so that the tip affects every second minimum in the same way. As we shall see below, in general, the modulation pattern depends both on the asymmetry coefficient and on the position of the tip. The modulation effect arises to order $\gamma^2\lambda$ when we treat the impurity strength and tunneling amplitudes as perturbation parameters.

The third effect of the tip consists in a reduction of the visibility of the the Fabry-Pérot oscillations: in the presence of the tip the relative separation between maxima and minima decreases. This reduction stems from the decoherence introduced by the tip, since the probability of constructive interference between paths with two backscattering processes at the contacts decreases when electrons can be incoherently absorbed and re-ejected by the tip. Notice that the reduction of visibility is of order $\gamma^2\lambda^2$, and it is therefore negligible with respect to the modulation effect in the Fabry-Pérot regime.

Let us now discuss the role of asymmetric tunneling in the voltage probe configuration. When $\chi \neq 0$, the effect of conductance suppression is less pronounced then for symmetric tunneling. This can be seen already in the case of a clean wire ($\lambda_i = 0$), where

$$I_{\rm M} = \frac{e^2}{h}(V_{\rm S} - V_{\rm D})\frac{2+\gamma^2\chi^2}{2+\gamma^2}\,, \tag{2.43}$$

and the value $\bar{V}_{\rm T}$ of the tip voltage ensuring $I_{\rm T} = 0$ is given by

$$\bar{V}_{\rm T} = \frac{1}{2}\left[V_{\rm S}(1+\chi) + V_{\rm D}(1-\chi)\right]\,. \tag{2.44}$$

As one can see from the last factor in Eq. (2.43), the suppression of the current $I_{\rm M}$ is completely absent for fully asymmetric tunneling $\chi = \pm 1$. Importantly, this features persists also in the presence of realistic contacts ($\lambda_i \neq 0$), as shown in Figure 2.3, where the differential conductance $dI_{\rm M}/dV$ is plotted as a function of the source-drain voltage for several values of the tunneling strength γ. Increasing the tunneling strength simply decreases the amplitude of the Fabry-Pérot oscillations but does not change the average value of the conductance. Two more noteworthy features can be observed: in the fully asymmetric case also the modulation of the peaks is absent, and the non-linear conductance is independent of the tip position. The reason lies in the specific tunneling conditions. For example, a right-moving electron ejected by the tip cannot be re-absorbed after scattering as a left-moving one, and this rules out interference effects between electrons traveling through the tip and electrons that have undergone an odd number of backscattering events at the contacts. Such processes would give rise to effects related to the tip

position, while interference phenomena with electrons that have undergone an even number of backscattering events, which continue to be present also for $\chi = \pm 1$, are independent of the tip position. Moreover, in the completely asymmetric case, electrons passing through the tip continue to move in the same direction, and this is the reason why, also for strong tunneling, the average value of the differential conductance is independent of γ.

Finally, we analyze the dependence of the differential conductance on the tip position. For simplicity we limit this discussion to the case of symmetric tunneling illustrated in Fig. 2.4. Apart from the conductance suppression discussed above, one sees that the modulation effect exhibits a strong dependence on the tip position. In particular, when the tip is close to a contact impurity, we observe Fabry-Pérot-like oscillations over-imposed by an oscillation with large period due to coherent motion of carriers between the tip and the contact impurity remote from the tip.

2.3 The interacting case

Let us now turn to the study of the effects that electron-electron interactions have on the transport properties of our setup. Electronic interactions will be taken into account exactly through the bosonization formalism. However, an analytical treatment of the contact impurities and of the tunnelling amplitudes is not possible. We will therfore restrict our analysis to the regime of weak contact impurities (in which Fabry-Pérot oscillations arise) and of weak tip-wire coupling, treating the perameters $\gamma_\pm$ and λ_i as small perturbations. The evaluation of the currents in the three terminals will be based on the out-of-equilibrium Keldysh formalism.[56] The regime of highly transparent contacts to the electrodes for interacting wires has already been analyzed for a two-terminal set-up [52, 53].

We start by neglecting the presence of the tip in order to sudy the effects of interactions on just the Fabry-Pérot oscillations.

2.3.1 Interaction effects on Fabry-Pérot oscillations in a two-terminal set-up

Let us first analyze the effects of electron-electron interaction for a contacted wire without tip. As in the non-interacting case, for $\gamma_\pm = 0$ the problem is reduced to a two-terminal set-up, where $I_\mathrm{T} = 0$ and $I_\mathrm{S} = I_\mathrm{D} = I_\mathrm{M}$. Furthermore, I_M can again be written as a sum of the current I_0 in a wire with adiabatic contacts and I_imp, see Eq. (2.26). Importantly, while I_0 is

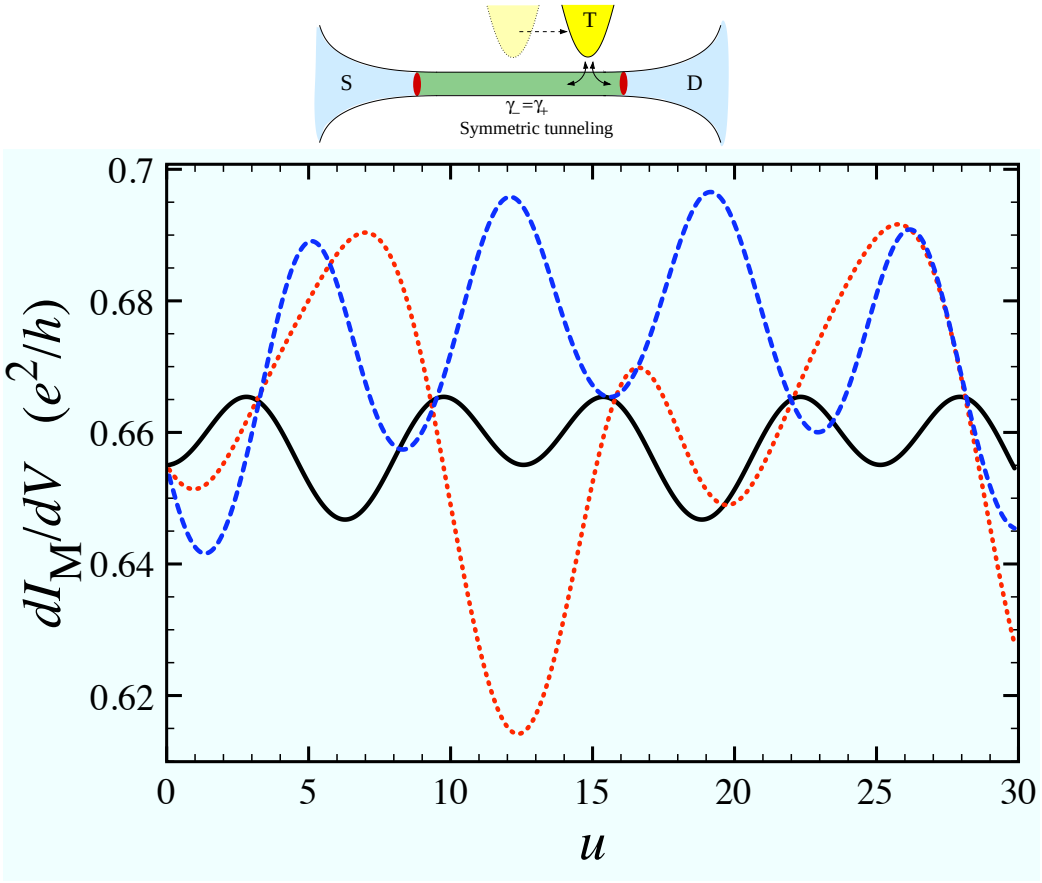

Figure 2.4: Zero temperature differential conductance as a function of the source-drain voltage for a non-interacting wire for several values of the tip position $x_0 = 0$ (solid line), $x_0 = 0.17$ (dotted line) and $x_0 = 0.41$ (dashed line). Tunneling has amplitude $\gamma = 1$ and is symmetric ($\chi = 0$). The contact impurities have equal strengths $\lambda_1 = \lambda_2 = 0.1$. The gate is grounded ($V_{\rm G} = 0$), and the bias is applied symmetrically ($V_{\rm S/D} = \pm V/2$).

unaffected by the interaction in the wire [7, 8, 9], the current $I_{\rm imp}$, accounting for the contact resistances, is strongly modified by the interaction. One can still decompose $I_{\rm imp}$ into

$$I_{\rm imp} = \frac{e\omega_L^*}{2\pi}\left(j_{\rm inc} + j_{\rm coh}\right), \tag{2.45}$$

where $j_{\rm inc}$ is the sum of two terms related to a single impurity each, and $j_{\rm coh}$ describes interference between scattering processes at the two impurities. Here, an important difference emerges with respect to the non-interacting case. The Fermi velocity *in the wire* is enhanced by the interaction parameter

g, leading to a higher ballistic frequency

$$\omega_L^* = \frac{\omega_L}{g}\,. \tag{2.46}$$

Moreover, the interaction also affects the strength of the contact impurities: the forward-scattering processes are left unchanged whereas the backscattering ones are renormalized[3]

$$\lambda \to \begin{cases} \lambda_{\mathrm{B},i}^* = \lambda\, \alpha_{\mathrm{W}}^{g-1} \\ \lambda_{\mathrm{F},i} = \lambda \end{cases} \quad . \tag{2.47}$$

where $\alpha_{\mathrm{W}} = a_{\mathrm{W}}/gL$ is a small dimensionless cutoff parameter. The cutoff length a_{W}, which is related to the lattice spacing or the electronic bandwidth of order $\hbar v_{\mathrm{W}}/a_{\mathrm{W}}$, is introduced in App. B.

In the Fabry-Pérot regime we can again restrict ourselves to terms up to third order in the contact impurity strengths λ_i. Then, the incoherent and the coherent contributions can be written as

$$j_{\mathrm{inc}} = \sum_{i=1,2} j_{\mathrm{inc},i} \tag{2.48}$$

and

$$j_{\mathrm{coh}} = j_{\mathrm{coh}}^{(2)} + j_{\mathrm{coh}}^{(3)}\,, \tag{2.49}$$

with

$$j_{\mathrm{inc,i}} = (\lambda_{\mathrm{B},i}^*)^2 D_{ii}(u) \tag{2.50}$$

and

$$j_{\mathrm{coh}}^{(2)} = 2\lambda_{\mathrm{B},1}^*\lambda_{\mathrm{B},2}^* D_{12}(u)\cos\left\{2\left[\kappa_{\mathrm{W}} + g(u_{\mathrm{W}} - u_{\mathrm{G}})\right]\right\} \tag{2.51}$$

$$\begin{aligned} j_{\mathrm{coh}}^{(3)} =& 2\lambda_{\mathrm{B},1}^*\lambda_{\mathrm{B},2}^*(\lambda_{\mathrm{F},1} + \lambda_{\mathrm{F},2}) D_{12}(u) \\ & \times g^2 \sin\left\{2\left[\kappa_{\mathrm{W}} + g(u_{\mathrm{W}} - u_{\mathrm{G}})\right]\right\}, \end{aligned} \tag{2.52}$$

where we have introduced

$$\begin{aligned} D_{ij}(u) = \frac{2}{\pi\alpha_{\mathrm{W}}^{2g}} \int_0^\infty d\tau \sin(u\tau) \\ \times \sin\left[4\pi\mathcal{I}^{\Phi\Phi}(\xi_i;\xi_j;\tau)\right]\, \mathrm{e}^{4\pi\mathcal{R}_{\mathrm{reg}}^{\Phi\Phi}(\xi_i;\xi_j;\tau)}\,. \end{aligned} \tag{2.53}$$

[3]Note that the renormalization exhibits the same scaling exponent as in the homogeneous Luttinger liquid model (see *e.g.* C. L. Kane, and M. P. A. Fisher, Phys. Rev. B **46**, 15233(1992)). In the inhomogeneous Luttinger liquid model used here, however, the renormalization flow driven by the relevant impurity backscattering operator is cut not only by a finite temperature T or bias V, but also by the finite length of the wire L. For this reason our perturbative treatment is safe also at $V = 0$ and $T = 0$.

The dimensionless voltages $u, u_{\rm W}$ and $u_{\rm G}$ are now scaled by the factor $e/\hbar\omega_L^*$ compared to the physical voltages $V_{\rm S} - V_{\rm D}, (V_{\rm S} + V_{\rm D})/2$ and $V_{\rm G}$, respectively. In the expression for D_{ij}, the dimensionless integration time is defined as $\tau = \omega_L^* t$, and the functions $\mathcal{R}^{\Phi\Phi}_{\rm reg}(\xi;\xi';\tau)$ and $\mathcal{I}^{\Phi\Phi}(\xi;\xi';\tau)$ are the real and imaginary parts, respectively, of the auto-correlation function of the bosonic phase field Φ introduced in App. B. The quantity D_{ij} defined in Eq. (2.53) is cut-off independent, since the cut-off dependence of the prefactor is compensated by one of the correlation functions. Explicit results for the phase field auto-correlation function have been given in a previous paper [10, 57]. Further, the $\xi_i = x_i/L$ $(i = 1, 2)$ are dimensionless contact impurity positions. Equations (2.50-2.52) are obtained from a perturbative development of the current in the impurity strengths λ_i employing the methods described in Apps. A and B. The current $j^{(3)}_{\rm coh}$ in Eq. (2.52) includes forward scattering processes that give rise to the factor $\lambda_{{\rm F},1} + \lambda_{{\rm F},2}$ and a twofold backscattering contribution leading to the factor $\lambda^*_{{\rm B},1}\lambda^*_{{\rm B},2}$.

Another important effect of the interaction is that the incoherent term $j_{\rm inc}$ does not depend linearly on the bias as in the non-interacting case. Instead, it exhibits oscillations of period $\Delta u = \pi$, due to the interplay between backward scattering at one contact impurity and Andreev-type reflection at the other contact. [10, 57] On the other hand, the coherent term $j_{\rm coh}$, responsible for Fabry-Pérot oscillations, shows a power-law suppression with increasing voltage.[52, 53] Thus, in the presence of interaction two types of oscillations are present, namely the Fabry-Pérot ones (already existing for a non-interacting wire and modified by the interaction), and the Andreev-type ones (purely due to the interaction). These two types of oscillations are characterized by the same period in the source-drain bias, and they are of the same order in the impurity strength, if we assume that the two contact transparencies are comparable ($\lambda_1 \simeq \lambda_2$). It is therefore difficult to distinguish the two phenomena from an inspection of the two-terminal differential conductance, which is shown in Fig. 2.5 as a function of the source-drain bias for various values of the interaction parameter g. Besides the power-law suppression of the amplitude at high applied bias, we see that for strong interaction ($g < 1/2$) the sinusoidal behavior of the oscillations is deformed into a saw-tooth-like shape. Furthermore, although the total current (2.26) in the presence of contact resistances is always smaller than the current I_0 of an ideally contacted wire ($I_{\rm imp} \leq 0$), the differential conductance may exceed e^2/h. This is a well-known effect of non-linear transport in Luttinger liquids[58], reflecting the fact that the conductance cannot be expressed in terms of single-particle transmission coefficients. In Sec. 2.4 we shall comment on how the two types of oscillations may be experimentally distinguished in a three-terminal set-up.

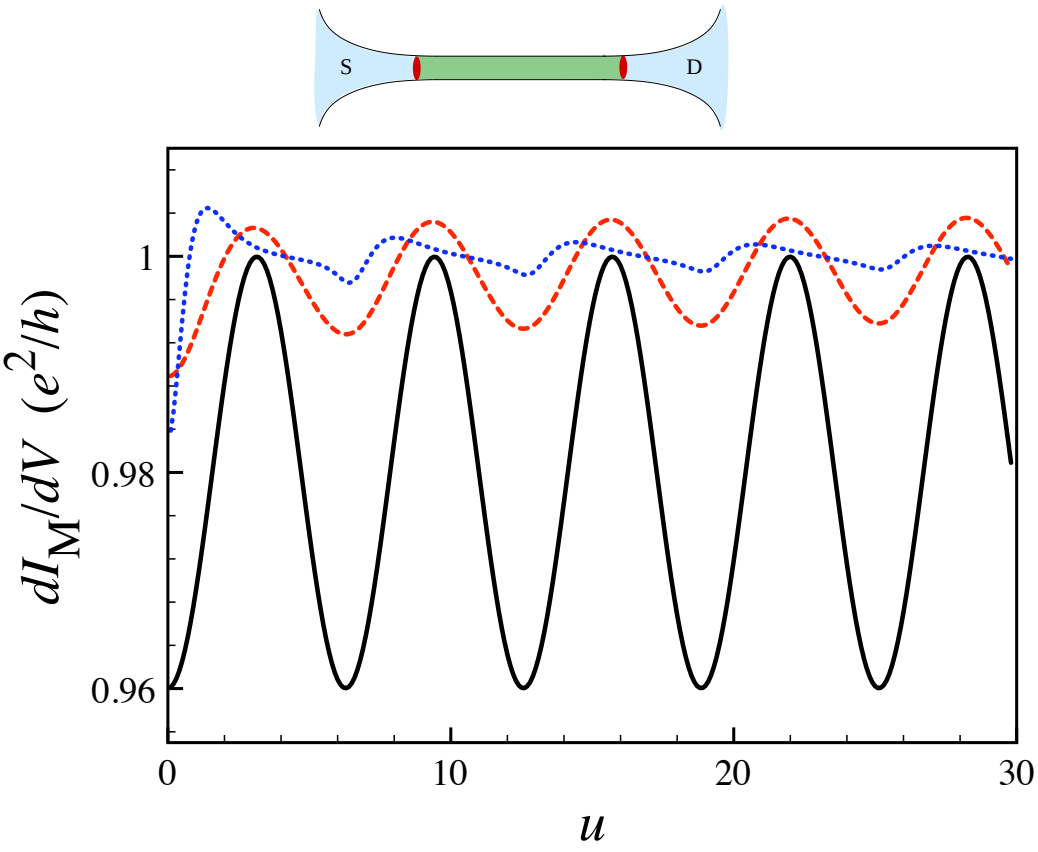

Figure 2.5: Differential conductance of an interacting quantum wire with impurities at the contacts as a function of the source-drain voltage for several values of the interaction parameter: $g = 1$ (solid line), $g = 0.75$ (dashed line) and $g = 0.25$ (dotted line). The contact impurities have equal strengths $\lambda^*_{\mathrm{B},1} = \lambda^*_{\mathrm{B},2} = 0.1$. The gate voltage is $V_{\mathrm{G}} = 0$, and the bias is applied symmetrically ($V_{\mathrm{S/D}} = \pm V/2$).

Further interesting insights emerge from the analysis of the conductance dI_{M}/dV as a function of both the source-drain bias $V = V_{\mathrm{S}} - V_{\mathrm{D}} = (\hbar\omega^*_L/e)u$ and the gate bias $V_{\mathrm{G}} = (\hbar\omega^*_L/e)u_{\mathrm{G}}$. Corresponding conductance plots are shown in Fig. 2.6. Panels (a), (b) and (c) refer to three different values of the interaction strength g, in the case of a symmetrically applied source-drain bias, $u_{\mathrm{S/D}} = \pm u/2$. The oscillations of the conductance as a function of V and V_{G} are characterized by two periods ΔV and ΔV_{G}. The period ΔV coincides with the period of the function $D_{12}(u)$ [Eq. (2.53)] appearing in the coherent terms (2.51) and (2.52), since the functions $D_{11}(u)$ and $D_{22}(u)$ related to the incoherent contribution (2.50) exhibit the period $\Delta V/2$. We

thus recover the result of Ref. [53]. On the other hand, the period $\Delta V_{\rm G}$ in the gate voltage is determined by the sinusoidal factors of Eqs. (2.51) and (2.52). The values of ΔV and $\Delta V_{\rm G}$ depend on the interaction strength g and are inversely proportional to g and g^2, respectively. Interestingly, the ratio of these periods yields the Luttinger liquid interaction strength, $\Delta V/\Delta V_{\rm G} = \Delta u\,/\Delta u_{\rm G} = 2g$, as can be checked from the table associated with Fig. 2.6.

Panel (d) describes the case of an asymmetrically applied bias ($u_{\rm S} = u$ and $u_{\rm D} = 0$), for the same interaction strength as panel (b). In this case $u_{\rm W} = u/2$ [see Eq.(2.32)], so that an additional dependence on V arises from the sinusoidal factors of Eqs. (2.51) and (2.52), and the period in V at fixed $V_{\rm G}$ changes. For this reason the two-dimensional pattern of the nonlinear conductance is twisted with respect to panel (b). However, the quantities ΔV and $\Delta V_{\rm G}$ related to a symmetrically applied bias can still be obtained, *e.g.*, by projecting the conductance maxima on the V-axis and measuring the distance between these projections as indicated by the arrows in panel (d). The value of g can therefore be extracted also in this case as $\Delta u\,/\Delta u_{\rm G} = 2g$. We remark that a qualitatively similar twist of the conductance pattern has recently been observed in carbon nanotubes [49].

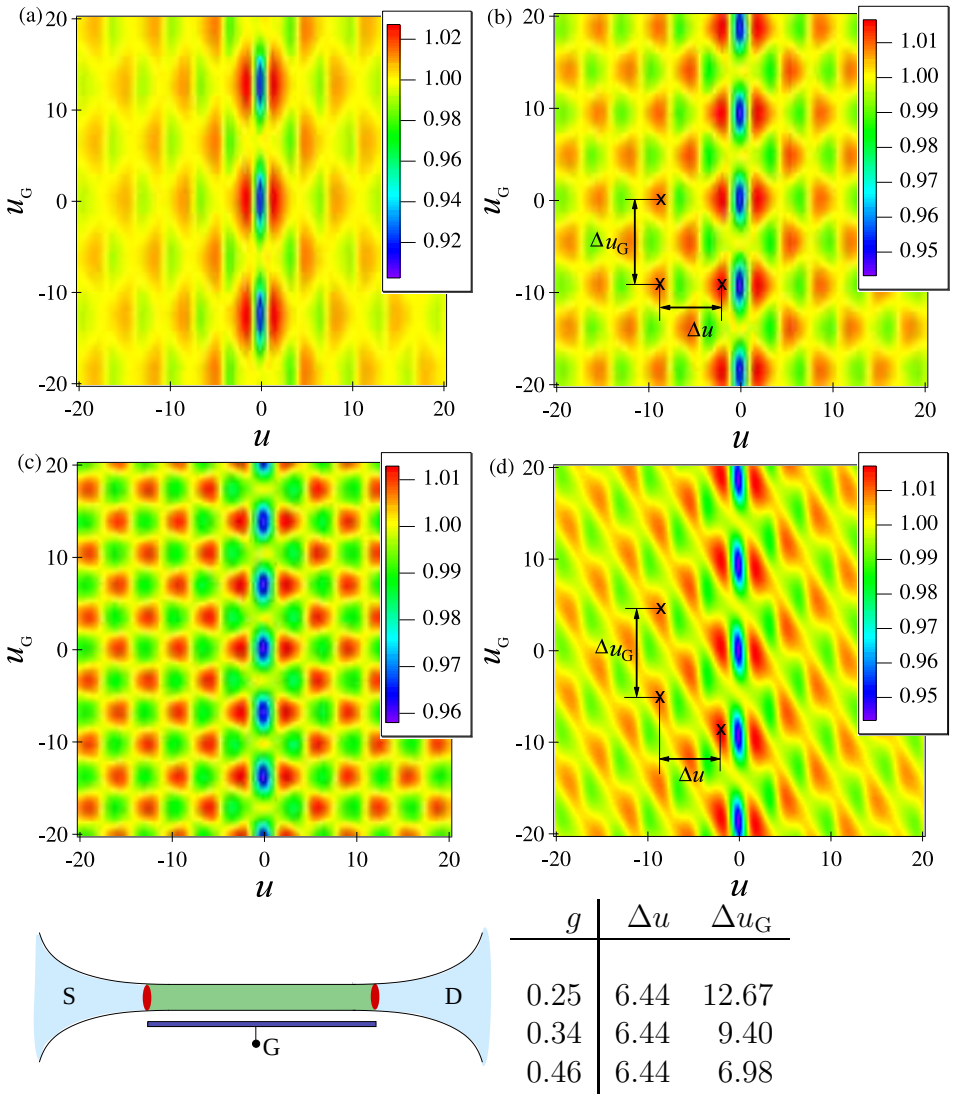

g	Δu	Δu_G
0.25	6.44	12.67
0.34	6.44	9.40
0.46	6.44	6.98

Figure 2.6: The differential conductance dI_M/dV (in units of $e\omega_L^*/2\pi$) of the two-terminal setup in the absence of a tip is shown as a function of the dimensionless source-drain bias u and the dimensionless gate voltage u_G. The strengths of the contact impurities are equal, and are characterized by $\lambda_{F,i} = 0.1$ and $\lambda^*_{B,i} = 0.25$. In panels (a), (b), and (c) the source-drain voltage is applied symmetrically, $u_{S/D} = \pm u/2$, and the interaction parameter is $g = 0.25, 0.34$, and 0.46, respectively. The dashed-dotted lines in panels (b) and (d) are a guide for the eye to identify the periodic pattern of the Fabry-Pérot oscillations determined by the periods Δu and Δu_G. Their ratio yields the value of g, as shown in the table for the three cases. In panel (d) the source-drain voltage is applied asymmetrically ($u_S = u$ and $u_D = 0$) to a wire with interaction strength $g = 0.34$. When compared with panel (b) for the same interaction strength, the asymmetric bias twists the pattern.

Conductance plots as a function of the transport and gate voltages have previously been discussed in the context of carbon nanotubes in Refs. [52] and [53]. We point out that the way we introduce the bias and gate voltages in our model [see Eq. (2.6)] differs from the one adopted in the above papers. Our approach accounts for several basic physical facts. In a non-chiral quantum wire only the electrochemical potentials of the leads can be controlled experimentally, whereas the electrochemical potentials of right- and left-movers inside the wire are a result of the biasing of the wire and its screening properties. As a consequence, the source and drain biases, $V_{\rm S}$ and $V_{\rm D}$, are applied here only in the related leads. This is in accord with a basic hypothesis underlying the definition of an electrode, namely that inelastic processes in the lead equilibrate absorbed electrons, yielding a voltage drop at the contacts *even* in the absence of contact impurities. On the other hand, the charge density of metallic electrodes is typically insensitive to a gate, due to their electroneutrality. For this reason, in our model the gate voltage $V_{\rm G}$ is applied only to the interacting wire and not to the leads.

The precise form of the coupling to the biasing voltages adopted in the model has implications on the behavior of the current as a function of bias and gate voltages. We find that the dependence on $V_{\rm G}$ and $(V_{\rm S}+V_{\rm D})/2$ involves a factor g^2, as shown, for instance, in Eqs. (2.51) and (2.52). [In the dimensionless formulation one factor of g is contained in the definition of the dimensionless quantities $u_{\rm G}$ and $u_{\rm W}$.] The difference $(V_{\rm S}+V_{\rm D})/2-V_{\rm G}$ is proportional to the *bare* electron charge injected into the wire, whereas the g^2 factor originates from the partial screening occurring in a Luttinger liquid [59], and physically describes the fraction of the bare charge that remains unscreened. In particular, in the limit $g\to 0$ of an electroneutral wire we obtain that the current depends only on the difference $V_{\rm S}-V_{\rm D}$ and is independent of the gate, as it should be.

On a more formal level, these physical properties are encoded in the zero modes $\Phi_{0,\pm}(x)$ [see Eq. (B.13)]. Indeed, the transformation $\Phi_\pm\to\Phi_\pm+\Phi_{0,\pm}$ of the chiral boson fields gauges away the bias term (2.6). We note that, differently from the homogenous Luttinger liquid case, in the presence of leads the zero modes cannot be just linear functions of the position uniformly along the entire system. The inhomogeneity of the system leads to a non-trivial space dependence of the zero modes $\Phi_{0,\pm}(x)$, which can be obtained from the boson Green function of the inhomogeneous LL model, as shown in Eq. (B.14).

2.3.2 Interaction effects on electron tunneling from the tip: The case of adiabatic contacts

We shall now consider the full three-terminal set-up, and discuss the effects of the wire electron-electron interaction on tunneling from the tip, both for the case of electron injection and in the voltage probe configuration. We start by presenting results for a wire with adiabatic contacts ($\lambda_i = 0$). For a non-interacting wire, the calculation described in Sec. 2.2 yields

$$I_{\rm T} = \frac{e^2}{h}\frac{8\gamma^2}{(2+\gamma^2)^2}\left(V_{\rm T} - \frac{1+\chi}{2}V_{\rm S} - \frac{1-\chi}{2}V_{\rm D}\right) \tag{2.54}$$

and

$$\begin{aligned} I_{\rm M} &= \frac{e^2}{h}\frac{1}{(2+\gamma^2)^2}\left\{V_{\rm S}\left[4+2\gamma^2(1-\chi+\gamma^2\chi^2)\right]\right. \\ &\quad \left. -V_{\rm D}[4+2\gamma^2(1+\chi+\gamma^2\chi^2)] + 4\chi\gamma^2 V_{\rm T}\right\}, \end{aligned} \tag{2.55}$$

where γ is the total tunneling strength defined in Eq. (2.34) and χ is the tunneling asymmetry parameter introduced in Eq. (2.35). Thus, in the absence of interaction, the currents depend linearly on the three applied voltages and are independent of the position x_0 of the tip.

When electron-electron interaction is taken into account, an exact solution of the tunneling problem is not possible for arbitrary values of the tunneling amplitudes $\gamma_\pm$. We shall assume that $\gamma_\pm \ll 1$, consistent with the tunnel Hamiltonian approach, and provide results up to leading order in perturbation theory. The currents in the source and drain leads are again written as in Eqs. (2.16) and (2.17), where $I_{\rm M}$ and $I_{\rm T}$ are evaluated now to order γ^2 yielding

$$I_{\rm M} = I_0 + I_{{\rm M},\gamma^2} \tag{2.56}$$

and

$$I_{\rm T} = I_{{\rm T},\gamma^2} \tag{2.57}$$

where

$$I_{{\rm M(T)},\gamma^2} = \frac{e\omega_L^*}{2\pi}(\gamma^*)^2\, j_{{\rm M(T)},\gamma^2}\,. \tag{2.58}$$

Here

$$\gamma^* = \gamma\,\alpha_{\rm W}^{\frac{g+g^{-1}-2}{4}} \tag{2.59}$$

is the tunneling amplitude renormalized by the electron-electron interaction. The dimensionless currents $j_{{\rm M(T)},\gamma^2}$ read

$$j_{\mathrm{M(T)},\gamma^2} = \frac{2}{\pi\alpha_{\mathrm{T}}\alpha_{\mathrm{W}}^{\frac{g+g^{-1}}{2}}} \int_0^\infty d\tau\, Q_{\mathrm{M(T)}}(\tau)\, \sin\left\{4\pi\left[\mathcal{I}^{\Phi_+\Phi_+}(\xi_0;\xi_0;\tau)+\mathcal{I}^{\varphi\varphi}(0;0;\tau)\right]\right\} \times \mathrm{e}^{4\pi\left[\mathcal{R}_{\mathrm{reg}}^{\Phi_+\Phi_+}(\xi_0;\xi_0;\tau)+\mathcal{R}_{\mathrm{reg}}^{\varphi\varphi}(0;0;\tau)\right]} \tag{2.60}$$

where

$$\begin{aligned} Q_{\mathrm{M}}(\tau) &= \sin(u\tau/2)\cos\left[(u_{\mathrm{W}}-u_{\mathrm{T}})\tau\right]+\chi\cos(u\tau/2)\sin\left[(u_{\mathrm{W}}-u_{\mathrm{T}})\tau\right] \qquad (2.61)\\ Q_{\mathrm{T}}(\tau) &= 2\cos(u\tau/2)\sin\left[(u_{\mathrm{W}}-u_{\mathrm{T}})\tau\right]+2\chi\sin(u\tau/2)\cos\left[(u_{\mathrm{W}}-u_{\mathrm{T}})\tau\right] \quad . \end{aligned}$$

Here α_{T} is a small dimensionless cutoff parameter for the tip defined in App. B. The functions $\mathcal{R}_{\mathrm{reg}}^{\Phi_+\Phi_+}(\xi;\xi';\tau)$ and $\mathcal{I}^{\Phi_+\Phi_+}(\xi;\xi';\tau)$ are the real and imaginary parts of the auto-correlation function of the chiral wire field Φ_+ defined in Eqs. (C.7) and (C.8), respectively, while $\mathcal{R}_{\mathrm{reg}}^{\varphi\varphi}(\xi;\xi';\tau)$ and $\mathcal{I}^{\varphi\varphi}(\xi;\xi';\tau)$ are the real and imaginary parts of the correlator of the tip field φ given in Eqs. (C.11) and (C.12). The integral (2.60) is a cut-off independent quantity.

We consider two parameter domains of the three-terminal set-up corresponding to the cases where the tip operates as an electron injector and as a voltage probe, respectively. In the electron injection case, source and drain are at the same electrochemical potential while a bias is applied to the tip. For this configuration the current noise was evaluated in Refs. [47] and [48]. Here we shall explicitly evaluate the non-linear tunneling conductances

$$G_{\mathrm{ST}} \doteq \left.\frac{\partial I_{\mathrm{S}}}{\partial V_{\mathrm{T}}}\right|_{V_{\mathrm{S}}=V_{\mathrm{D}}=0} \tag{2.62}$$

and

$$G_{\mathrm{DT}} \doteq \left.\frac{\partial I_{\mathrm{D}}}{\partial V_{\mathrm{T}}}\right|_{V_{\mathrm{S}}=V_{\mathrm{D}}=0} \quad . \tag{2.63}$$

Conventional Luttinger liquid theory, where the presence of the source and drain electrodes is neglected, predicts that an electron charge injected by tunneling, *e.g.* as a right-mover, into an interacting wire breaks up into separate charge pulses moving in opposite directions, namely a fraction $(1+g)/2$ moving to the right and a fraction $(1-g)/2$ going to the left.[60, 61, 62, 48, 54, 63, 64] This effect originates from the coupling between the densities of right- and left-moving electrons, accounted for by the homogeneous

LL Hamiltonian. As a consequence, one expects that when the tip injects electrons asymmetrically, *e.g.* only toward the drain electrode on the right ($\chi = 1$), the electron-electron interaction would cause a part of the current to flow also to the source electrode on the left.

However, when the source and drain electrodes are explicitly taken into account, our results show that the above expectation is in fact wrong. Remarkably, using Eq. (2.60), one can indeed prove that for $V_S = V_D$ the equality

$$\mathcal{A}(\chi) = \left.\frac{|I_D| - |I_S|}{|I_D| + |I_S|}\right|_{\chi} \equiv \chi \tag{2.64}$$

holds, indicating that for a clean wire the current asymmetry is *independent* of the wire interaction strength g. In particular, for fully asymmetric tunneling ($\chi = 1$), the whole current is injected into the drain electrode, just as in the non-interacting case. This unidirectional charge flow even in the presence of interaction arises from the phenomenon of Andreev-type reflections.[7, 8, 9] Even though charge fractionalization occurs in the bulk of the wire, the plasmonic excitations reaching an interface with the leads experience the mismatch of the interaction strengths in the wire and in the electrode and are thus partly reflected as an oppositely charged excitation. The sum of all reflected pulses at both interfaces restores the property that the whole current flows into the drain, like in the non-interacting wire. This behavior is in fact very similar to an effect occurring in a two-terminal set-up, where the conductance of a wire adiabatically connected to electrodes is $G_{2t} = e^2/h$, independent of the interaction strength. Thus, for perfectly transmitting contacts, it is impossible to extract the interaction constant either from the conductance of a two-terminal set-up or from the current asymmetry in three-terminal measurements.

Nevertheless, in a three-terminal set-up signatures of interaction *do appear* in the behavior of the differential conductances G_{ST} and G_{DT} as a function of the tip-source and tip-drain bias. Figures 2.7(a) and 2.7(b) show G_{ST} and G_{DT} for the case of a tip located in the middle of a wire with interaction strength $g = 0.25$. The various curves correspond to different values of the asymmetry parameter χ, which unbalances the amount of injected right *vs.* left moving electrons. The fully symmetric case ($\chi = 0$) was discussed in Ref. [65]. While for a non-interacting wire G_{ST} and G_{DT} are constant [as can easily be seen from Eqs. (2.54) and (2.55)], in the presence of interaction an oscillatory behavior arises. These oscillations are entirely due to the electron-electron interaction in the wire, which causes Andreev-type reflections even at adiabatic contacts. With increasing χ the conductance G_{ST} decreases until it vanishes for $\chi = 1$, whereas the conductance G_{DT} increases

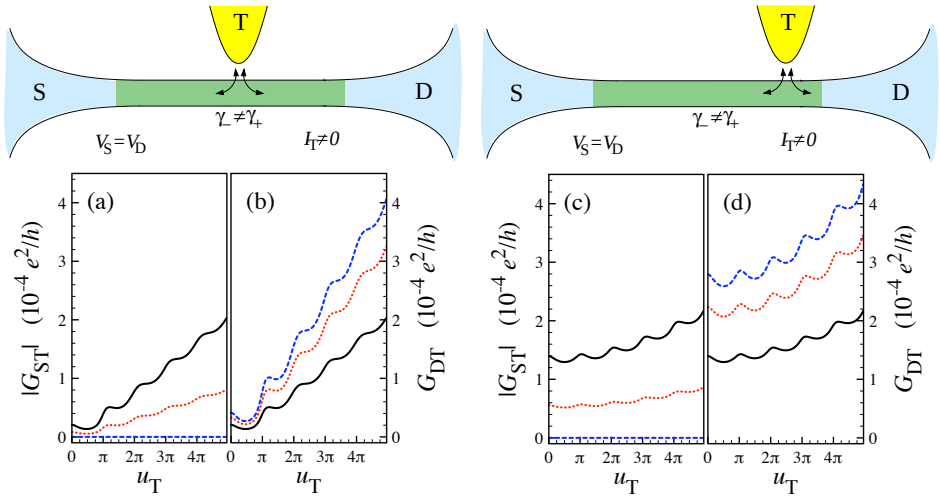

Figure 2.7: Electron injection into an interacting wire. Panel (a) [(b)] shows the tunneling differential conductance $G_{\rm TS}$ [$G_{\rm TD}$] between the tip and source [drain] electrode as a function of the dimensionless tip-source [tip-drain] bias for a wire with interaction strength $g = 0.25$. The various curves refer to different values of the tunneling asymmetry ($\chi = 0$ solid line, $\chi = 0.6$ dotted line, and $\chi = 1$ dashed line). The tunneling strength is $\gamma^* = 0.01$, and the tip is located in the middle of the wire. Panels (c) and (d) are the same as panels (a) and (b) but the tip is located near a contact at $x_0 = 0.45L$.

up to the maximum value for the completely asymmetric case. The relation $G_{\rm ST} = G_{\rm DT}(1-\chi)/(1+\chi)$ between these two conductances is independent of g.

Figures 2.7(c) and 2.7(d) describe the case of an off-centered tip located at $x_0 = 0.45L$. Apparently, the period of the oscillations is the same as in panels (a) and (b) where the tip is in the middle. This is due to the fact that this period is related to the traversal time of plasmonic excitations originating from the tip and interfering at the same point after an even number of Andreev-type reflections at the contacts. This traversal time depends neither on x_0 nor on the asymmetry coefficient.

Let us now discuss the configuration where the tip acts as a voltage probe, *i.e.* when $V_{\rm S} \neq V_{\rm D}$ and $V_{\rm T}$ is set to a value such that $I_{\rm T} = 0$ is fulfilled. In this configuration the quantity on the left hand side of Eq. (2.36) is vanishing, due to Eqs. (2.16) and (2.17). By applying a source-drain bias, one can analyze how the source-drain conductance

$$G_{\rm SD} = \left.\frac{\partial I_{\rm M}}{\partial(V_{\rm S}-V_{\rm D})}\right|_{I_{\rm T}=0} \tag{2.65}$$

is affected by the interaction strength. It is worth emphasizing that in a two-terminal set-up, *i.e.* in the absence of the tip ($\gamma_\pm = 0$), one obtains for a clean wire $G_{\rm SD} = G_{2\rm t} = e^2/h$, independent of the interaction strength. As already mentioned previously, this is due to the fact that, although the electron charge injected by the source splits up in fractions through the interaction-induced Andreev-type reflections at the contacts, in a clean wire the series of these fractions always sums up to e, disguising the interaction effects in the dc average current.[7] Our results show that a quite different behavior emerges for a three-terminal set-up, even in the configuration where the tip does not inject any net current into the wire. Figure 2.8(a) shows $G_{\rm SD}$ as a function of the source-drain bias, for different values of the interaction strength, ranging from a non-interacting to a strongly interacting wire. The left panel refers to the case of symmetric tunneling $\chi = 0$, whereas the right one analyzes the role of a tunneling asymmetry. As one can see, the effects of interaction in the wire become observable through the voltage probe, since oscillation of $G_{\rm SD}$ originating from Andreev-type reflections emerge. Notice that at constant bare tunneling amplitude γ the zero bias conductance is higher in the presence of interaction than for a non-interacting wire, since the renormalization (2.59) of the tunneling amplitude suppresses γ. With increasing tunneling asymmetry [see Fig. 2.8(b)], the differences between interacting and non-interacting wires become less pronounced, and indeed the oscillations are washed out for fully asymmetric tunneling $\chi = \pm 1$.

The dimensionless tip voltage $\bar{u}_{\rm T} = (e/\hbar\omega_L^*)\bar{V}_{\rm T}$ ensuring $I_{\rm T}$=0 shows an interesting dependence on the source-drain bias. In the limiting cases of symmetric and completely asymmetric tunneling this dependence coincides for interacting and non-interacting wires (namely $\bar{u}_{\rm T} = u_{\rm W}$ for $\chi = 0$ and $\bar{u}_{\rm T} = u_{\rm W} \pm u/2$ for $\chi = \pm 1$). For intermediate values of the asymmetry parameter χ the tip voltage $\bar{u}_{\rm T}$ shows an oscillatory behavior with period $\Delta\bar{u}_{\rm T} = 2\pi$ as a function of the source-drain bias. We also see that the period of $G_{\rm SD}$ in Fig. 2.8 is twice as large as the period of $G_{\rm TS}$ and $G_{\rm TD}$ in Fig. 2.7 where the tip is in the electron injection configuration. This is due to the fact that in Fig. 2.8 the source-drain bias is applied symmetrically ($u_{\rm W} = 0$) while in Fig. 2.7 source and drain are both grounded and the bias is only applied to the tip.

Finally, we emphasize again the difference between the electron injection and the voltage probe configurations of the tip: While in the former case an asymmetry in tunneling does not spoil the observation of effects of electron-electron interaction (see Fig. 2.7), in the latter case interaction-induced oscillations can be best observed for symmetric tunneling and they are in fact vanishing for fully asymmetric tunneling.

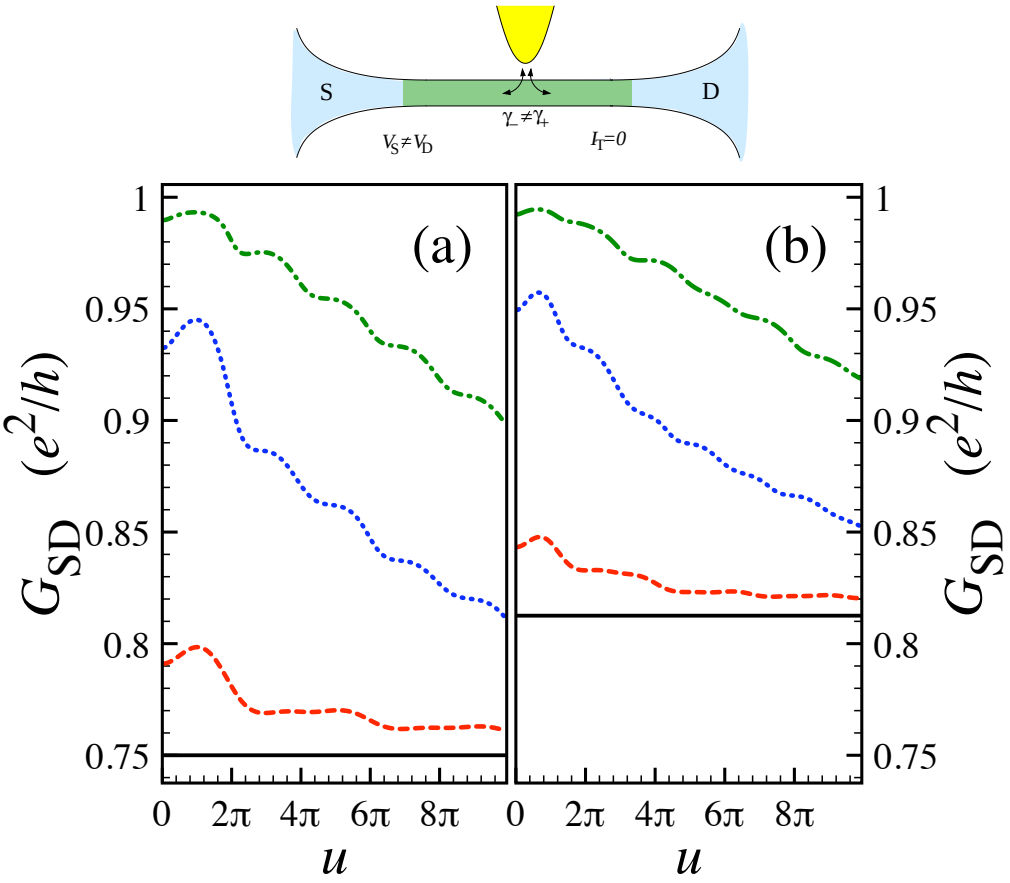

Figure 2.8: The effect of the tip in the voltage probe configuration on the zero temperature conductance is shown as a function of the source-drain bias. Panel (a): the case of symmetric tunneling ($\chi = 0$). Panel (b): the case of an asymmetry in tunneling ($\chi = 1/2$). Different curves refer to different values of the interacting strength: non-interacting ($g = 1$, solid curve), weakly interacting ($g = 0.7$, dashed curve), moderately interacting ($g = 0.4$, dotted curve), and strongly interacting ($g = 0.25$, dashed-dotted curve). The bare tunneling strength is $\gamma = 0.5$ and the dimensionless cutoff parameter is $\alpha_W = 10^{-3}$.

2.3.3 Interaction effects on electron tunneling from the tip: The case of a wire with non-ideal contacts

In this section we analyze the three-terminal transport properties in the presence of electron-electron interaction, contact impurity scattering and electron tunneling from the tip. In particular, we discuss how a finite contact resistance modifies the Andreev-type oscillations of the tunneling conductances, previously discussed for the case of adiabatic contacts ($\lambda_i = 0$). We present results obtained by perturbation theory for weak contact impurities λ_i, and tunneling amplitudes $\gamma_\pm$. Technical details can be found in the Appendices. The currents may be written as

$$I_{\rm M} = I_0 + I_{\rm imp} + I_{{\rm M},\gamma^2} + I_{{\rm M},\gamma^2\lambda} \tag{2.66}$$

and

$$I_{\rm T} = I_{{\rm T},\gamma^2} + I_{{\rm T},\gamma^2\lambda} \tag{2.67}$$

Here $I_0 = (e^2/h)(V_{\rm S} - V_{\rm D})$ is the current of an ideally contacted wire in the absence of the tip, whereas $I_{\rm imp}$ is the leading order term accounting for non-ideal contacts [see Eq. (2.45)]. In general, this latter term involves both Fabry-Pérot and Andreev-type oscillations. Both, I_0 and $I_{\rm imp}$, vanish when the electrochemical potentials for source and drain electrodes are equal ($V_{\rm S} = V_{\rm D}$); alternatively, they can be easily determined by measuring the current-voltage characteristics in the absence of the tip. Henceforth, we shall focus on contributions to the currents arising from the presence of the tip. The leading order terms $I_{{\rm M},\gamma^2}$ and $I_{{\rm T},\gamma^2}$, given by Eq. (2.58), describe tunneling into an ideally contacted wire and contain only Andreev-type oscillations. The next-to-leading order terms ($\gamma^2\lambda$, $\gamma^2\lambda^2$, ...) also exhibit oscillations originating from interference between backscattering at the contacts and tunneling to/from the tip. Such oscillations, though modified by the interaction, are already present in a non-interacting wire, unlike the Andreev-type oscillations of the leading order terms (γ^2), that are instead entirely due to the interaction. We thus analyze how interaction affects the terms $I_{{\rm T(M)},\gamma^2\lambda}$, which represent the most relevant correction to the Andreev-type oscillations discussed above. These terms describe up to leading order the interplay between electron injection at the tip and backscattering at the S and D contacts.

Explicitly one finds

$$I_{{\rm M(T)},\gamma^2\lambda} = \frac{e\omega_L^*}{2\pi}(\gamma^*)^2\,\lambda^*\sqrt{1-\chi^2}\; j_{{\rm M(T)},\gamma^2\lambda} \tag{2.68}$$

where $\lambda^* = \lambda^*_{\rm B,1} + \lambda^*_{\rm B,2}$, and

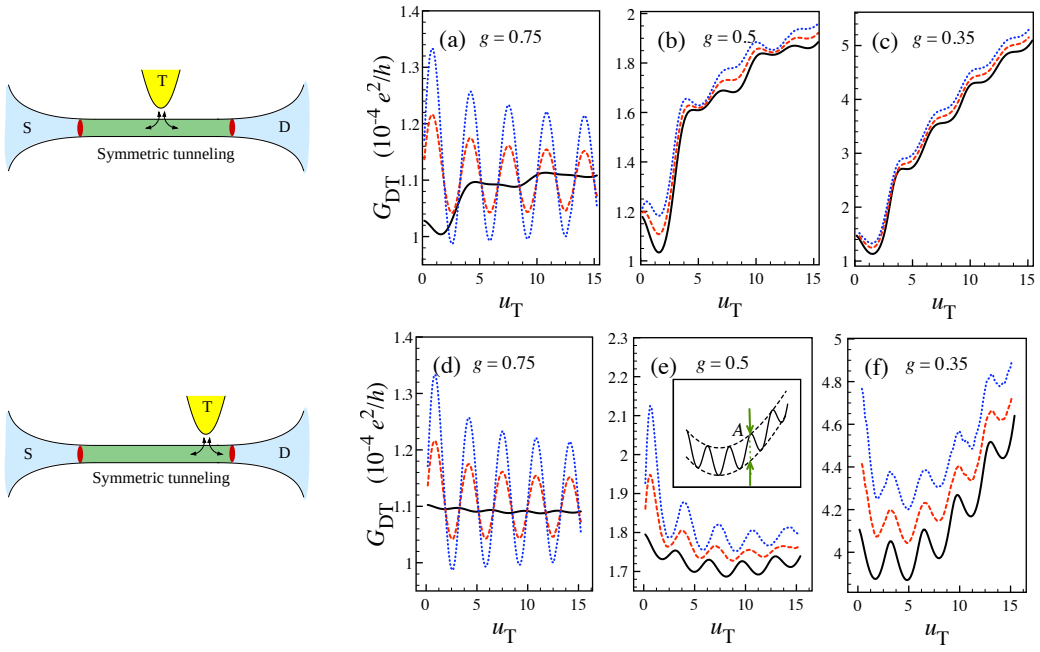

Figure 2.9: Zero temperature non-linear tip-drain conductance $G_{\rm DT}$ as a function of the tip bias for tunneling amplitude $\gamma^* = 10^{-2}$ and symmetric tunneling $\chi = 0$. The upper panels (a), (b) and (c) are related to a tip in the middle of the wire ($x_0 = 0$), whereas the lower ones (d), (e) and (f) to a tip located at $x_0 = 0.45L$. Panels pairs (a) and (d), (b) and (e), and (c) and (f) describe the case of a wire with weak ($g = 0.75$), moderate ($g = 0.5$), and strong ($g = 0.35$) interaction strength, respectively. In each panel the different curves refer to different contact impurity strengths. The solid curves describe the case of ideal contacts where the oscillations are purely Andreev-type. The dashed [dotted] lines refer to finite contact impurity strength $\lambda^*_{{\rm B},1} = \lambda^*_{{\rm B},2} = 0.1$ [$= 0.2$]. For a weakly interacting wire the conductance oscillations are mostly due to the conventional interference between backscattering at the contacts and tip tunneling, and Andreev-type oscillations become visible only for extremely low contact resistance. In contrast, for stronger interaction strength a finite contact resistance is sufficient for the oscillations to be attributed to Andreev-type processes. The inset of panel (e) shows the definition of the average amplitude referred to in the text.

$$
\begin{aligned}
j_{{\rm M(T)},\gamma^2\lambda} = &- \frac{1}{2\pi\alpha_{\rm W}^{\frac{g+g^{-1}+6}{4}}\alpha_{\rm T}} \sum_{i=1,2} \frac{\lambda^*_{{\rm B},i}}{\lambda^*} \iint_{-\infty}^{+\infty} d\tau_1 d\tau_2 \Big\{ \\
&\cos\left[(u_{\rm S}-u_{\rm T})\tau_1 + (u_{\rm T}-u_{\rm D})\tau_2 - 2(\kappa_{\rm W} + g u_{\rm W} - g u_{\rm G})(\xi_0 - \xi_i)\right] \\
&\times {\rm e}^{4\pi[\mathcal{R}_{\rm W}(\xi_0;\xi_i;\tau_1;\tau_2)+\mathcal{R}_{\rm T}(\tau_1;\tau_2)]} \sum_{\eta_1,\eta_2=\pm} P^{\eta_1\eta_2}_{\rm M(T)}\, F^{\eta_1\eta_2+}_{{\rm W},\gamma^2\lambda}(\tau_1;\tau_2)\, F^{\eta_1\eta_2}_{{\rm T},\gamma^2\lambda}(\tau_1;\tau_2) \\
&\times \sin\left\{4\pi\left[\mathcal{I}^{\eta_1\eta_2+}_{\rm W}(\xi_0;\xi_i;\tau_1;\tau_2) + \mathcal{I}^{\eta_1\eta_2}_{\rm T}(\tau_1;\tau_2)\right]\right\} \Big\}
\end{aligned}
\tag{2.69}
$$

where

$$P_{\rm M}^{\eta_1\eta_2} = \eta_2 + \eta_1 - 2\eta_1\eta_2 \tag{2.70}$$

$$P_{\rm T}^{\eta_1\eta_2} = 2(\eta_2 - \eta_1)\,. \tag{2.71}$$

The functions $F^{\eta_1\eta_2\eta_3}_{{\rm W},\gamma^2\lambda}(\tau_1;\tau_2)$ and $F^{\eta_1\eta_2}_{{\rm T},\gamma^2\lambda}(\tau_1;\tau_2)$ are defined in App. B in Eqs. (B.8) and (B.24), respectively, and the functions $\mathcal{R}_{\rm W}(\xi_0;\xi_i;\tau_1;\tau_2)$, $\mathcal{I}_{\rm W}(\xi_0;\xi_i;\tau_1;\tau_2)$, $\mathcal{R}_{\rm T}(\tau_1;\tau_2)$ and $\mathcal{I}_{\rm T}(\tau_1;\tau_2)$, accounting for the real and the imaginary parts of several correlation functions in the wire and in the tip, are defined in App. C in Eqs. (C.1), (C.2), (C.11) and (C.12), respectively.

For simplicity, we limit the analysis of Eqs. (2.68) and (2.69) to the electron injection configuration where source and drain are grounded. We start with the case of symmetric tunneling ($\chi = 0$).

As already observed in Sec. 2.2 for a noninteracting wire, the term (2.68) leads to additional oscillations in the differential conductance of the three-terminal set-up. These conventional oscillations are characterized by two periods related to the distances between the tip and the contact impurities, so that the pattern depends on the tip position. Electron-electron interaction modifies this pattern reducing the amplitude of the conventional oscillations and giving rise to additional Andreev-type oscillations. The case of a tip in the middle of the wire is shown in the upper panels (a), (b) and (c) of Fig. 2.9, where the differential conductance $G_{\rm DT}$ is plotted as a function of the tip bias $u_{\rm T}$ for three different values of interaction strength, ranging from weak ($g = 0.75$), over moderate ($g = 0.5$) to strong interaction ($g = 0.35$), as displayed in the three panels. In each panel the solid curve refers to the case of ideal contacts where the oscillations are purely of Andreev-type. The dotted and dashed curves describe the effect of finite contact resistances arising from the contribution of the term (2.68). As one can see from panel (a), for weak electron-electron interaction the conventional oscillations dominate and mask the Andreev-type oscillations. In this case, only extremely good contacting might allow the identification of Andreev-type processes. However, for moderate interaction strength [panel (b)], the two types of oscillations have comparable amplitudes, and for strong interaction [panel (c)] the conventional oscillations are strongly suppressed while the term (2.68) only causes a small shift of the conductance value. The oscillations of $G_{\rm DT}$ are essentially Andreev-type.

A similar effect occurs when the tip is closer to one of the contacts displayed in the lower panels (d), (e) and (f) of Fig. 2.9. The main difference is that in this case the pattern of the Andreev-type oscillations is more sinusoidal, even for weak interactions.

g	0.4	0.5	0.6	0.7	0.8
$\lambda_{\rm C}^*$	0.2	0.02	$4 \cdot 10^{-3}$	$4 \cdot 10^{-4}$	10^{-4}

Table 2.1: Crossover value of the (renormalized) contact impurity strength $\lambda_{\rm C}^*$, below which oscillations can be attributed to Andreev-type processes, for various values of the interaction strength g. The tip is located at $x_0 = 0.45L$, as in the lower panels of Fig.2.9.

Our result indicates that, for a wire with a given interaction strength, there is crossover value $\lambda_{\rm C}^*$ of the (renormalized) contact resistance, below which the oscillations of the non-linear conductance can essentially be attributed to Andreev-type processes. We have quantified $\lambda_{\rm C}^*$ for the case of a tip close to the contacts, where the regularity of oscillations allows for a straightforward determination of their amplitude, defined as the average distance between maxima and minima, as schematically displayed in the inset of Fig. 2.9(e). The crossover impurity strength $\lambda_{\rm C}^*$ is then simply determined by the value of λ^* for which the amplitude $A_{\gamma^2\lambda}$ of the conventional oscillation term $I_{{\rm T},\gamma^2\lambda}$ [see Eq. (2.68)] equals the amplitude A_{γ^2} of the Andreev-type oscillation term $I_{{\rm T},\gamma^2}$ [see Eq. (2.58)]. The result is given in Table 2.1 for different values of interaction strength. For contact impurity strength $\lambda^* \leq \lambda_{\rm C}^*$ the oscillations of the non-linear conductance are essentially of Andreev-type.

Let us finally briefly consider the case of asymmetric tunneling $\chi \neq 0$. An important result is that, in view of Eq. (2.68), the contribution to the current of order $\gamma^2\lambda$ vanishes in the case of totally asymmetric tunneling ($\chi = \pm 1$). This property is thus robust with respect to electron-electron interaction within the Luttinger liquid picture. In fact, one can show that in this case only perturbative contributions of order $\gamma_i^{2n}(\lambda_1\lambda_2)^{n+m}$ ($n = 1, 2, 3, \ldots; m = 0, 1, 2, \ldots$) are non-vanishing.

2.4 Discussion and Conclusions

In order to facilitate the discussion, we propose to the reader different perspectives from which our results can be considered.

The effects of electron-electron interaction on Fabry-Pérot oscillations. The origin of Fabry-Pérot oscillations boils down to quantum interference between electron backscattering at two (or more) impurities. As a consequence, this phenomenon is present also in a non-interacting quan-

tum wire (see Sec. 2.2), where the oscillations appear both as a function of the source-drain bias and as a function of the gate voltage. The interference pattern is modified by electron-electron interaction, which introduces a power-law suppression of the amplitude and, especially for $g < 1/2$, deforms the sinusoidal shape towards a saw-tooth-like shape (see Fig. 2.5). Interaction also leads to a (partial) screening of the charge in the wire[59], causing a change of the oscillation period as a function of the gate bias with respect to the period as a function of the source-drain bias. This effect suggests an operative procedure to extract the Luttinger liquid parameter g from measurements of the non-linear conductance in the Fabry-Pérot regime (see Fig. 2.6). The effects of an asymmetrically applied source-drain bias have also been discussed.

Conventional vs. Andreev-type oscillations. Besides modifying Fabry-Pérot oscillations, electron-electron interaction also yields another major effect, which is absent in a non-interacting wire: at the wire-electrode interfaces, plasmon excitations are partially reflected due to the mismatch of interaction strengths in the interacting wire and the non-interacting electrodes. This effect, entirely due to interaction, occurs also for ideally contacted adiabatic interfaces and gives rise to a different type of oscillation, termed Andreev-type oscillations[10, 57] since the incoming charge and the fractional charge reflected at the contact have opposite signs, just as at an interface between a normal metal and a superconductor. In real experiments with interacting quantum wires in the Fabry-Pérot regime, the current-voltage characteristics will in general exhibit both conventional Fabry-Pérot oscillations, i.e. oscillations that are already present in a non-interacting wire and that are simply *modified* by interaction, and Andreev-type oscillations, purely *originating* from interaction. The interesting question arises whether one can distinguish between these two oscillatory phenomena in an operative way and, in particular, whether it is possible to determine regimes and conditions, under which the latter can be observed.

Since the amplitude of Fabry-Pérot oscillations is roughly proportional to the reflection coefficients of the contacts whereas Andreev-type processes occur even with ideal interfaces, one might at first think that with improving transparency of the contacts the non-linear conductance of a two-terminal set-up would exhibit a predominance of Andreev-type oscillations over the conventional Fabry-Pérot ones. However, this is not the case, since for an ideally contacted wire the sum of all Andreev-type reflection processes at the two interfaces exactly recovers the injected pulse, when the sign of all reflected charge pulses is taken into account. The transmission of an interacting wire

adiabatically connected to non-interacting leads turns out to equal 1, as was pointed out in Refs. [7] and [8, 9]. Although Andreev-type oscillations of the conductance do appear in the presence of even a single impurity[10, 57], their amplitude is proportional to the impurity reflection coefficient. This implies that two-terminal set-ups are not suitable to distinguish between Andreev-type and Fabry-Pérot oscillations, since both oscillations have the same dependence on the impurity strengths $\lambda^*_{\mathrm{B},i}$. Furthermore they also exhibit the same period as a function of the source-drain bias.

In contrast, our analysis suggests that a three-terminal set-up may allow one to distinguish Andreev-type oscillations from conventional oscillations. As far as Andreev-type oscillations are concerned, three-terminal set-ups indeed offer one important advantage with respect to two-terminal ones: in the presence of a third electrode, Andreev-type oscillations appear even for the ideal case of a wire adiabatically connected to the source and drain electrodes (λ_i=0). In the presence of interaction the tip-source and tip-drain non-linear conductances G_{ST} and G_{DT} oscillate as a function of the tip voltage u_{T} already to leading order γ^2 in the tunneling amplitude, independent of contact impurity strengths λ_i. This effect holds when the tip acts as an electron injector (see Fig. 2.7) as well as when it acts as a voltage probe (see Fig. 2.8), and the oscillations vanish for a non-interacting wire [see Eqs. (2.54) and (2.55)]. Thus, quite differently from a two-terminal set-up, in three-terminal set-ups Andreev-type oscillations become more visible when the contact transparency is improved.

In view of the fact that in realistic experiments the contact resistance is always finite, we have quantitatively evaluated the influence of the contact resistance on the conductance oscillations [see Eq.(2.69)] showing that additional Fabry-Pérot-type oscillations superimpose with the Andreev-type ones (see Fig.2.9). We have thus put forward criteria for observing the interaction induced Andreev-type oscillations. At least two experimental situations are promising: For the conventional case of symmetric tunneling from the tip, we have determined typical values of the contact resistance below which the oscillations in the current-voltage characteristics can essentially be attributed to Andreev-type phenomena. The result, shown in Table 2.1, indicates that the stronger the interaction of the wire the larger are the contact resistances that are tolerable in order to still observe Andreev-type oscillations. Furthermore, in the case that the set-up allows for fully asymmetric tunneling, the leading order correction (2.69) competing with the Andreev-type term is vanishing, *even in the presence of interaction.*

In summary, in systems like carbon nanotubes where the interaction strength is typically strong, $g \simeq 0.2 - 0.3$, while electron injection from an STM tip is typically symmetric, Andreev-type oscillations may be ob-

served by achieving a high quality of the contacts to the leads. In contrast, in semiconductor quantum wires, where the interaction strength is usually moderate $g \simeq 0.6 - 0.7$, asymmetric tunneling induced by a magnetic field is more suitable for observing Andreev-type oscillations.

The effects of asymmetric tunneling. The above-mentioned case of asymmetric tunneling merits some further remarks. Recent experiments by Yacoby and co-workers[41, 42, 51] have shown that fully asymmetric tunneling into semiconductor-based quantum wires can be realized by appropriate tuning of a magnetic field. Inspired by these experiments, we have considered the possibility of an asymmetry in electron tunneling from the tip. Before discussing our results we would like to point out the relation between our model and Yacoby's experimental set-up. While Yacoby *et al.* study electron tunneling between two parallel wires where momentum conservation is required, our model considers injection from a point-like tip. Although these two situations may at first seem incompatible, a regime can be determined where they are equivalent. In the experiments of Refs. [41, 42, 51] electrons are injected from an upper shorter wire with length L_u into a lower longer wire with length L_l. Since the tunneling region reasonably coincides with the length of the short wire, momentum conservation only holds up to an uncertainty $\delta k \sim 1/L_u$. Although this uncertainty is small enough to select a specific electron momentum state in the upper wire, δk may be much bigger than the mean level spacing of the lower wire, if the latter is much longer than the former ($L_l \gg L_u$). In this regime, while the electron wave function behaves like a plane wave for the short wire, for the long wire it can effectively be considered as a localized wave packet, and our model thus applies.

Under these conditions several interesting effects emerge. In the first instance, by using the tip as an electron injector, the tunneling asymmetry can be exploited to gain the transmission coefficient of each contact by measuring the current asymmetry (2.36) in the two cases of tunneling purely to the right ($\chi = +1$) and to the left ($\chi = -1$), as has been shown in Eq. (2.40). Secondly, when the tip is used in the configuration of a voltage probe, fully asymmetric tunnelling allows us to eliminate the suppression of the source-drain conductance $G_{\rm SD}$, which occurs for symmetric tunneling. Similarly, $G_{\rm SD}$ becomes independent of the tip position.

When electron-electron interaction is taken into account, the scenario is even richer. Luttinger liquid theory predicts that electron-electron interaction induces a current asymmetry which depends on the interaction strength g. The appealing question arises whether this effect is observable in experiments, where currents are measured not directly in the interacting wire but

in metallic electrodes connected to it.

Here we have scrutinized this question by taking the presence of source and drain electrodes into account in a fully consistent manner within the inhomogeneous Luttinger liquid model. Considering as a test bench the case of a wire adiabatically contacted to source and drain electrodes, we have proven that, although charge fractionalization does occur in the bulk of the wire, the sum of Andreev-type reflection processes at the contacts leads to a current asymmetry $\mathcal{A}$ that is *independent* of the electron-electron interaction strength, just as it is the case with the two terminal conductance $G_{2\mathrm{t}}$. Thus, already for this ideal case, no proof of charge fractionalization can be gained from the analysis of $\mathcal{A}$, or from the ratio $e^2\mathcal{A}/(hG_{2\mathrm{t}})$. [4] We have also shown that, nevertheless, interaction effects do appear in the behavior of the nonlinear conductance, where interaction induced oscillations arise as a function of the tip-source and tip-drain bias. It is worth emphasizing that this feature is due to the three-terminal set-up, since the two-terminal conductance of a Luttinger liquid ideally contacted to leads is independent of the source-drain bias.

[4]The investigation carried out in Ref. [54], based on the assumption that the interfaces between the interacting wire and the electrodes can be treated phenomenologically with a transmission coefficient *à la* Landauer-Büttiker, has led these authors to the claim that the interaction strength can be observed via the current asymmetry. We believe that our approach takes the nature of the leads into account more thoroughly.

Part II

Quantum Transport Through Nanoelectromechanical Systems

Chapter 3

Quantum nanomechanical systems and superconducting circuits

3.1 Nanomechanical oscillators and their quantum regime

The last few decades have witnessed a rapid development of nanotechnologies. The ability to produce nanoscopic samples of specific shape or composition, printing suitable patterns onto high-quality substrates, has made it possible to test the validity of physics paradigms in a regime that was previously inaccessible: the scale at which quantum coherence plays an important role.

However, one of the most relevant boosts in this field came from the perspectives of potential technological applications. Integrated circuitry was at the base of mass production and diffusion of information devices such as personal computers and calculators; higher efficiency and lower costs demanded an ever-decreasing size of circuit elements, so that the celebrated Moore's law, predicting an exponential decrease in transistors' size, has held now for more than forty years.

Among other relevant directions in which micro- and nano-fabrication found important applications is micromechanics. The Scanning Tunnel Microscope, for instance, exploits the possibility of having very sharp (one or very few atoms wide) metallic tips whose position can be controlled with very high accuracy; by facing such tips at the surface of some sample held at a different electric potential, one finds that an electrical current flows through a vacuum into the sample and that the amplitude of this current is exponentially sensitive to the distance between the tip and the sample. Thanks

to micromechanics and quantum tunneling, one can easily take pictures of a sample at atomic resolution. Another example is the Atomic Force Microscope, which is an improvement of the Scanning Tunneling Microscope; in this device a tip is suspended so that its vertical position depends on how strongly the sample surface attracts the tip itself: the position of the tip is detected by attaching a mirror onto it and shining a light beam. These are just two examples of how control in shaping very sharp tips and very small beams can open new ways of dealing with the world of nanoscopic samples, but they effectively convey a timely picture of how the problem of characterizing a nanobeam and detecting its position is usually tackled: the two main roads consist in coupling the nanodevice with an electrical current or with a coherent light beam.

Although the development of nanotechnologies was pushed by the need for technological advances, it gave physicists new ground for the investigation of nature. Indeed a suspended nanoscale structure of high quality in a cryogenic environment is likely to display quantum features in its dynamics, in much the same way as low-temperature nanocircuits obey the law of quantum mechanics. For the first time in history, nanomechanics gives us the opportunity to investigate some of the most intriguing fundamental questions raised after the birth of quantum mechanics, such as the existence of quantum superposition of states for macroscopic objects, in real mechanical systems.

The dynamics of a rigid body with one (cantilever) or two (doubly-clamped beams) fixed edges is best described in terms of oscillations around a configuration at rest. In classical mechanics it is standard to assume that for small deviations from the equilibrium position, the restoring (generalized) force is linear in the (generalized) displacement; this hypothesis gives rise to the well-known theory of small oscillations. In the description of nanomechanical systems it is customary to decompose the complex motion of these rigid bodies into many different decoupled modes, in a similar way as what one does for crystal deformations in a solid; each mode coordinate obeys the usual harmonic-oscillator equation with its own frequency. In order to obtain a quantum description of the dynamics of such systems, one merely employs the correspondence principle by introducing one pair of bosonic creation and annihilation operators for each mode, so that each describes a quantum harmonic oscillator. The use of the correspondence principle assures that for high temperatures the quantum description coincides with the classical one; however truly quantum features will emerge as the temperature is decreased below a certain threshold. An estimate for such a threshold is found by

requiring that the average thermal occupation number is of order unity:

$$n_{\rm th} = \frac{1}{e^{\hbar\omega/k_B T} - 1} \approx 1 \quad \Longrightarrow \quad k_B T \lesssim \hbar\omega \tag{3.1}$$

Eq. (3.1) makes it apparent why nanomechanics is required in order to observe quantum dynamics in actual mechanical systems: the order of magnitude of frequencies corresponding to such a requirement for a temperature of 10mK is $\omega \approx 2\pi \times 200$ MHz, which is very difficult to obtain in macroscopic objects; however, the typical scaling law for the eigenfrequencies of a rigid body follows the relation for massive springs $\omega \simeq \sqrt{k/m}$, where k is the spring constant and m is the mass, therefore nanoscopic pieces of a rigid material can reach this limit.

Nanomechanical resonators are likely to become a new test bed for Quantum physics. Despite their small size, these devices can still be considered as macroscopic, since the number of degrees of freedom needed for a description of their dynamics is very large. Therefore a definite demonstration of quantum behavior of such systems would be a nice step towards a confirmation that standard Quantum Theory applies to macroscopic objects as well.

By "quantum behavior" we mean that some experimental procedure results in some measurement output that obeys the rules of Quantum physics while not beeing easily accounted for with those of Classical physics. Two orders of problems have to be tackled in order to reach such a goal: on the one hand we must be able to prepare the device in a state in which the expectation values of some observables are not "classical"; on the other hand we need to produce some measurement scheme and some experimental apparatus that can detect this non-classicality.

The first order of problems comprises the previously mentioned issue of cooling: equilibrium thermal states of high temperature display only classical values of physical observables and their correlations. Given the possibility of having a cold nanomechanical system, one can employ the coupling to some external field, or other controllable quantum systems, to produce a suitable dynamics resulting in some known exotic quantum state, such as minimum-uncertainty states (coherent states), squeezed states, high-phonon-number Fock states, and so on.

As an example, consider a squeezed state. This kind of state is obtained by applying to a known quantum state a unitary transformation that corresponds to the canonical transformation $q \to q/k$, $p \to kp$; this is realized in the quantum formalism by the unitary operator $U = \exp\{i \log k(qp+pq)/2\hbar\}$. Suppose we can control the dynamics of the device in such a way that the time evolution has the form of a squeezing operator of tunable parameter k; we can then measure repeatedly the position of the nanomechanical oscillator

for a fixed value of the squeezing parameter and compute the inaccuracy of the measurement. One should find that this inaccuracy depends only on the value of the squeezing parameter, and therefore is not related to the measurement apparatus. Squeezed states have been demonstrated long ago for the electromagnetic field in an optical cavity [66].

Another interesting example is a Fock state. Fock states are eigenstates of the operator representing the number of excitations in a harmonic oscillator (the photons in an optical cavity or the quanta of vibrations in a mechanical oscillator, usually referred to as phonons). Although it has turned out to be rather difficult to engineer arbitrary superpositions of Fock states in optical cavities [67], it has been recently demonstrated for microwave superconducting cavities [68], which is very promising for application to nanoelectromechanical systems in view of the good coupling that has been recently demonstrated between such systems and a phase qubit [69] (this was used to prove the first nanomechanical system in its quantum ground state).

The second order of problems is related to the accurate detection of the oscillator's position. The accuracy required to test the validity of the theory must be of the order of $\sqrt{\hbar/2m\omega}$, which is the typical length scale at which quantum features of the system state appear. Although this is a trivial upper bound, a simple application of Heisenberg's uncertainty inequality shows that it is also a lower bound for a very large class of the possible measurement schemes. Following Caves [70], suppose that we want to detect the position of an harmonic oscillator with a measurement apparatus with an intrinsic inaccuracy σ, and that we use this apparatus to make repeated measurements of the position. Just after the first measurement, the oscillator is left in a state in which $\langle(\hat{x}-\bar{x})^2\rangle \leq \sigma^2$. The inaccuracy of the second measurement (at time t) will be:

$$\begin{aligned}\Delta_2^2 =&\sigma^2 + \langle(\hat{x}(t)-\bar{x}(t))^2\rangle \geq \langle(\hat{x}(0)-\bar{x}(0))^2\rangle + \langle(\hat{x}(t)-\bar{x}(t))^2\rangle \geq \\ &\geq 2\sqrt{\langle(\hat{x}(0)-\bar{x}(0))^2\rangle\langle(\hat{x}(t)-\bar{x}(t))^2\rangle} \geq |\langle[\hat{x}(0),\hat{x}(t)]\rangle|\end{aligned} \tag{3.2}$$

In the case of the harmonic oscillator, it is known that $\hat{x}(t) = \hat{x}(0)\cos(\omega t) + \hat{p}(0)/\omega m \cdot \sin(\omega t)$, therefore $\Delta_2^2 \geq \hbar/m\omega \cdot |\sin(\omega t)|$. Repeated measurements of the position taken at random times cannot in general have uncertainties much smaller than $\sqrt{\hbar/m\omega}$, a quantity which is therefore called *Standard Quantum Limit*. The above derivation illustrates how the Standard Quantum Limit originates from Heisenberg's uncertainty relation between the observable at different times; the actual value of the intrinsic inaccuracy σ is totally irrelevant: using a detector with a smaller inaccuracy, produces the same results.

However the inaccuracy due to the quantum nature of an object strongly

depends on the observable we want to measure, and specifically on its commutation relation with the Hamiltonian of the system. Indeed if we want to observe a quantity that is an integral of motion, and we can employ a detector with no inaccuracy, then after the first measurement the system will remain in an eigenstate of this observable and subsequent outcomes of the measurement procedure will always yield the same result. This is an example of a Quantum Non-Demolition measurement (see for instance [71]). A less trivial example for the case of the harmonic oscillator is the repeated measurement of position at time intervals that are multiple of $2\pi/\omega$ (in [71] these are called Stroboscopic QND observables); in this case the upper bound (3.2) becomes trivial and the main source of inaccuracy will be the intrinsic one σ.

For historical reasons the first detection technique to be developed for high-precision position detection was based on interferometry of optical light; the Michelson interferometer was devised in the late nineteenth century for this purpose, when highly coherent light was not yet available. Laser light, then, offered the opportunity of reaching unprecedented precision thanks to the availability of highly-collimated, very bright light beams. In the field of gravitational wave detection, for instance, this fact has been exploited for using interferometers with very long arms in which the two branch of a laser beam bounce back and forth several times before they are recombined to interfere. This can be used to detect a change in the distance between the mirrors at the end of the two arms which is of the order of 10^{-18}m at frequencies of some hundred Hertz (a frequency that is expected for collapsing binary neutron-star systems)[72]. Although this is about the amplitude of quantum zero point motion for a mirror of 1kg mass and 1Hz proper frequency, we cannot expect to observe quantum motion in such a system since it would be too difficult to cool down to the required temperature.

However, laser light can be used in table-top experiments for detecting the position of micrometer-sized mechanical oscillators, based on very similar principles. Indeed high quality optical cavities (Fabry-Pérot cavities) can be produced by letting a spherical mirror face a reflecting cantilever, acting as a moving mirror. Changing the length of the cavity produces a shift in the sharp resonance peaks characterizing it and this change can be used to extract information about the position of the oscillator [73]. One way is to measure the transmission amplitude close to the cavity's resonant frequency: since the transmission has a lorenztian peak in correspondence with the resonant frequency, a shift in the mirror position results in an increasing or decreasing transmission; for this scheme it is best to use an input field at whose frequency the unperturbed transmission of the cavity is about half its maximum, so that the derivative of the transmission with respect to the

mirror's position is maximum. One drawback of this scheme is the following: since the total energy stored in the cavity depends on the amplitude of the field inside it and since a change in the mirror's position changes the amplitude of the field inside the cavity, it therefore also produces a force acting on the mirror, already at a classical level. To avoid this, one could tune the external-field frequency to a value close to the cavity's proper frequency: in this case the amplitude of the field will change quadratically with the mirror's displacement; however, in passing from being red-detuned to being blue-detuned, the phase of the external field at the output changes its sign. The second scheme is then to measure the phase difference between the incoming and outgoing (or reflected) field.

These ideas can be implemented in principle in microscopic devices, using cantilevers as mirrors and optical fibers to convey laser light; micromechanical resonators have higher resonant frequencies and can get closer to their quantum ground state. Specific feedback mechanisms can be used for instance to cool the mirrors down, both actively and passively [74, 75, 76]. Downscaling these devices is not straightforward since optical radiation manifests diffractive effects when hitting obstacles of 1μm size, as this is roughly the wavelength of the radiation [77]. An alternative approach for exploiting the high control of coherent light in the optical range to measure position of quantum mechanical oscillator, overcoming the diffraction limit, is through near-field effects. In dielectric cavities the confined electromagnetic field can be coupled to external media by means of its evanescent tails; this principle has been employed for demonstrating position detection above the Standard Quantum Limit for mechanical resonators thinner than the wavelength of the radiation used for detection [78].

The second major way to manipulate nanomechanical objects is by coupling them to some electric circuit by means of electromagnetic forces; the devices implementing this idea are referred to as nanoelectromechanical systems, or NEMS for brevity. Although this working principle has long been known and technological applications date back to the XIX century, the difficulties in dealing with integration of nanomechanical parts in electrical circuits prevented the first NEMS from being realized prior to the 1990's [79, 80]. The nanomechanical suspended bridges that are free to oscillate are usually made of a semiconducting material; in order to obtain good coupling with electrical degrees of freedom they can be covered with thin layers of metal, thus becoming conducting.

The possible coupling schemes can be based on the action of a magnetic field or of an electrical field. A possible implementation based on the magnetic field is to place a conducting nanobeam in a uniform magnetic field perpendicular to the long axis of the oscillator; one then allows an ac cur-

rent to flow through it and detects the voltage drop between the two ends of the beam. Because of the current flow perpendicular to the magnetic field, the bridge experiences a uniformly distributed Lorentz force in a direction that is perpendicular to both the beam and the magnetic field and that, as a first approximation, does not depend on the displacement of the oscillator from its equilibrium position. This systems acts like a driven harmonic oscillator, and therefore the oscillation amplitude in the stationary regime depends only on the frequency of the driving ac current, according to the usual Lorentzian curve. The displacement produced in this way is perpendicular to the magnetic field and the area swept by the beam results in an electromotive force along the circuit in which the nanobeam is integrated. The voltage drop across the beam due to the magnetic induction varies in time with the same frequency as the ac current flowing through the beam; the amplitude of voltage oscillations, however, follows the Lorentzian curve describing the response to the driven oscillator. After amplification, this signal can be measured to determine the proper frequency of the mechanical bridge (that is, of all the modes that can be coupled to the magnetic field) and its characteristic damping rate.

Electric actuation and sensing is usually performed by allowing a conducting plate or lead (the gate) to face the nanobeam and then exploiting interactions between the charge carriers in the two conductors. As a first approximation, this system can be described as a capacitor whose capacitance depends on the distance between the nanobeam and the conducting plate. A voltage difference between the two conductors produces charge accumulation in the nanobeam and in the gate plate, of opposite sign; this in turns results in an electrostatic force between the suspended nanobeam and the fixed gate lead. By varying the voltage of the gate lead, one can vary the force acting on the nanomechanical oscillator and drive it. This same coupling scheme can be used for sensing by replacing the gate lead with an electrometer kept at fixed voltage difference with respect to the nanobeam: a displacement of the oscillating bridge produces a change in the capacitance to the electrometer and of the charge present in it.

The quantum nature of mesoscopic and nanoscopic conductors at cryogenic temperatures can be exploited to study the physics of nanoscale mechanical oscillators in a much deeper way along both the above mentioned schemes. On the one hand, coupling a mechanical oscillator to a quantum system is the only way to directly detect quantum fluctuations in the values of its observables [81]. On the other hand, the combination of quantization of the energy spectrum and gauge invariance makes low-temperature mesoscopic conductors optimal detectors of charge and magnetic flux.

One important example is the Single Electron Transistor, or SET[82].

The key concept behind this very important device is the *Coulomb Blockade*. Coulomb Blockade is the phenomenon taking place when the transport of a single electron through a small conducting island is suppressed by an overwhelming increase in the electrostatic potential energy that such a process would produce. It can be shown that the charging energy of a small conducting island can be written as $E_c(n - n_g)^2$, where E_c is called charging energy and is inversely proportional to the total capacitance of the island to the ground, n is the number of charge carriers present on the island and n_g is the number of charges induced on the island by some lead held at a finite voltage V_g. If n_g is half-integer, then changing the number of charge carriers from $n_g - 1/2$ to $n_g + 1/2$ does not change the energy; transport through the conducting island can take place one charge carrier at a time. If n_g is an integer, instead, no charge carrier can pass through the island unless an energy E_c is provided; if this energy is much larger than thermal energy fluctuations and than the energy gain for a charge carrier to go from one side of the island to the other, and if quantum fluctuations of n can also be neglected, then transport is suppressed. The conductivity of a device made by a small conducting island attached to two leads in the presence of a gate voltage is thus very sensitive to changes in the product $C_g V_g$. The improvement of electrometers due to the quantum behavior of mesoscopic conductors allowed scientists to achieve some of the most sensitive displacement detectors available [83, 84].

Quantum-coherent devices produced analogous improvements in the field of ultra-sensitive detection of magnetic flux. Applications of superconductivity technology to the field of displacement detection is the subject of the remainder of this thesis.

3.2 Superconducting NEMS

Many conducting materials undergo the superconducting phase transition at very low temperatures. In the superconducting state the spectrum of excitations of the system has a finite gap and because of this charge carriers can flow through a superconductor without being scattered (zero resistance, or current flow without voltage drop). Moreover the superconducting phase displays perfect diamagnetism, meaning that, in the presence of an external magnetic field, dissipationless currents flow around the superconductor shielding the magnetic field deep in the bulk. These two facts can be accounted for by assuming that the order parameter associated with the superconducting phase transition behaves like a quantum wave function under gauge transformations and that the dissipationless currents are proportional to the gradient of the complex phase of the order parameter itself. The super-

conducting order parameter can also be shown to obey a differential equation which is very similar to the Schrödinger equation. Therefore, in many respects, superconductors exhibit quantum behavior on a macroscopic scale. Small constrictions or insulating barriers between superconductors, although not superconducting by themselves, have been proven to admit supercurrent flows because charge carriers can tunnel through them; this is known as the *Josephson Effect* and the barriers are called *Josephson junctions*. A well-known example of macroscopic quantum behavior in superconductors is the so-called *Macroscopic Quantum Tunneling*[85], which consists of a sudden change in the gradient of the complex phase of the superconducting order parameter across a Josephson junction due only to quantum fluctuations; this can be detected because, while a gradient in the phase is just a supercurrent, a time-varying gradient in the phase produces a non-zero voltage drop. The quantum nature of the phenomenon is proven by the statistics of the "escape" events.

In view of these peculiar characteristics, coupling nanomechanical oscillators to superconducting circuits is very promising and has received much attention from researchers in both experimental and theoretical Quantum physics. A simple scheme for obtaining this kind of coupling is to merely exploit the standard electrostatic or magnetic induction between a conducting nanomechanical oscillator and a quantum superconducting circuit such as a Superconducting Single-Electron Transistor or a superconducting qubit.

However, in principle nothing prevents the nanobeam itself from being a superconductor, since the metal used for building the conducting layer might well be one of those that become superconductors at low temperatures. In this case the intrinsic quantum coherence of a superconducting circuit can be used to couple the mechanical degree of freedom with the dynamics of the current or the voltage drop by exploiting quantum interference effects. An interesting way of implementing this idea is by integrating a superconducting nanomechanical oscillator in the loop of a superconducting quantum interference device (see appendix D for a brief review of the working principles of SQUIDs); this would allow us in principle to exploit the high sensitivity of SQUIDs in detecting small flux changes to measure the position of the oscillator. A remarkable amount of attention in the last few years has been devoted to coupling SQUIDs to mechanical oscillators for detection or cooling [86, 87, 88, 89, 90] and, recently, the first detection of mechanical motion of a micromechanical resonator embedded in a dc SQUID was reported [91].

Motivated by the high sensitivity of SQUIDs as flux to voltage transducers and the possibility of realizing superconducting loops in the quantum regime, we study the coupled dynamics of a SQUID and a nanomechanical oscillator, both in the classical and quantum regime. The basic idea is to have one arm of

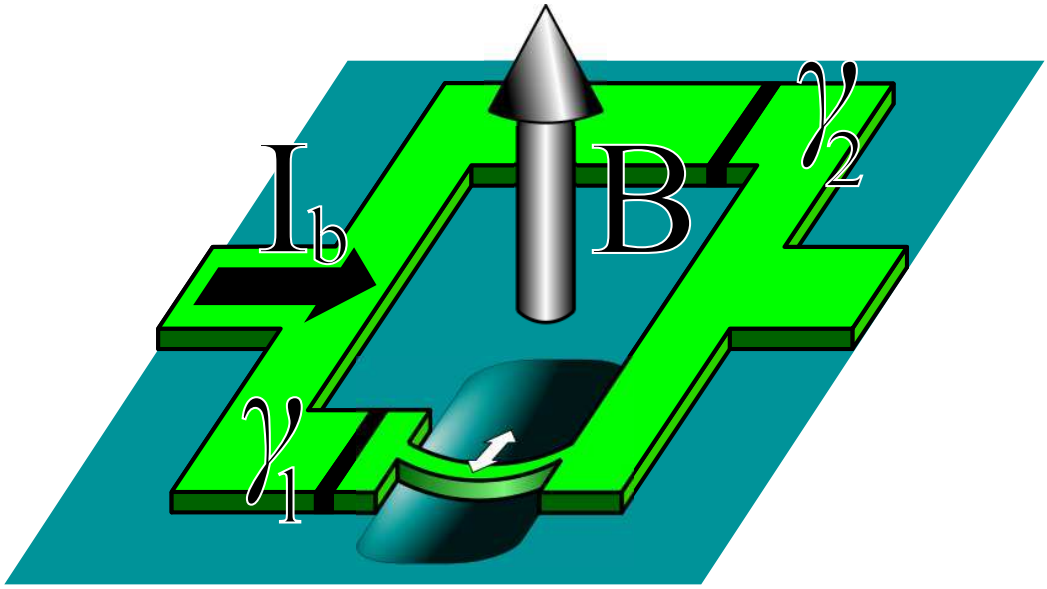

Figure 3.1: A pictorial view of a dc SQUID with a suspended arm that is free to oscillate in the plane of the SQUID itself. A uniform constant magnetic field B is present, and it represents the means of coupling the mechanical motion of the suspended arm with the electronic degrees of freedom of the SQUID, here just the two superconducting phase drops γ_1 and γ_2. In principle a dc bias current I_c is allowed to flow through the device.

the loop free to oscillate, either in the plane of the loop itself or perpendicular to it. The mechanical motion is reflected in a change in the shape of the loop and hence of its area; in the presence of a constant uniform magnetic field B, this provides a mechanism for coupling the mechanical degree of freedom of the oscillating arm with the magnetic flux threading the loop, which is an electrical degree of freedom of the superconducting circuit. A generic sketch of the device is depicted in Fig. 3.1. Depending on the design of the suspended arm, the fundamental mode can be flexural, longitudinal or even breathing (in the case of carbon-nanotube oscillators). In the following we will assume that the fundamental mode is flexural and that the area swept by the motion of the oscillator in this mode is $l \cdot X$, where X is the displacement of the center of mass from its rest position and l is an effective length, which is of the order of the length of the suspended bridge[1]. Since the coupling between the mechanical degree of freedom and other coordinates of the superconducting circuit is via the induced magnetic flux, the strength of

[1]This relation is not general, it is just the first order term of a Taylor expansion of the swept area as a function of X.

this coupling is proportional to the change in the magnetic flux induced by the zero point motion of the oscillator. In superconducting circuits there is a typical scale for the magnetic flux affecting the dynamics, namely the *flux quantum* $\Phi_0 = h/2e \simeq 2.07 \times 10^{-15}$Wb, therefore the strength of the coupling between the mechanical and electrical degrees of freedom is measured by the dimensionless ratio:

$$\frac{BlX_0}{\Phi_0} \tag{3.3}$$

where X_0 is the amplitude of the zero-point motion. For estimating the order of magnitude of this ratio, we take as an example a carbon nanotube 1μm long, whose mass is approximately 10^{-17}kg, with a fundamental flexural frequency $\nu \simeq 1$GHz in a magnetic field of 1T and we get the value 10^{-5}.

Chapter 4

Classical dynamics of a nonlinear SQUID-NEMS

In this chapter we analyze the coupled dynamics of a SQUID with a moving arm acting like a nanoelectromechanical device. In principle the nonlinearity introduced by the Josephson junctions can result in effects that, like rectification, can be useful for the purpose of monitoring the oscillator's position and/or momentum, or at least to gain information about its mechanical properties. The starting idea of our study was to exploit the so-called ratchet effect[92].

In very simple terms the ratchet effect can be explained by considering a particle moving in an external periodic potential and subject to a periodic (or random) force with zero average. If the potential breaks spatial inversion symmetry, a directed motion is possible even if the system is unbiased. By detecting the directed motion of a particle it is in general possible to gain information on the oscillating force.

It has been shown [93] that SQUIDs can behave as ratchets, where the superconducting phase difference at the junction γ and the Josephson potential play the role of the coordinate and the ratchet potential, respectively. When such systems are biased by an ac current, a constant drift in the phase drop occurs under appropriate conditions, causing a finite dc voltage.

In the following we will show how to exploit the rectifying properties of these SQUID ratchets in order to characterize the motion of a nanomechanical resonator; indeed a mechanical oscillator embedded in a SQUID circuit threaded by a magnetic flux produces an ac signal across the SQUID that plays the role of a zero-average driving force, and, although this signal is too small to be rectified, it nevertheless affects the dc characteristic of this ratchet circuit. We find that the current-voltage curve is qualitatively changed by the mechanical oscillations with respect to the case without a moving part.

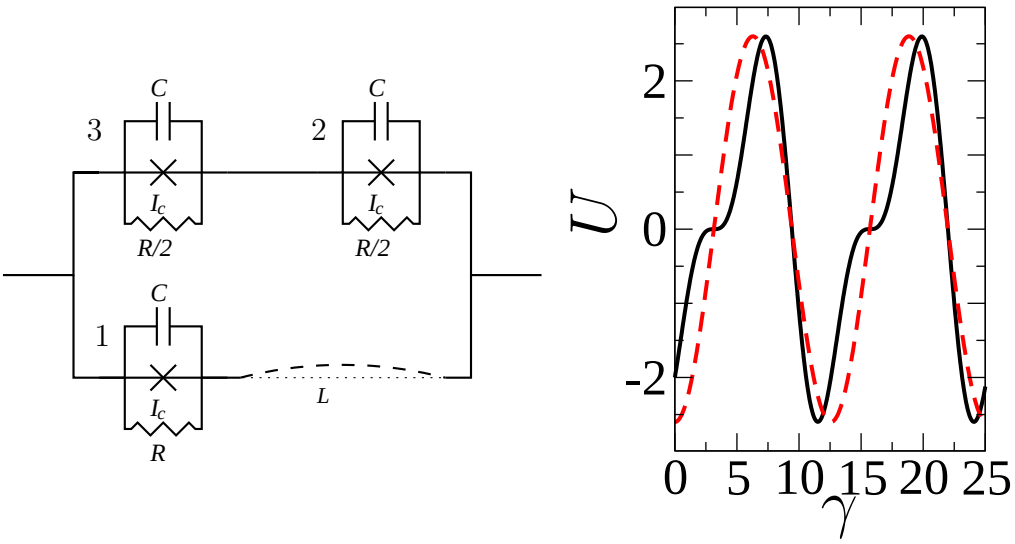

Figure 4.1: *Left panel.* A scheme of the ratchet circuit considered here. Three Josephson junctions are coupled to a mechanical resonator oscillating in the plane of the circuit, threaded by a magnetic flux, and biased by a current. The junctions have equal critical currents and capacitances but different shunting resistances. *Right panel.* The potential $U(\gamma)$ in the absence of a moving part (solid line); the average slope in the decreasing part is larger in modulus than the average slope of the increasing part, as can be seen by comparing with a cosine curve (dashed line).

4.1 The Model

The circuit that we analyze is schematically depicted in Fig. 4.1. It consists of a Josephson junction and a mechanical resonator connected in parallel with two other Josephson junctions. The Josephson junctions are in the classical regime and they can be described with the RCSJ model, i.e.

$$\frac{I_i}{I_c} = \sin\gamma_i + \frac{\hbar}{2eR_iI_c}\dot{\gamma}_i + \frac{\hbar C}{2eI_c}\ddot{\gamma}_i \qquad i = 1, 2, 3\ . \tag{4.1}$$

In Eq.(4.1) the current flowing through each junction is denoted by I_i, and γ_i is the related gauge-invariant phase difference. In Eq. (4.1) C denotes the capacitance, and R_i the resistances, chosen as $R_1 = R$ and $R_2 = R_3 = R/2$ (see Fig. 4.1). For simplicity we assumed that the three junctions are characterized by the same critical current I_c. By considering overdamped junctions, $\omega_{pl}RC \ll 1$ ($\omega_{pl} = \sqrt{2eI_c/\hbar C}$ is their plasma frequency), the terms involving second-order derivatives of the phases can be neglected in Eq. (4.1). One can then show that, if $\gamma_2 = \gamma_3$ holds at a certain time, such

a condition is maintained. We shall henceforth set $\gamma_2 = \gamma_3 = \gamma/2$, whereas the phase γ_1 is related to the others by the equation

$$\gamma_1 - \gamma = 2\pi \left(\frac{\Phi}{\Phi_0} + n \right) \qquad n = 0, 1, \ldots \tag{4.2}$$

ensuring a vanishing total phase difference along the loop. In the Eq. (4.2) Φ denotes the total magnetic flux threading the circuit and Φ_0 is the elementary quantum of flux. Neglecting the self-inductance of the loop, the flux is determined by the total area of the circuit, which in turn depends on the position of the resonator: $\Phi = B(A + lX(t))$ (l is the effective length of the resonator, $X(t)$ is the position of its center of mass and A is the area of circuit when $X(t) = 0$). In the remainder of this chapter we will assume that the motion of the resonator is fixed externally and equals $X(t) = X_0 \cos(\omega t)$ (see Sec. 4.5). Indicating by I_b the current biasing the device, current conservation $I_b(t) = I_1(t) + I_2(t)$ leads to the following equation of motion for the phase γ,

$$\partial_\tau \gamma = -\frac{\partial U}{\partial \gamma} + \frac{I_b(\tau)}{I_c} + \frac{\pi L B X_0}{\Phi_0} \Omega \sin(\Omega\tau) \ , \tag{4.3}$$

where $\tau = \omega^* t$ is a dimensionless time variable, $\omega^* = eRI_c/\hbar$ and $\Omega = \omega/\omega^*$. We will consider external bias of the form $I_b(\tau) = I_{dc} + I_{ac} \cos(\Omega_{ac}\tau)$, with I_{dc} denoting the dc component, and I_{ac} and Ω_{ac} the amplitude and frequency of a monochromatic ac component. The periodic function

$$U(\gamma, f(\tau)) = -2\cos(\gamma/2) - \cos(\gamma + \phi + f(\tau)) \tag{4.4}$$

is the potential leading to the ratchet effect as discussed by Zapata *et al* [93]. In addition to the dimensionless external magnetic flux $\phi = 2\pi AB/\Phi_0$, the potential U now also includes a time-dependent fluctuation part $f(\tau) = (2\pi LBX_0/\Phi_0)\cos(\Omega\tau)$ which arises from the oscillations of the mechanical resonator. The coupling between the SQUID and the mechanical resonator can be parametrized by the dimensionless parameter

$$a = \frac{2\pi L B X_0}{\Phi_0} \tag{4.5}$$

At finite temperatures the r.h.s. of Eq.(4.3) will also include a noise term, as discussed in section 4.4.

Depending on the value of the external flux, the potential term defined in Eq.(4.4) breaks γ inversion symmetry and therefore leads to the ratchet effect. In Ref. [93] this effect has been shown by biasing the SQUID with an oscillating current leading to a finite dc voltage. Here we show that the

ratchet effect allows one to detect the oscillatory motion of the oscillator which enters the dynamics of the systems both in the potential through the fluctuating part of the flux and in the third term on the r.h.s of Eq.(4.3). We emphasize that in order for the ratchet effect to appear, the system needs to be out of thermal equilibrium[92].

The dc voltage drop across the circuit can be expressed through the Josephson relation as

$$V_0 = \frac{\hbar}{2e}\left\langle \frac{d\gamma}{dt} \right\rangle = \frac{RI_c}{2}\langle \partial_\tau \gamma \rangle \quad , \tag{4.6}$$

where the brackets $\langle \ldots \rangle$ indicate time average (and possibly thermal average). A non-vanishing voltage drop can be obtained when the ratchet potential is asymmetric in γ, which occurs for values of the magnetic flux $\phi \neq n\pi$. In particular one finds that, for sufficiently large values of I_{ac}, a finite dc voltage $V_0 \neq 0$ arises even in the presence of a vanishing average drive ($I_{dc} = 0$). Furthermore, for $I_{dc} \neq 0$ the dc $V - I$ curve is not an odd function of the current. It is therefore convenient to analyze its symmetric (even) part defined as

$$v_0^e \doteq \frac{V_0(I_{dc}) + V_0(-I_{dc})}{2RI_c} \, . \tag{4.7}$$

Mechanical oscillations lead to two effects in the dynamics of the SQUID. First, a term qualitatively similar to an ac bias arises, as shown by the last term in the r.h.s of Eq.(4.3). Second, a fluctuating term $f(\tau) \neq 0$ appears in the potential, affecting the symmetry of the ratchet potential as a function of γ. In the presence of the resonator the analysis is thus more subtle. As we shall see in Sec. 4.2, the fluctuations of the potential tend to wash out the ratchet effect, although for some specific values of the parameters one can still obtain $V_0(I_{dc} = 0) \neq 0$. In most cases the ratchet effect survives only in some non-trivial features in the symmetric part of the $V - I$ curve, which will be a main focus in the rest of the paper.

Apart from some specific cases the equation of motion of the SQUID, (4.3), does not allow for an analytic solution. Most of our results are based on a numerical integration of the equation of motion. As we are interested in the feasibility of a SQUID-based detector of the mechanical oscillations, it is appropriate to first briefly discuss the case where no oscillator is present, in order to highlight the difference due to the mechanical motion. When the SQUID is biased by a dc current $[I_b(\tau) = I_{dc}]$ and there is no resonator ($a = 0$) the voltage drop can straightforwardly be computed as $V_0 = 4\pi(RI_c/2)/T$,

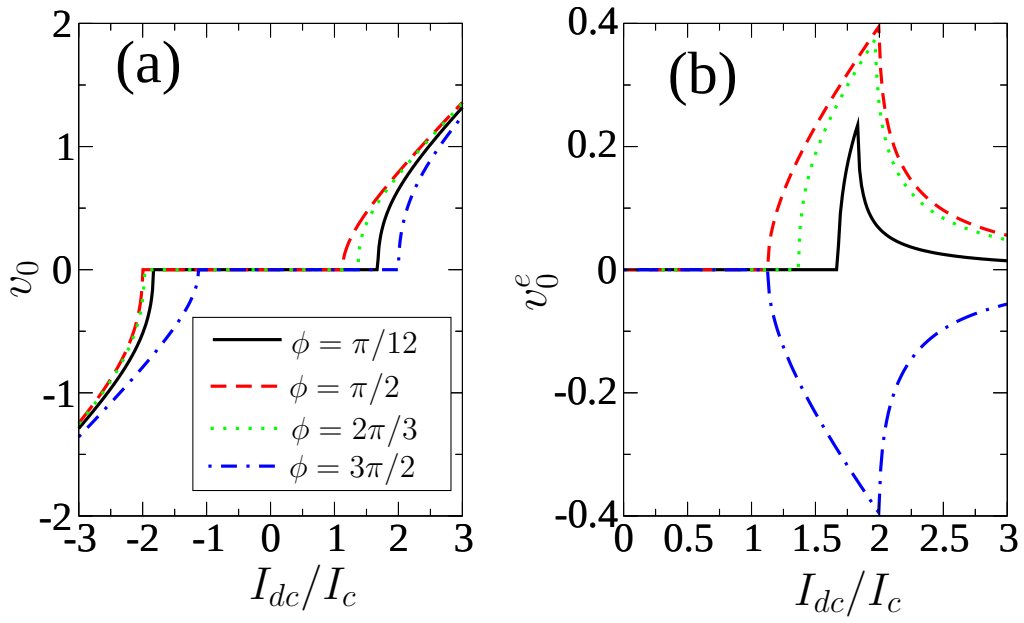

Figure 4.2: (a) Dimensionless dc voltage drop $v_0 = V_0/RI_c$ as a function of the dimensionless bias current I_{dc}/I_c, for different values of the flux. No oscillating mechanical part is present ($a = 0$). (b) The even part v_0^e of the same curves plotted for positive values of I_{dc} only. v_0^e is zero for $\phi = n\pi$ and $v_0^e(-\phi) = -v_0^e(\phi)$.

where 4π is the period of the potential (4.4), and

$$T = \int_0^{4\pi} \frac{d\gamma}{I_{dc}/I_c - \sin(\gamma/2) - \sin(\gamma + \phi)} \tag{4.8}$$

is the time required for the phase to span such an angle. The resulting $V - I$ curve of the device is shown in Fig. 4.2(a). For an asymmetric potential ($\phi \neq n\pi$) the curves are not odd in the current, and a non-vanishing even component (4.7) arises [see Fig. 4.2(b)]. This component will be shown to be affected by the presence of the mechanical resonator. As the flux varies, the curve $v_0(I_{dc})$ shifts to the left and then to the right with a period of 2π; this is reflected in the amplitude and sign of v_0^e. Indeed, from Eq. (4.8) one can show that $v_0^e(-\phi) = -v_0^e(\phi)$ and $v_0^e(\phi = 0) = 0$.

4.2 Slowly oscillating resonator – the adiabatic limit

We now discuss the role of the resonator. Before addressing the full numerical solution of Eq. (4.3), we discuss here the limiting situation in which $\Omega \ll 1$, i.e. the oscillator's frequency is much smaller than the plasma frequency of the SQUID. As we shall see, this regime is indeed suggested by the typical experimental conditions, where $\Omega \sim 10^{-3}$, indicating that the mechanical oscillations are much slower than the dynamics of the junctions. Moreover the same condition can be realized for the frequency of the ac component of the bias current. Under these conditions, the equation of motion can be solved within the adiabatic approximation. One can determine $v_0(I_{dc})$ by evaluating, for a fixed position of the oscillator $X(\tau)$ and value of the bias current $I_b(\tau)$, the time $T(\tau)$ required for the phase to span an angle 4π. Averaging over τ one then obtains

$$\begin{aligned} v_0 &= \frac{1}{2}\langle 4\pi/T(\tau)\rangle = \\ &= \int_0^{2\pi}\left[\int_0^{4\pi}\frac{d\gamma}{I_b(\theta)/I_c - \partial_\gamma U(\gamma, f(\theta)) + \frac{a\Omega}{2}\sin(\theta)}\right]^{-1} d\theta \end{aligned} \tag{4.9}$$

Equation (4.9) will be analyzed in two different cases in which the bias current is constant or has also an additional monochromatic ac component.

Dc bias current. We start by analyzing the situation of a dc bias current, $I_b(\tau) = I_{dc}$. In Fig. 4.3(a) and 4.3(b) the even component (4.7) of the voltage is plotted as a function of I_{dc}, for different values of the coupling strength a and flux ϕ. For small coupling $a \ll 1$, we recover the exact results discussed in Sec.4.1 [see Fig. 4.2(b)]. On the other side, at high values of the coupling the main effect of the mechanical oscillations is to wash out the effects of the asymmetry of the ratchet potential. This is due to the fact that in this system the resonator oscillations also affect the ratchet potential via the term $f(t)$. Notice that the disappearance of asymmetry occurs at lower values of a for a smaller flux ϕ, as one can see by comparing the dashed-dotted curves in Fig. 4.3(a) and 4.3(b). Thus the effects of the coupling to the mechanical resonator are more dramatic for $\phi \sim n\pi$. Note, however, that for the special values $\phi = n\pi$, where n is an integer, one still finds $v_0^e = 0$, as can be shown by a change of integration variables $\gamma \to -\gamma$ and $\theta \to \pi + \theta$ in Eq. (4.9) with $I_b(\tau) \equiv I_{dc}$. We notice also that the experimentally accessible values of a are very small. Although in section 4.5 possible operative ways to enhance

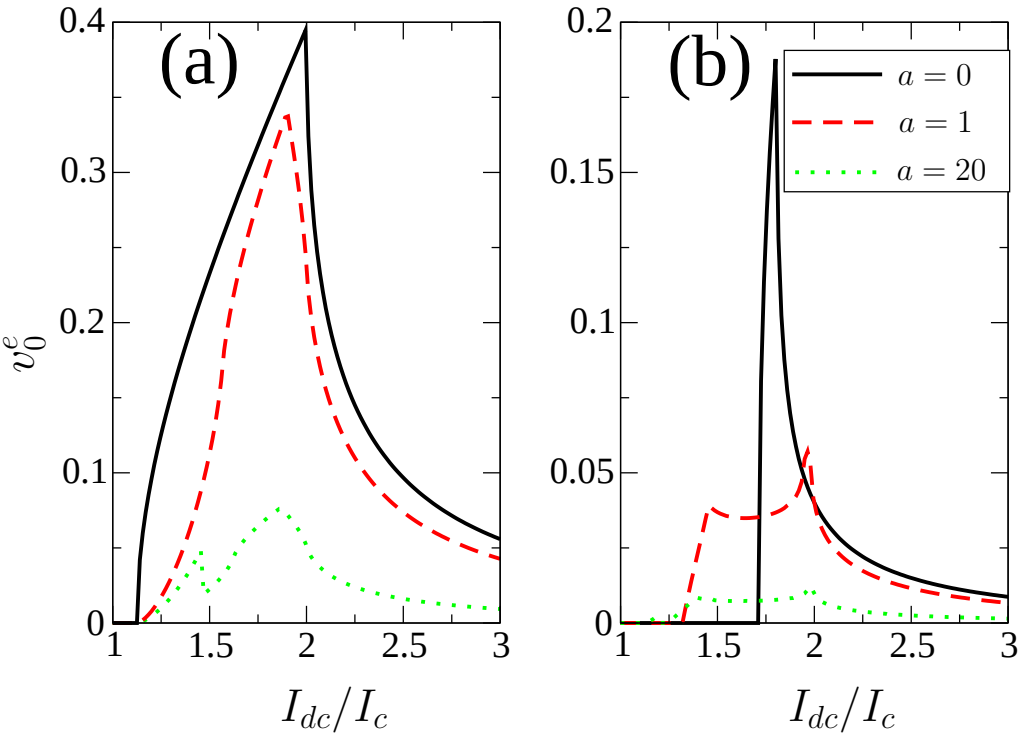

Figure 4.3: $v_0^e(I_{dc})$ curves for different values of the coupling parameter a. The two plots refer to different values of the flux: (a) $\phi = \pi/2$ and (b) $\phi = \pi/20$. While for small coupling one recovers the curves of Fig. (4.2), for high coupling the features are washed out. The effect is more pronounced for small flux bias.

the coupling a will be proposed, these results lead to the conclusion that, in the presence of a purely dc bias I_{dc}, it is difficult to gain information on a realistic mechanical resonator. A possible solution is to inject current with a monochromatic ac component with frequency $\omega_{ac}/2\pi$, small enough for the adiabatic approximation still to hold.

Ac monochromatic bias. In this case some new effects arise that can be clearly attributed to the mechanical resonator. One might naively expect that such effects simply originate from resonances at specific values of ω_{ac} related to ω, yielding an enhancement of the effects due to the mechanical oscillations. However, as we shall discuss below, the situation is more complex and the overall features of the current-voltage characteristics originate from different mechanisms.

We assume $I_b(\tau) = I_{dc} + I_{ac}\cos(\Omega_{ac}\tau)$ ($\Omega_{ac} = \omega_{ac}/\omega^*$) and we restrict to the case $\Omega_{ac} = \Omega q/p$, with q and p integers with no common divisor apart

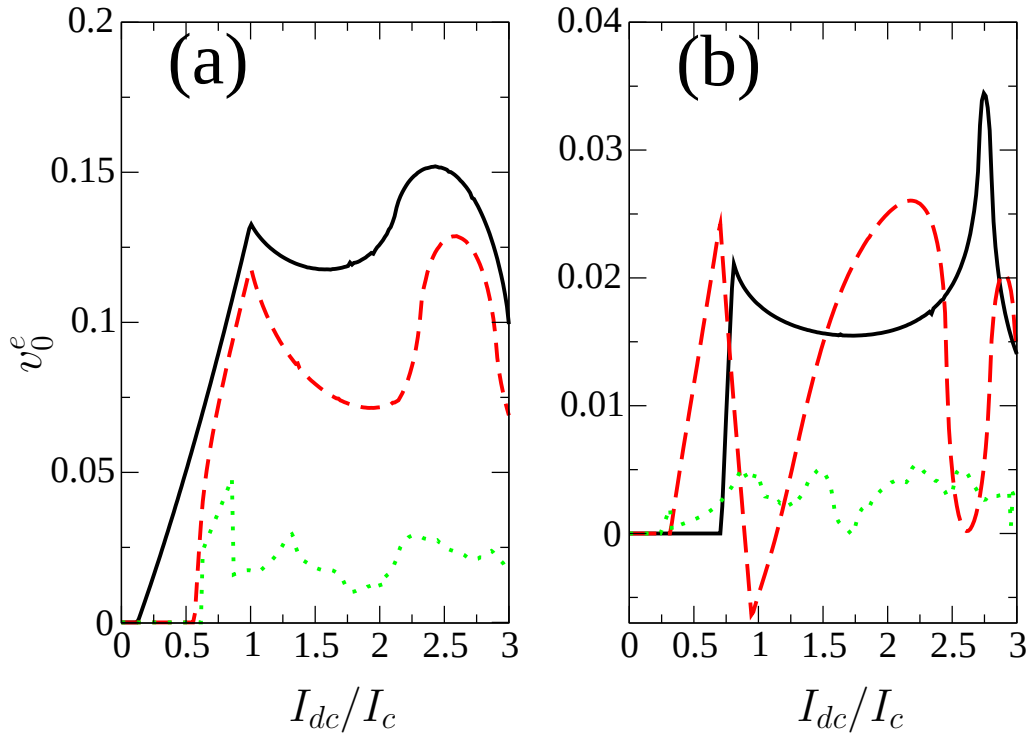

Figure 4.4: $v_0^e(I_{dc})$ curves for $I_{ac} = I_c$, $\Omega_{ac} = 2\Omega/3$ and different values of the coupling parameter a (the same as in Fig. 4.3). The two plots refer to different values of the flux bias: (a) $\phi = \pi/2$ and (b) $\phi = \pi/20$. Again, for small coupling the curves are indistinguishable from the uncoupled ones ($a = 0$); however for high couplings a richer structure now appears and its onset occurs at a smaller coupling for $\phi \sim n\pi$.

from 1. A straightforward calculation allows us to rewrite Eq. (4.9) as

$$v_0 = \int_0^{2\pi} d\theta \left\{ \int_0^{4\pi} d\gamma \left[\frac{I_{dc}}{I_c} + \frac{I_{ac}}{I_c}\cos(q\theta) - \sin\left(\frac{\gamma}{2}\right) - \right.\right. \\ \left.\left. - \sin[\gamma + \phi + a\cos(p\theta)] + \frac{a\Omega}{2}\sin(p\theta) \right]^{-1} \right\}^{-1} \tag{4.10}$$

and to determine how the ac bias affects the $V - I$ curves of Fig. 4.3. The result is shown in Fig. 4.4 for two different values of the flux.

The even component v_0^e is suppressed for strong coupling, similar to the dc bias case. However, a richer structure due to the interplay of the two components of the driving bias is observable. Another noteworthy difference with respect to the dc case is that at small values of the dimensionless flux, the suppression occurs at higher values of the parameter a, as one can observe

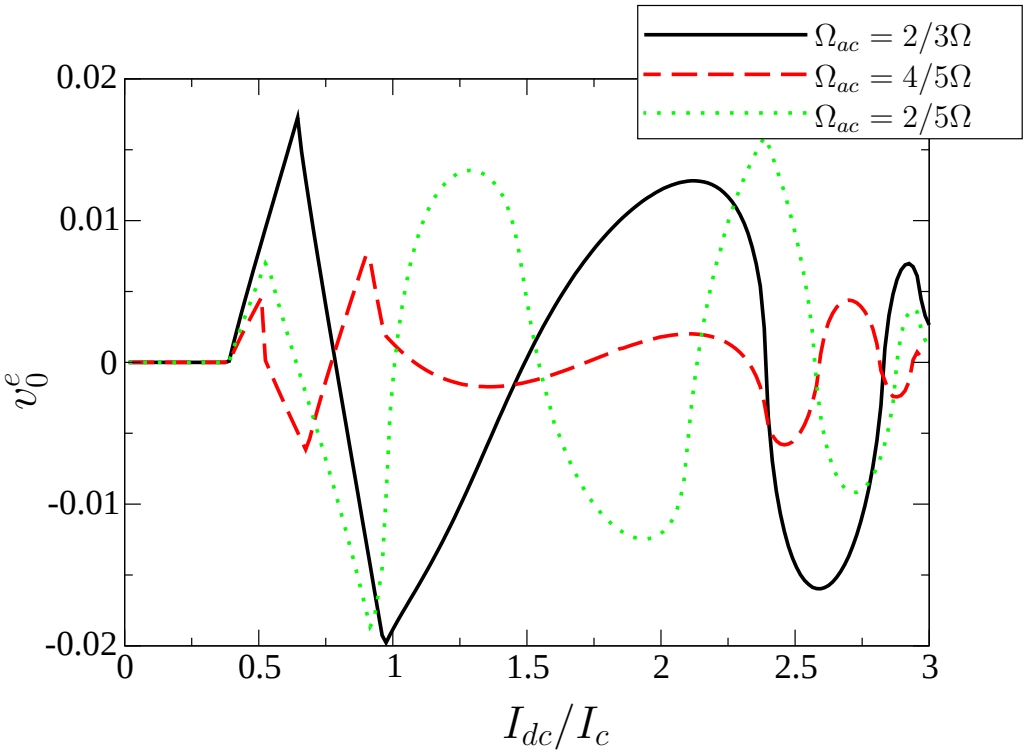

Figure 4.5: $v_0^e(I_{dc})$ for zero bias flux and different values of the ratio Ω_{ac}/Ω. Here $a = 1$, while for $a = 0$ the curves should be flat ($v_0^e \equiv 0$).

by comparing the curves of Fig. 4.4(b) with Fig. 4.3(b). This indicates that the presence of an ac current makes the even component of the characteristic curve much more robust to the coupling with the resonator. Such difference is particularly striking at $\phi = n\pi$ ($n = 0, \pm 1, \ldots$). For these particular values of flux v_0^e vanishes for a purely dc bias current, whereas a finite value of v_0^e is predicted for an ac current. Indeed the argument used to prove that $v_0^e \equiv 0$ if $\phi = n\pi$ (a suitable change in the integration variables) does not apply when $I_{ac} \neq 0$, unless the frequency assumes specific values, namely those for which p and q are both odd integers. One can see the effects of the two combined oscillations in Fig. 4.5. Notice that these curves cannot be due to an ac bias *alone*, for if $a = 0$ and $I_{ac} \neq 0$ the same argument of the previous section would apply, and the $V - I$ curve at $\phi = n\pi$ would be odd.

These results suggest a possible operative detection protocol for the tiny motion of a mechanical resonator integrated in a SQUID ratchet circuit: one may first measure the $V - I$ curve of the circuit biased by a purely dc current, for different values of magnetic flux ϕ. This would allow the determination of values of ϕ such that the $V - I$ curve is completely odd. Then, by adding

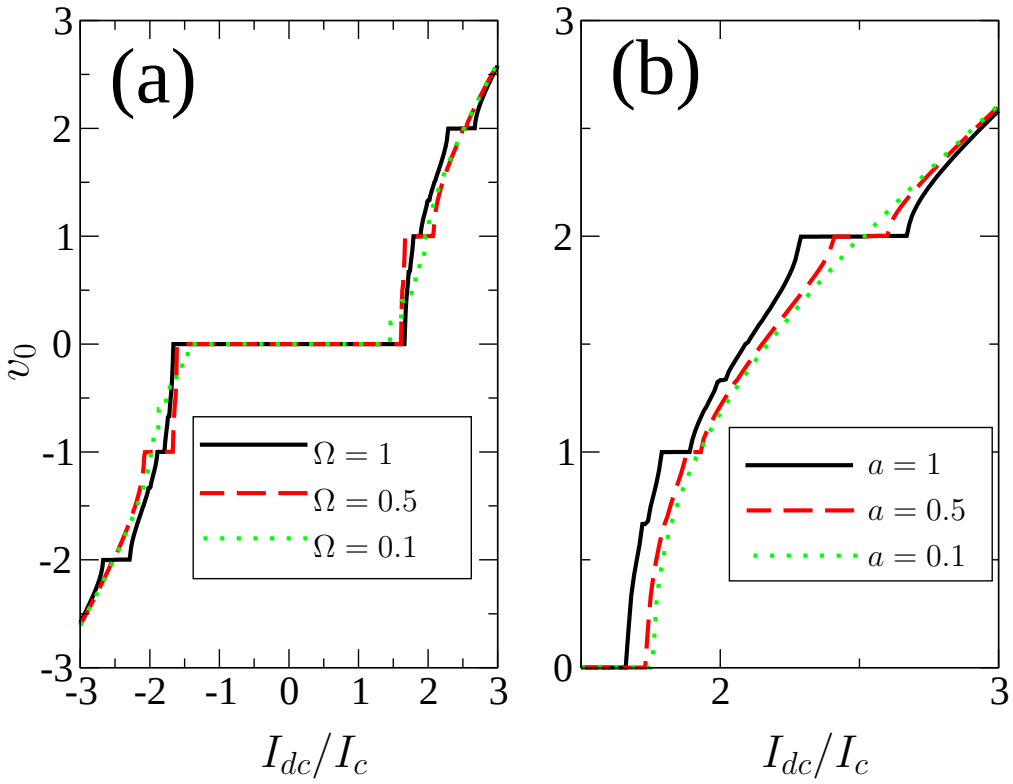

Figure 4.6: (a) Exact v_0-I_{dc} curves for different frequencies Ω of the mechanical resonator. Here $a = 1$, $I_{ac} = 0$ and $\phi = 0$. Even though no ac bias current is supplied, the system exhibits Shapiro steps, whose heights are related to Ω. (b) The same but for a fixed frequency $\Omega = 1$ and different values of the coupling a. The width of Shapiro steps approaches zero for small values of a.

an ac term to the bias current, without changing the magnetic field, a non-vanishing even component would arise in the $V - I$ curve while varying the frequency of the ac bias.

4.3 Arbitrary resonator frequency

In many situations the value of the coupling parameter a is rather small (see Sec. 4.5); for improving the coupling efficiency one could then in principle study devices with a higher value of the frequency Ω, so that the coupling term $a\Omega\cos(\Omega\tau)/2$ can be increased. Under these circumstances the adiabatic approximation may no longer hold and one should compute the current-voltage characteristic starting from the complete numerical solution

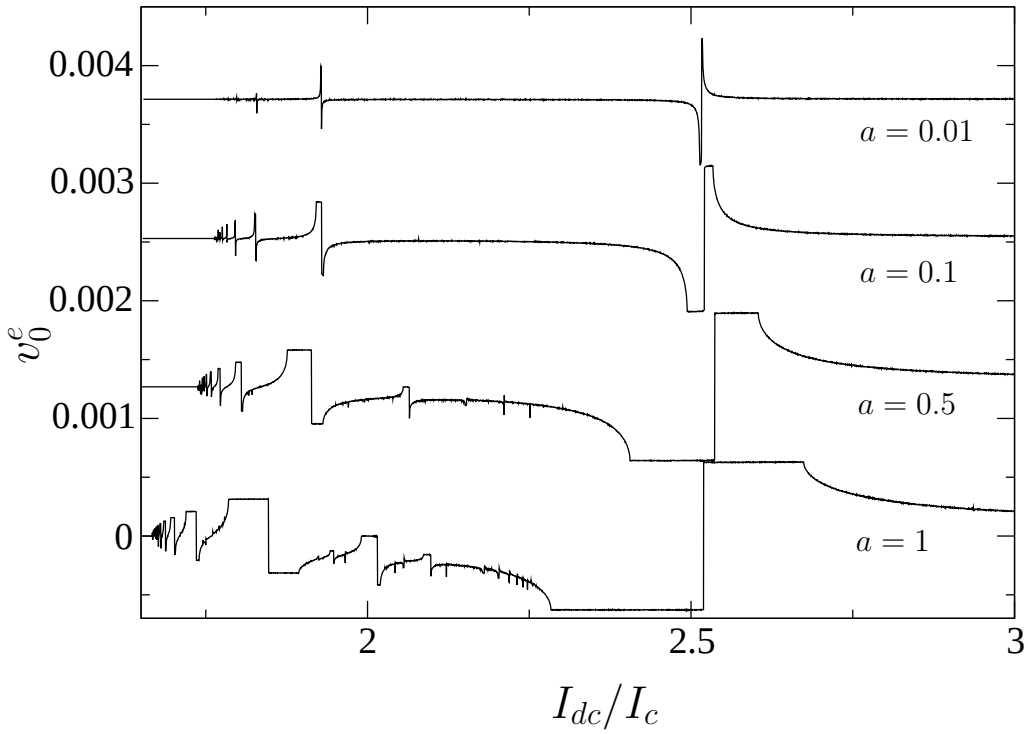

Figure 4.7: The even component v_0^e of the voltage drop as a function of the dc bias current I_{dc} at $\phi = 0$ and $\Omega = 1$ for different values of the coupling a (the curves are displaced vertically). The amplitude of the features is the same for all couplings, but their widths become smaller for smaller couplings.

of Eq. (4.3).

The results are shown in Fig. 4.6(a), where the $V - I$ curves at strong coupling are plotted, in the absence of the ac bias current, at vanishing flux and for different values of the dimensionless frequency Ω. One can clearly recognize the typical shape of the $V - I$ curve for ac biased Josephson junctions, characterized by Shapiro steps. However, while these features are usually attributed to an ac bias current, here they originate from the mechanical oscillations. Notice that the height of the steps varies with the proper frequency of the resonator, as happens for Shapiro steps in isolated Josephson junctions. This suggests that in principle the frequency of the resonator can be directly read by inspection of the height of the steps in the $V - I$ curve of the system. Instead, the width of the steps is usually related to the amplitude a of the ac biasing signal. This is illustrated in Fig. 4.6(b), where one can see that as a approaches zero, the steps become narrower and the $V - I$ curve becomes smoother.

Important differences emerge with respect to the adiabatic limit. In par-

ticular the even component of the $V - I$ curve does not vanish for $\phi = n\pi$ and $I_{ac} = 0$, and exhibits an interesting structure: ranges where the voltage is independent of I_{dc} are separated by sequences of maxima and minima, as shown in Fig. 4.7. Interestingly, the amplitude characterizing these features in the even component of the $V - I$ curve seems roughly independent of the coupling parameter a. This represents a promising effect for the detection of realistic mechanical oscillators. However, as is already the case for the whole curve $v_0(I_{dc})$ (Fig. 4.6), the width of the different peaks is suppressed for small coupling.

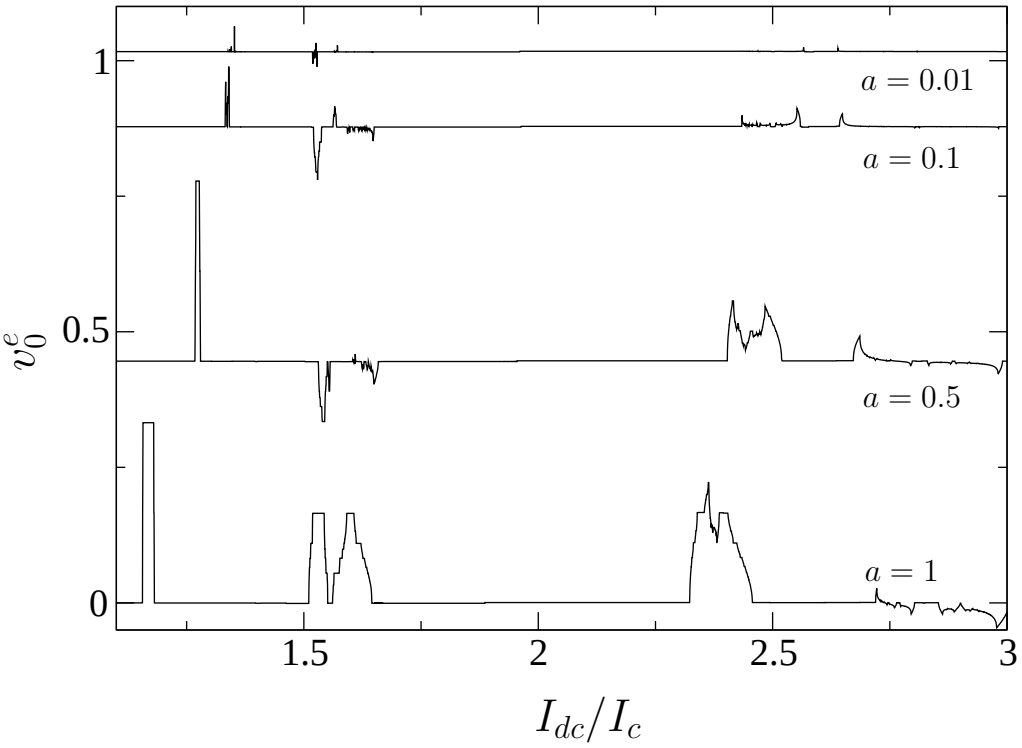

Figure 4.8: The even component v_0^e of the voltage drop as a function of the dc bias current I_{dc} at $\phi = 0$ and $I_{ac} = I_c$, for different values of the coupling a. Here $\Omega = 1$ and $\Omega_{ac} = 0.67$.

The effect of an ac bias is to enhance the amplitude of these features; indeed the ratio between the heights of the features in Fig. 4.8 and those in Fig. 4.7 is about 50. The numerical solution indicates that, in the absence of a mechanical oscillator ($a = 0$), the $V - I$ curve is odd ($v_0^e \equiv 0$), as in the adiabatic limit. We conclude that at $\phi = n\pi$ a detected signal has to be attributed only to the mechanical resonator. Even though the main difficulty at low coupling still remains, these effects may be enhanced by applying an

ac bias.

4.4 Finite Temperatures

In this section we discuss the effects of thermal fluctuations on the dc voltage drop of the system. To be consistent with the model adopted so far, we shall focus on the classical regime and account for finite temperature by adding a stochastic term (white noise) in Eq. (4.3). These fluctuations are associated with two sources of dissipation: the finite resistance $R/2$ of the circuit, giving rise to electrical fluctuations in the bias current, and the finite quality factor Q of the mechanical resonator, related to a random force producing mechanical fluctuations. Electrical fluctuations are taken into account by adding a term

$$\Delta I_b(\tau) = I_c\sqrt{\frac{4ek_BT}{\hbar I_c}}\xi(\tau) \tag{4.11}$$

to the bias current $I_b(\tau)$, where $\xi(\tau)$ is a white-noise process with zero average and correlation function $\langle\xi(\tau)\xi(\tau')\rangle = \delta(\tau-\tau')$. Mechanical fluctuations may be introduced via a stochastic force

$$F(t) = \sqrt{\frac{2m\omega k_BT}{Q}}\eta(t) \tag{4.12}$$

acting on the resonator. Here m is the mass of the mechanical oscillator and $\eta(t)$ another white-noise process, statistically independent of ξ. In the previous sections we assumed the motion of the mechanical oscillator to be undamped ($Q = \infty$), so that the mechanical noise should be neglected. However for realistic devices this treatment is still a good approximation if

$$k_BT \ll Q\frac{1}{2}m\omega^2x_0^2 \tag{4.13}$$

with x_0 denoting the amplitude of the oscillation. For high Q there is a regime in which temperature is low enough to fulfill condition (4.13), but high enough to fulfill $k_BT \gg \hbar\omega$, so that the behavior is neither quantum nor noisy. In the following we shall assume that the mechanical noise can be neglected, and analyze Eq. (4.3) with

$$y = a\Omega/2\sin(\Omega\tau) + \frac{I_{dc}}{I_c} + \frac{I_{ac}}{I_c}\cos(\Omega_{ac}\tau) + \sqrt{\Theta}\xi(\tau) \tag{4.14}$$

where $\Theta = T/T_0$ and $T_0 = \hbar I_c/4ek_B \simeq 12\mathrm{K}\cdot I_c/1\mu\mathrm{A}$. As one may expect, for a certain value of the coupling parameter a there is a value of Θ above which

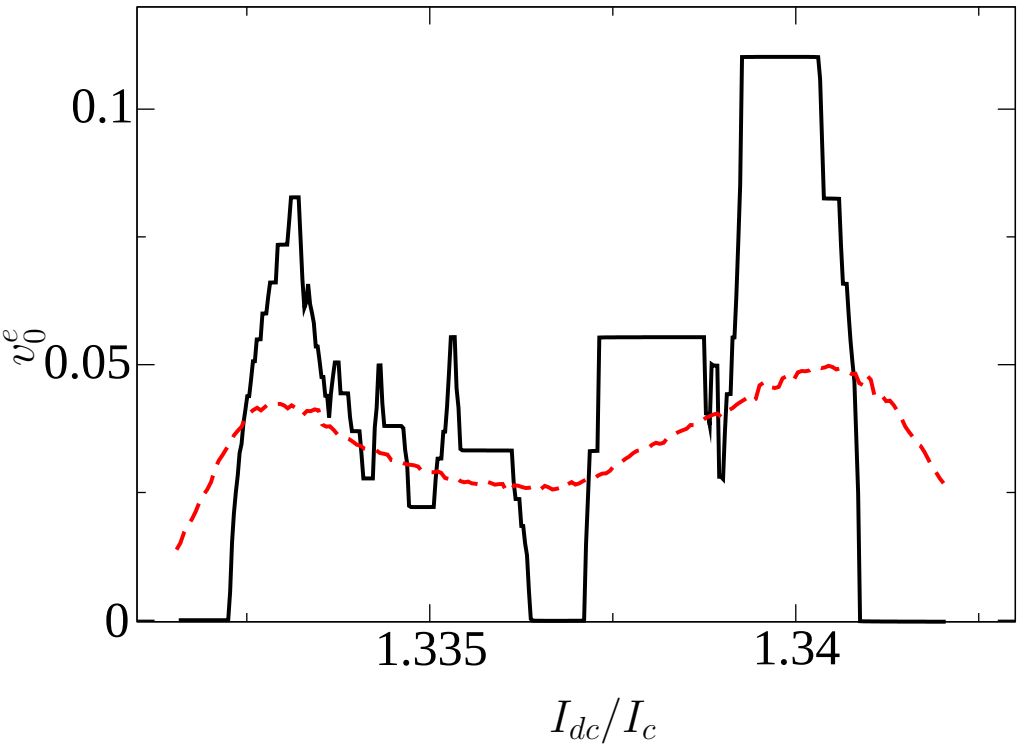

Figure 4.9: Some details of Fig. 4.8 for $a = 0.1$, $I_{ac} = 1$, $\Omega = 1$ and $\Omega_{ac} = 0.67$; the curves correspond to different temperatures: $\sqrt{\Theta} = 0$ (solid line) and $\sqrt{\Theta} = 10^{-4}$ (dashed line).

the peculiar features of the characteristic curve are lost. For determining the temperature scale at which this happens, one has to know T_0, which is set by the value of the critical current. Devices with large critical currents are in principle the best for this detection scheme, since they will be less affected by temperature. For a critical current as large as 1mA, the temperature scale is 10^4K. As an example, consider Fig. 4.9, which is a detail of the $v_0^e(I_{dc})$ curve in Fig. 4.7 for $a = 0.1$, compared with its finite temperature counterpart. Thermal fluctuations tend to wash out the peculiar features of the dc characteristic; the temperature scale at which this happens is 0.1mK for a high-I_c device, corresponding to $\Theta \approx 10^{-8}$.

4.5 Experimental perspectives

By now top-down fabrication techniques can produce single-crystal doubly-clamped beams whose typical dimensions are $1\mu\text{m}\times0.1\mu\text{m}\times0.1\mu\text{m}$ and whose frequency ranges from tens of MHz[80] to 1 GHz[94]; using Silicon Nitride or

Carbide, the density is about $3 \times 10^3 \mathrm{kg/m}^3$ and hence typical masses are of the order of 10^{-17}kg. Lower values can be obtained using carbon nanotubes, which can also have higher oscillation frequencies due to their high bulk modulus[95]. The oscillation can be induced by driving the resonator either mechanically (with a piezo element applied on the substrate and driven by an ac signal) or electrically (for instance by capacitively coupling the resonator with a gate electrode); a 1μm-long beam can be easily excited up to oscillation amplitudes of 1nm. To estimate the corresponding coupling parameter a one has to keep in mind that the magnetic field causing the coupling cannot be too large, otherwise the device loses superconductivity; a typical upper bound is $B < 0.1$T. With these values, one gets $a \approx 0.1$, the value used for the plots in Fig. 4.9.

The intensity of the back-action on the beam can be estimated by the Lorentz force acting on it in virtue of the current flowing through it: $F_l = LIB \simeq 1\mu\mathrm{m} \times 1mA \times 0.1T = 10^{-10}N$; this is to be compared with $m\omega^2 x_0 \simeq 10^{-17}\mathrm{kg} \times 4\pi^2(1\mathrm{GHz})^2 \times 10^{-9}\mathrm{m} = 4 \times 10^{-7}N$. (At such amplitudes the force may no longer be linear in the displacement and it would probably be larger than this estimate). The back action can thus be neglected as a first approximation.

As for the adiabatic approximation, the value of $\Omega = \hbar\omega/eRI_c$ depends on the resistance of the junction. For tunnel junctions the low-temperature resistance is due only to quasi-particle tunneling and increases exponentially with decreasing temperature; at temperatures close to the critical temperature the resistance can be estimated with the normal state resistance and $I_c R_n$ can be as large as 1mV, corresponding to $\omega^* \simeq 10^{12}$Hz. In such situations the adiabatic approximation could apply. However the resistance of a Josephson junction can vary greatly and thus the validity of the adiabatic approximation depends on the device.

Chapter 5

Quantum spectrum of a SQUID-NEMS

The first nanomechanical resonator in its quantum ground state has recently been realized[69]; it was a plate made of a piezoelectric material, whose deformations could produce an electric field that increased the restoring force, thus reaching a very proper frequency of the fundamental mode. Although the physics of suspended nanobeams is quite different, it is reasonable to expect that the quantum regime will soon be avilable for them as well. In fact this regime has already been widely explored in the theoretical literature [96, 97, 98, 99, 100, 101, 102, 103, 28, 104, 105]; however, nanobeams are usually very weakly coupled to electrical circuits, although many smart coupling schemes have already been devised. The case of a SQUID in the quantum regime with a vibrating arm has been also investigated actively in the past few years [106, 86, 88, 90, 107].

In this chapter we address the question of how to optimize the coupling between a suspended nanobeam and a quantum SQUID for detection purposes. A natural way to detect the quantum motion of the mechanical resonator would be through a spectroscopy measurement of the energy level spectrum by standard techniques developed for flux qubits [108]. Indeed the coupling of a few-level quantum system (the SQUID) with an external field can show up in the spectrum in different ways depending on whether the external field is classical or quantum[109, 110]. In any case, it is crucial that the resonant coupling regime is realized in order to produce more visible effects in a spectroscopic measurement. The focus of our study is how to make this possible by tuning the external magnetic field and the bias current with available experimental setups. Furthermore we also discuss a strategy to optimize the resonant coupling between the resonator and the SQUID, thus maximizing the splitting of an energy level associated with the SQUID

due to the coupling to a resonator.

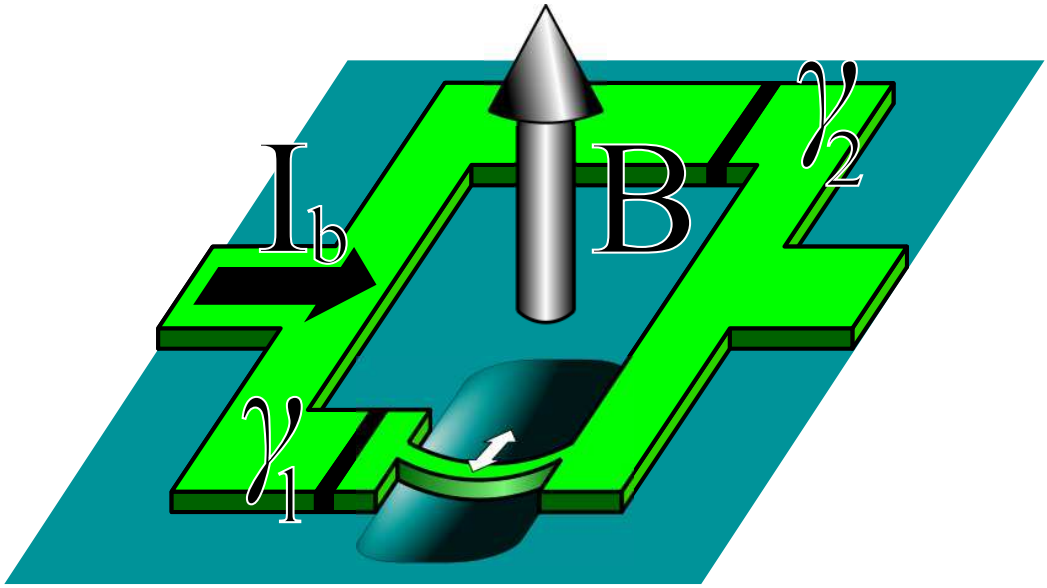

Figure 5.1: A sketch of the device we study: one arm of a dc SQUID is free to oscillate in the plane of the SQUID itself. A uniform magnetic field B orthogonal to the SQUID plane is present and a dc bias current I_b flows through the device. The two Josephson junctions, whose phase drops are respectively γ_1 and γ_2, are taken to be identical.

5.1 Formal description of the setup

The system we consider is schematically drawn in Fig. 5.1. A dc SQUID is made of a superconducting loop of total area A with an arm of mass m that can oscillate freely in the plane of the loop. For simplicity we assume that only a single mode of oscillation with the frequency ω can be excited. This mode is a flexural mode, with the arm oscillating in the plane of the SQUID; for small displacements from the equilibrium position, the area swept by the motion of the vibrating arm can be described as the product of the dynamical variable X, representing the shift of the center-of-mass of the resonator with respect to its rest position, and a parameter l, an effective length of the nanobeam. The quantum effects related to mechanical motion of this oscillator appear at the scale of the amplitude of zero-point motion $X_0 = \sqrt{\hbar/2m\omega}$. The SQUID further comprises two Josephson junctions of equal critical currents I_c and shunting capacitances C; the typical energy scales

related to the physics of the junctions are the Josephson energy $E_J = \hbar I_c/2e$ and the charging energy $E_c = (2e)^2/2C \ll E_J$, whose magnitude depends on the geometry of the junctions. The typical time scale for the dynamics of the junctions is set by the inverse plasma frequency $\omega_{\rm pl} = \sqrt{2E_J E_c}/\hbar$. The dynamics of the SQUID is described by the two gauge-invariant phase drops γ_1 and γ_2 across the two junctions.

The coupling of the SQUID dynamics to mechanical motion is provided by the position dependence of the magnetic flux threading the SQUID loop. The two phases are constrained by the requirement that the superconducting order parameter is single valued,

$$\gamma_1 - \gamma_2 = 2\pi \left(\frac{\Phi}{\Phi_0} + n \right) , \tag{5.1}$$

where $\Phi_0 = h/2e$ is the flux quantum; the total flux Φ is the sum of three contributions. The first comes from the external bias $\Phi_e = BA \equiv \Phi_0 \phi_e$, while the second $\Phi_m = BlX$ depends on the position of the mechanical resonator and provides the coupling between the mechanical resonator and the SQUID. If the circuit also has non-negligible self inductance L, the third contribution to the total flux Φ comes from the current circulating in the loop; if I_1 and I_2 are the currents flowing through each junction, the self-induced flux reads $L(I_1 - I_2)/2$. This device has three degrees of freedom; if $L = 0$, then the constraint expressed by Eq. (5.1) reduces the number of degrees of freedom from three to two. In the following, we assume that the dissipation effects are negligible.

It is useful to describe the system in terms of three dimensionless variables $\gamma = (\gamma_1 + \gamma_2)/2$, $\phi = \Phi/\Phi_0$ and $\xi = BlX/\Phi_0$. The potential energy of the system reads

$$\begin{aligned} U = E_J \Bigg[& -2\cos\gamma\cos(\pi\phi) - \frac{I_b}{I_c}\gamma - \pi\frac{I_b}{I_c}\xi + \frac{\xi^2}{2\mathscr{A}^2} + \\ & + \frac{2\pi}{\beta_L}(\phi - \xi - \phi_e)^2 \Bigg] , \end{aligned} \tag{5.2}$$

where the first term on the r.h.s. is the sum of the Josephson energies associated to the two junctions, the second term is the well-known tilting term of the "tilted-washboard potential", the third term is necessary for getting the correct Lorentz force acting on the vibrating arm, the fourth term is the elastic potential energy and the last term represents the inductive energy of the loop due to the flux generated by the circulating current. We have also introduced the parameters

$$\mathscr{A} = \sqrt{\frac{2E_J}{\hbar\omega}}\frac{BlX_0}{\Phi_0} \; ; \; \beta_L = \frac{2LI_c}{\Phi_0} \; . \tag{5.3}$$

The parameter $\mathscr{A}$ is proportional to the flux threading the area swept by the mechanical resonator and plays the role of a coupling parameter, as we show below. Typical values of $\mathscr{A} = 4 \times 10^{-5}$ can be obtained assuming $I_c = 1\mu$A, $\omega = 1$GHz, $l = 1\mu$m, $X_0 = 10$fm and $B = 0.1$T.

5.2 Detection scheme

Quantum coherence in the motion of the mechanical resonator can be detected via spectroscopic measurements on the quantum SQUID. Indeed, the energy levels associated with the SQUID degrees of freedom are shifted due to the coupling to the oscillator. However, this shift is of the second order in the coupling and for realistic experimental parameters is very small. Therefore, below we employ a different scheme which provides a result of the first order in the coupling. One first chooses an appropriate set of values for the externally controllable quantities I_b and Φ_e such that the system can be trapped in a minimum in which one of the eigenfrequencies of the electromagnetic modes is the same as the frequency of mechanical oscillations (to be referred below as *degeneracy condition*); then one moves slightly away from this degeneracy condition by changing the remaining external parameter. A plot of the energy levels as functions of the external parameters should display an avoided level crossing, which is a clear indication that the SQUID is coupled to a coherent quantum system.

When the temperature is low enough for the system to reach the quantum regime, the coordinates typically oscillate around a minimum of the potential corresponding to the values $\bar{\gamma}$, $\bar{\phi}$ and $\bar{\xi}$. We can approximate the dynamics as a three-dimensional harmonic oscillator, with the energy being a quadratic form,

$$E_{\rm tot} = \sum_i \frac{\hbar^2}{2E_c}\dot{q}_i^2 + \sum_{i,j} E_J V_{ij} q_i q_j \ , \tag{5.4}$$

where the coordinates q_i read

$$q_1 = \gamma - \bar{\gamma};\ q_2 = \pi(\phi - \bar{\phi});\ q_3 = \frac{1}{\Omega}\frac{1}{\sqrt{2}\mathscr{A}}(\xi - \bar{\xi})\,, \tag{5.5}$$

and

$$V = \begin{pmatrix} r & -s & 0 \\ -s & r + \dfrac{2}{\pi\beta_L} & -\dfrac{2\sqrt{2}\mathscr{A}}{\beta_L}\Omega \\ 0 & -\dfrac{2\sqrt{2}\mathscr{A}}{\beta_L}\Omega & \left(1 + \dfrac{4\pi\mathscr{A}^2}{\beta_L}\right)\Omega^2 \end{pmatrix} . \tag{5.6}$$

(We have introduced $r = \cos\bar{\gamma}\cos(\pi\bar{\phi})$, $s = \sin\bar{\gamma}\sin(\pi\bar{\phi})$ and $\Omega = \omega/\omega_{\rm pl}$). The coupling V_{23} between the mechanical resonator and the SQUID is proportional to the ratio $\mathscr{A}/\beta_L$ (for devices with a low self-inductance this behavior no longer holds, see below for discussion); the decoupled regime can be obtained for either $B \to 0$ or $L \to \infty$. The coordinate $q_1 = \gamma - \bar{\gamma}$, corresponding to one of the electromagnetic degrees of freedom, oscillates with the frequency $\omega_{\rm pl}\sqrt{\cos\bar{\gamma}\cos(\pi\bar{\phi})}$; therefore if a minimum $(\bar{\gamma}, \bar{\phi}, \bar{\xi})$ is such that

$$\cos\bar{\gamma}\cos(\pi\bar{\phi}) = \Omega^2\,, \tag{5.7}$$

the frequencies associated with the motion of average phase drop γ and oscillator motion coincide up to correction of second order in $\mathscr{A}$; we show below that the equality is indeed exact to all orders in the coupling. Eq. (5.6) is exact up to quadratic terms in the displacement from the equilibrium position; however it is not suitable for describing devices with generic values of the self-inductance parameter β_L, since four matrix elements diverge for $\beta_L \to 0$. These divergences reflect the fact that for $\beta_L = 0$ only two degrees of freedom should remain, the value of the third coordinate being fixed by the other two. A description could be obtained by switching to a basis in which the diverging subblock is diagonal; without any loss of generality, the new form is suitable for all situations, including $\beta_L \simeq 0$. The analytic expression for the matrix in the new basis is quite cumbersome; below we give this expression for the case in which the degeneracy condition (5.7) holds,

$$V' = \begin{pmatrix} \Omega^2 & -s\dfrac{\sqrt{2}\pi\mathscr{A}}{C}\Omega & \dfrac{s}{C} \\ -s\dfrac{\sqrt{2}\pi\mathscr{A}}{C}\Omega & \Omega^2 & 0 \\ \dfrac{s}{C} & 0 & \Omega^2 + \dfrac{2C^2}{\pi\beta_L} \end{pmatrix}\,, \tag{5.8}$$

with $C = \sqrt{2\pi^2\mathscr{A}^2\Omega^2 + 1}$. The first and second row and column correspond to the phase drop γ and to the mechanical degree of freedom, respectively. The parameters I_b and Φ_e corresponding to the degeneracy condition are found if one solves the equation set,

$$\begin{cases} I_b/I_c = 2\sin\bar{\gamma}\cos(\pi\bar{\phi}) \\ 2\beta_L^{-1}(\bar{\phi} - \phi_e - \bar{\xi}) = -\cos\bar{\gamma}\sin(\pi\bar{\phi}) \\ \bar{\xi} = 4\pi\mathscr{A}^2\beta_L^{-1}\left(\bar{\phi} - \phi_e - \bar{\xi} + (\beta_L I_b)/(4I_c)\right) \\ \cos\bar{\gamma}\cos(\pi\bar{\phi}) = \Omega^2\,, \end{cases} \tag{5.9}$$

where the first three lines are satisfied by stationary points of the potential energy (5.2) and the fourth line is the degeneracy condition. In a minimum

one must have $V > 0$. The unknowns are the coordinates $(\bar{\gamma}, \bar{\phi}, \bar{\xi})$ of the minimum and Φ_e; we use I_b to tune the system to the degeneracy point[1].

Next, we quantize the system. The Hamiltonian reads

$$H = \sum_{i=1}^{3} \hbar\omega_i a_i^\dagger a_i + \sum_{i\neq j} \frac{1}{4}\hbar\omega_{\rm pl} \frac{\omega_{\rm pl}}{\sqrt{\omega_i\omega_j}} V'_{ij}(a_i^\dagger + a_i)(a_j^\dagger + a_j) \tag{5.10}$$

with $\omega_i = \omega_{\rm pl}\sqrt{V'_{ii}}$. When the condition (5.7) is fulfilled, the first excited levels $|100\rangle$ and $|010\rangle$ are quasi-degenerate and the Hamiltonian (5.10) restricted to their subspace becomes

$$H = \begin{pmatrix} \hbar\omega & \lambda \\ \lambda & \hbar\omega \end{pmatrix}, \quad \lambda = \frac{1}{4}\hbar\omega_{\rm pl}\frac{1}{\Omega}V'_{\xi\gamma}\,. \tag{5.11}$$

5.3 Results

Fig. 5.2 shows the dependence of the dimensionless level splitting $\lambda/\hbar\omega_{\rm pl}$ on the dimensionless external flux ϕ_e. The maximum level splitting is obtained for a specific value of the external flux and depends very weakly on the loop self-inductance; however the value of the flux at which the maximum is achieved does depend on the loop self-inductance; see below for further discussion. The magnitude of the splitting is of the order of $10^{-5}\hbar\omega_{\rm pl}$. The value of the ratio $\Omega = \omega/\omega_{\rm pl}$ plays an important role: lower values correspond to bigger maximum splittings and are thus preferable.

To enable the detection, the potential well formed at the chosen minimum must be capable of containing quantum states. The number of bound states can be estimated by the ratio between the energy difference ΔU between the minimum and the closest saddle point and the energy level separation, which is roughly $\hbar\omega$,

$$\frac{\Delta U}{\hbar\omega} = \frac{\Delta U}{E_J}\frac{1}{\Omega}\sqrt{\frac{E_J}{2E_c}} \equiv \Delta u\sqrt{\frac{E_J}{2E_c}}\,. \tag{5.12}$$

Fig. 5.3a displays plots of the quantity Δu, defined by Eq. (5.12), as a function of Ω for different values of the self-inductance parameter β_L; one sees that small values of Ω correspond to very shallow minima in the potential energy, whereas the deepest minima correspond to devices in which $\omega = \omega_{\rm pl}$. However Fig. 5.3b shows that for these devices no gap is expected in the first order in the coupling; this rather surprising fact can be further illustrated by considering the dependence of the matrix element $V'_{\gamma\xi}$ on $s = \sin\gamma\sin(\pi\phi)$ in

[1] In principle one, many or no solutions can exist for a particular set of parameters; when more then one solution exists, we take the one with the larger gap λ.

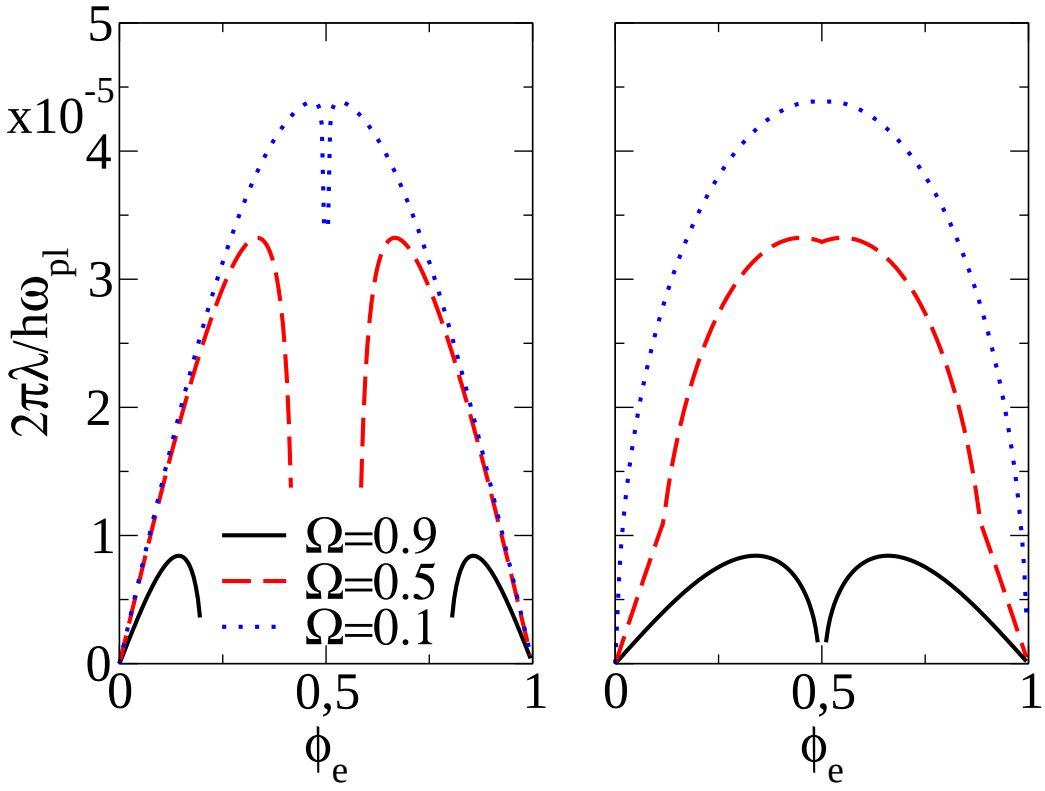

Figure 5.2: Dimensionless splitting $\lambda/\hbar\omega_{\rm pl}$ versus the external flux ϕ_e for the coupling parameter $\mathscr{A} = 4 \times 10^{-5}$. The self-inductance parameter β_L is 10^{-4} for the left panel and 1 for the right panel. Dotted, dashed, and solid lines correspond to $\Omega = \omega/\omega_{\rm pl} = 0.1, 0.5$ and 0.9, respectively. The plots are periodic, the period being one flux quantum.

Eq. (5.8): for $\Omega = 1$, one has $\cos\gamma\cos(\pi\phi) = 0$ and thus $s = 0 = \lambda$. Because of this trade-off, the optimal condition corresponds to an intermediate case. Note however that Δu depends on E_J and E_c only via the ratios $\Omega = \omega/\omega_{\rm pl}$ and I_b/I_c and thus can be tuned independently of E_J/E_c. Therefore a bigger minimum depth can be obtained by designing the SQUID so that the ratio E_J/E_c is large.

We now comment on the role of the self-inductance. The curve in Fig. 5.3b is very little affected by the value of β_L, implying that this parameter is not relevant for improving the splitting λ; on the contrary, the curves in Fig. 5.3a show that the dimensionless depth Δu of the minimum well is drastically reduced by increasing the self-inductance of the loop. Thus loops of smaller self-inductance are preferable.

Finally, Fig. 5.4 represents numerical solutions of Eqs. (5.9) used in the

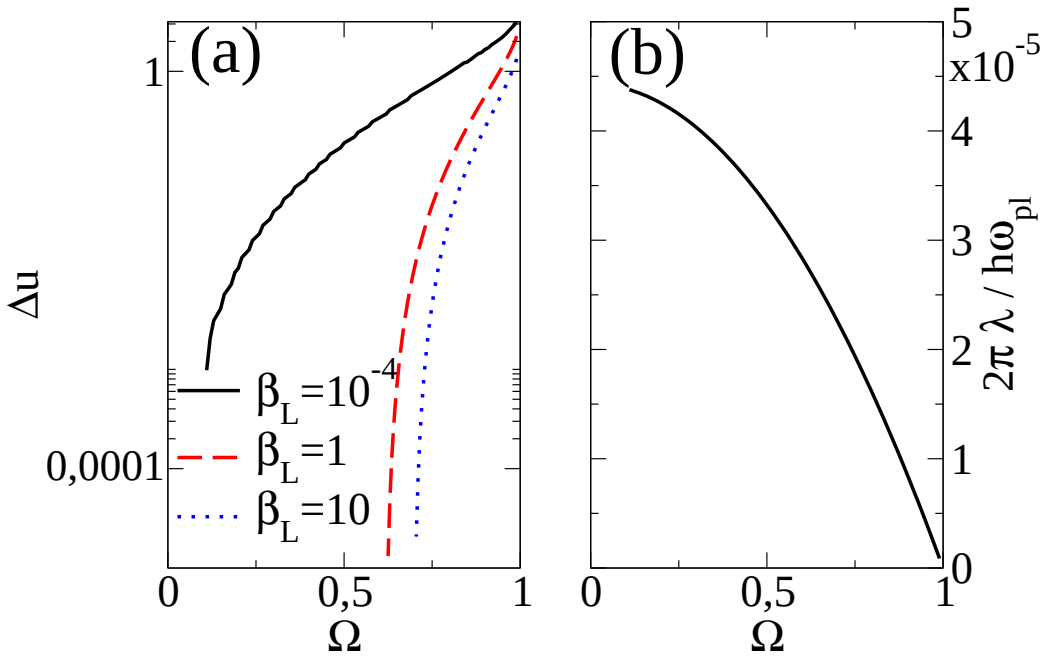

Figure 5.3: (a) the dimensionless depth Δu of the minimum featuring maximum splitting λ is plotted as a function of the ratio $\Omega = \omega/\omega_{\rm pl}$, for different values of the self-inductance parameter: $\beta_L = 10^{-4}$ (solid line), $\beta_L = 1$ (dashed line) and $\beta_L = 10$ (dotted line). (b) the maximum value of the dimensionless splitting $\lambda/\hbar\omega_{\rm pl}$ is plotted as a function of Ω; here $\beta_L = 1$, but the result is independent of β_L.

previous figures. The right panel shows the values of the dimensionless external parameters I_b/I_c and ϕ_e that correspond to the maximum value of the gap λ for values of Ω between 0 and 1, while the left panel shows a plot of the coordinates $(\bar{\gamma}, \bar{\phi})$ of the best minimum. As expected, the results are symmetric with respect to simultaneous current inversion $I_b \to -I_b$ and flux reflection $\phi_e \to 1 - \phi_e$; this can be seen from Eqs. (5.9), where in this case if $(\gamma, \phi, \xi, I_b/I_c)$ is a solution, then also $(\pi - \gamma, 1 - \phi, -\xi, -I_b/I_c)$ solves the equations.

5.4 A few words on the effect of dissipation

In this presentation we ignored the finite quality factor of the resonator and the decoherence of the SQUID. In this respect the required analysis goes exactly along the same lines as, for example, discussed in [108]. Damping should be small enough so that the line width be small as compared with

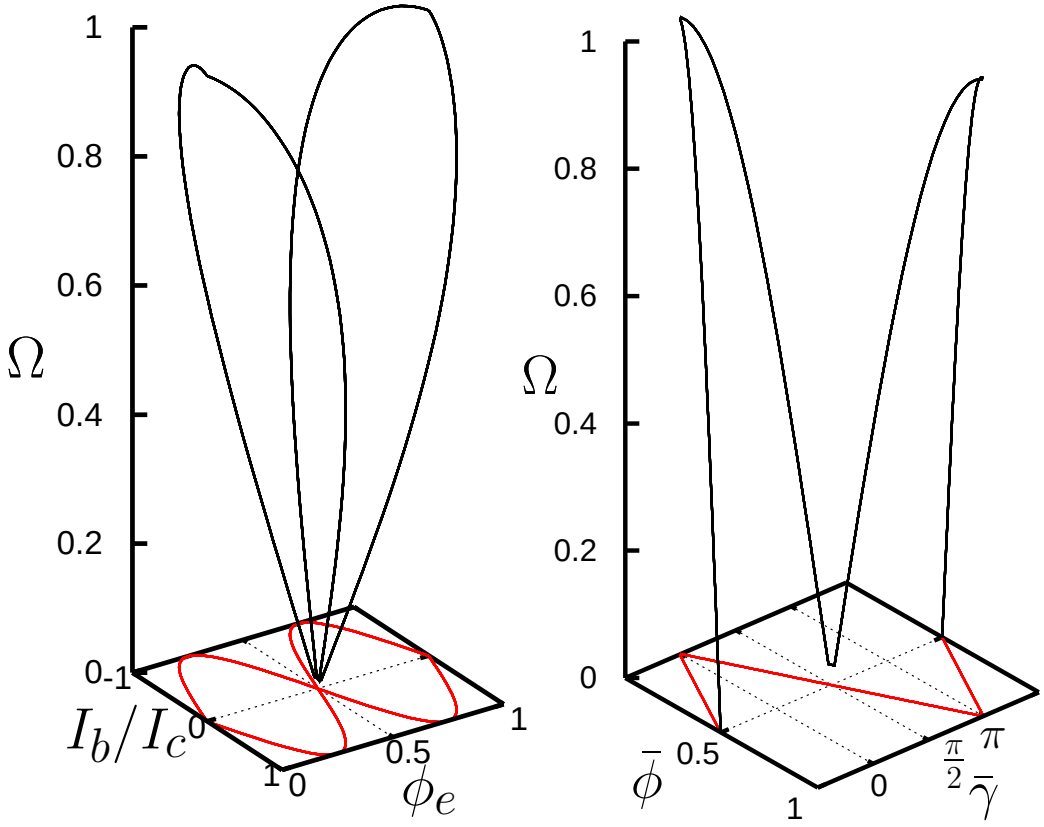

Figure 5.4: Plots of the solutions of Eqs. (5.9) giving maximum value of the dimensionless splitting $\lambda/\hbar\omega_{\rm pl}$; left panel $(I_b/I_c, \phi_e, \Omega)$, right panel $(\bar{\phi}, \bar{\gamma}, \Omega)$. A projection of the points onto to the horizontal plane is also displayed for the reader's convenience.

the energy splitting. The absolute value of the splitting depends on the bare plasma frequency $\omega_{\rm pl} = \sqrt{2E_cE_J}/\hbar$ of the SQUID; for $\omega_{\rm pl} \sim 100$GHz, the splitting 2λ can be as large as several MHz. Therefore if both the dephasing time of the SQUID and the decay time of the mechanical oscillator exceed 1μs, the avoided crossing in the spectrum should be observable; for quantum SQUIDs this has already been reported [111], whereas for GHz mechanical resonators it should not be a problem if using suspended carbon nanotubes as oscillators [2].

[2]Meerwaldt H., private communication.

Chapter 6

Detecting phonon-blockade with photons

Since the early days of quantum mechanics the crossover to the classical world and the possibility that macroscopic objects could exhibit quantum behavior has attracted continuous interest. The tremendous progress in nano-fabrication capabilities has made these questions amenable to experimental testing. Stimulated by the ideas of Leggett [112, 113], macroscopic quantum effects were first explored in Josephson junctions [114] and nanomagnets [115]. In the recent past, the field of nanoelectromechanical systems has received much attention as a very promising ground for the investigation of these questions [116, 117, 118, 78, 69] and the observation of a mechanical oscillator in its quantum ground state [69] is one of the most important achievements reached so far.

The coupling of a quantum nano-mechanical oscillator to a qubit makes NEMS also suitable systems for exploring the physics of circuit/cavity-QED [119, 120]. Different schemes have been proposed including coupling to Cooper-pair boxes [97, 98, 99, 100, 101, 102] and phase qubits [96, 103]. Recently, coupling to a Cooper-pair box has been realized experimentally [105]. Among the numerous interesting aspects of circuit-QED realized with mechanical resonators, here we want to address the phenomenon of *phonon blockade*, which was considered recently in [121], extending to NEMS the original ideas put forward with photons in cavity-QED systems [122, 123, 124]. The blockade effect arises because the coherent coupling of the harmonic (photonic/phononic) mode with the (solid-state) atom leads to an effective non-linearity. For sufficiently strong coupling, the non-linearity is such that, upon external driving, the number of excitations of the oscillator never exceeds one. Observation of phonon blockade in a nano-mechanical oscillator would be clear evidence of its quantum nature [121].

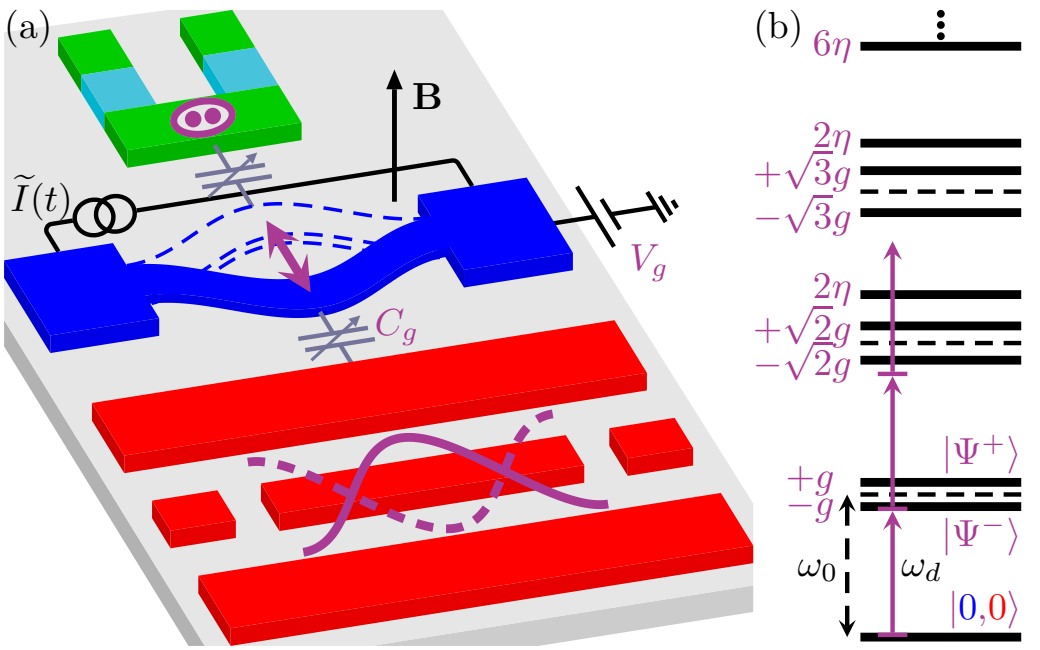

Figure 6.1: (a) Scheme of the system. A mechanical resonator is capacitively coupled to an artificial atom to induce a non-linearity and to a superconducting microwave resonator to detect phonon blockade. (b) Energy spectrum of the system for $\eta \gg g$, not to scale. The first excited states are the maximally entangled Bell states $|\Psi^{\pm}\rangle$ and the frequency of the transition from the ground state to these first-excited states is off resonance with the transitions to the states with more than one excitation. When the system is driven at the frequency $\omega_d = \omega_0 \pm g$, phonon blockade is observed through the photon statistics.

There is, however, an important challenge which needs to be tackled with respect to the demonstration of phonon blockade: its detection. The motion of a mechanical oscillator close to its ground state is tiny and strong amplification of the transduced signals must be applied. On the other hand, amplification will inevitably add classical correlations to the signal, thus disguising quantum correlations which are usually needed for demonstrating phonon blockade.

In this article we show that these problems may be overcome if a Superconducting Microwave Resonator (SMR) is coupled linearly to the mechanical oscillator for transducing its motion into an electric signal. SMRs have proven to be nearly ideal quantum oscillators with easily tunable quality factors and they can be efficiently coupled to coherent quantum circuits [125, 126, 127, 128]. Our analysis is amenable to experimental veri-

fication. Recently, good coupling of a nano-mechanical resonator and a SMR has been demonstrated [129, 130, 131]. Moreover, despite the difficulties in dealing with a microwave field at the level of a single photon, very recently it has been shown that time correlation functions for the cavity field can be measured accurately [132, 133, 134].

The system we have in mind is depicted in Fig. 6.1. It is a mechanical resonator coupled capacitively to an artificial atom and a SMR. The non-linearity, leading to phonon blockade, is induced by coupling the oscillator to a superconducting qubit. In the case of a Cooper-pair box, one gets the Jaynes-Cummings model. A Cooper-pair box molecule [135] may be considered as well in order to increase the non-linearity. In the present work, however, we do not deal with a specific choice of the superconducting nano-circuit; the important ingredient is the generation of a Kerr Hamiltonian proportional to $a^\dagger a^\dagger aa$ [136], where a and $a^\dagger$ are the phonon annihilation and creation operators of the mechanical oscillator. After the adiabatic elimination of the qubit, the Non-linear Mechanical Resonator (NMR) is described by the following effective Hamiltonian

$$H_{\rm NMR} = \hbar\omega_r a^\dagger a + \hbar\eta a^\dagger a^\dagger aa. \tag{6.1}$$

The mechanical resonator is supposed to be in the quantum regime (the bare frequency is in the gigaHertz range). For a strong coupling of hundreds of megaHertz, the Kerr non-linearity strength η is of the order of megaHertz. The coupling between the NMR and the SMR is obtained from circuit theory. The cavity is modeled by an array of LC circuits [128]. The Hamiltonian of the fundamental mode of the SMR is $H_{\rm SMR} = \hbar\omega_c b^\dagger b$, where $\omega_c/2\pi$ is the mode frequency and b ($b^\dagger$) the corresponding photon annihilation (creation) operator.

The mechanical resonator is kept at a fixed potential V_g with respect to ground and the coupling is realized through a localized capacitance $C_g = C_g^0 + (a + a^\dagger)C_g^1$, resulting in two coupling terms in the Hamiltonian: a radiation pressure term $C_g^1 V_{\rm r.m.s.}^2 a^\dagger a(b + b^\dagger)$ and a linear term $C_g^1 V_g V_{\rm r.m.s.}(a + a^\dagger)(b + b^\dagger)$, coming from the electrostatic energy of the coupling capacitor ($V_{\rm r.m.s.}$ is the root mean square of the zero-point voltage fluctuation of the SMR at the position of the coupling capacitance). These two terms can have very different orders of magnitude for typical values of V_g and $V_{\rm r.m.s.}$ [137]. We focus on the case where the gate voltage is much larger than the root mean square of the voltage quantum fluctuations inside the SMR, and thus neglect radiation pressure. In the rotating wave approximation, the coupling reads

$$H_{\rm int} = \hbar g \left(a^\dagger b + a b^\dagger\right), \tag{6.2}$$

where $g = C_g^1 V_g V_{\text{r.m.s.}}/\hbar$. For realistic parameters, the coupling may be of the order of megaHertz. The mechanical resonator is driven by a weak oscillating current, at the frequency $\omega_d/2\pi$, in the presence of a static magnetic field perpendicular to the plane of the circuit. This driving is modeled by the Hamiltonian

$$H_{\text{drv}} = \hbar\epsilon \left(a^\dagger e^{-i\omega_d t} + a e^{i\omega_d t}\right), \tag{6.3}$$

where the strength ϵ is proportional to the current amplitude and the magnetic field. The total Hamiltonian of the system reads $H = H_{\text{NMR}} + H_{\text{SMR}} + H_{\text{int}} + H_{\text{drv}}$. We choose the working point at $\omega_r = \omega_c \equiv \omega_0$.

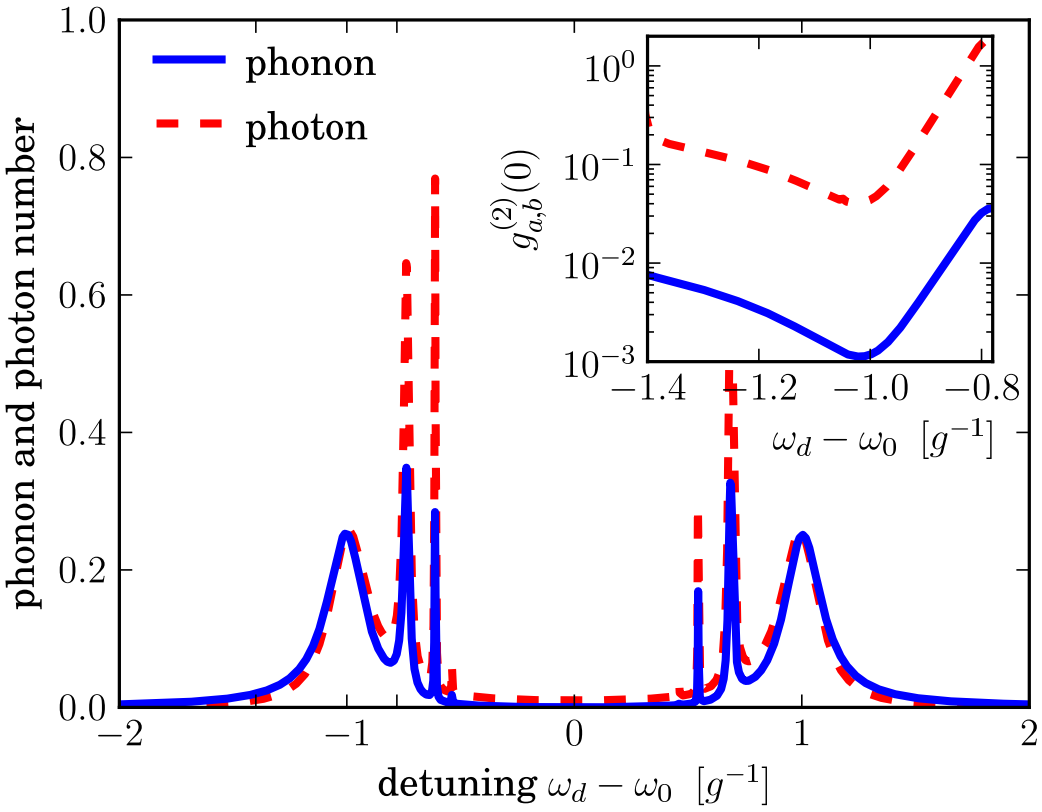

Figure 6.2: Spectroscopy of the energy spectrum. Steady-state phonon number (solid line) and photon number (dashed line) as a function of the driving frequency. The different peaks correspond to the excitation of the states with one phonon $|1, n_c\rangle$. Inset: Second order correlation functions at coinciding times for the phonons $g_a^{(2)}(0)$ and for the photons $g_b^{(2)}(0)$. Anti-bunching occurs at $\omega_d = \omega_0 \pm g$ where phonon and photon blockade take place. Photon bunching occurs when the states with many photons are excited.

The finite lifetime of the phonons and the photons is taken into account

through the Lindblad operators L_r and L_c of the resonator and the cavity, respectively [138, 139] (ρ is the density matrix of the whole system)

$$L_r\rho = \tfrac{1}{2}\gamma_r \left(2a\rho a^\dagger - a^\dagger a\rho - \rho a^\dagger a\right), \tag{6.4a}$$

$$L_c\rho = \tfrac{1}{2}\gamma_c \left(2b\rho b^\dagger - b^\dagger b\rho - \rho b^\dagger b\right), \tag{6.4b}$$

where the damping rates $\gamma_{r,c} = \omega_{r,c}/Q_{r,c}$ are the inverse of the phonon and photon lifetime and are defined by the quality factors $Q_{r,c}$. The dynamics of the system is then governed by the master equation

$$\partial_t\rho(t) = \frac{1}{i\hbar}\left[H, \rho(t)\right] + L\rho(t), \tag{6.5}$$

where $L = L_r + L_c$ is the total Lindbladian.

In principle, some noise is introduced by the voltage source used to keep the mechanical resonator at V_g. However, following Ref. [140], the dominant Lindblad operator corresponding to this source of noise for the case of a Markovian environment is found to be of the order of $\eta g R C_g^1 V_{\text{r.m.s.}}/V_g$ (R is the internal resistance of the voltage source), which is negligible due to the very small value of gRC_g^1. In the case of slow voltage fluctuations, one can also neglect noise effects, as we discuss below.

Blockade is possible only if the non-linearity of the energy spectrum is larger than the state linewidth, namely $\eta, g > \gamma_{r,c}$. This condition imposes the quality factors to be at least several thousand, which is within the experimental capabilities. Throughout the present work we chose the following parameters for the numerical simulations: $\omega_0/2\pi = 1\,\text{GHz}$, $\eta/2\pi = 10\,\text{MHz}$, $g/2\pi = 1\,\text{MHz}$, $Q_r = 10^5$, and $Q_c = 10^6$. Moreover, the NMR is driven at the resonance $\omega_d = \omega_0 - g$ with an amplitude $\epsilon/2\pi = 0.1\,\text{MHz}$. By analyzing the time traces of the photon and phonon populations (not shown here) it is possible to note that the cavity closely resembles the dynamics of the NMR, with equal steady state phonon and photon numbers close to 0.25. The population of the state with two phonons or two photons is strongly suppressed, implying both phonon and photon blockade. In the rest of the paper, we will show by a solution of Eq. (6.5) that by means of the detection of photon correlations it is possible to extract unique information on the phonon statistics.

In order to ascertain the accuracy of the proposed detection scheme, it is not sufficient to see a correlation in the populations. We analyze the statistics of the excitations by means of the second order correlation function [141]

$$g_y^{(2)}(\tau) = \lim_{t\to\infty} \frac{\langle y^\dagger(t)y^\dagger(t+\tau)y(t+\tau)y(t)\rangle}{\langle y^\dagger(t)y(t)\rangle^2}, \tag{6.6}$$

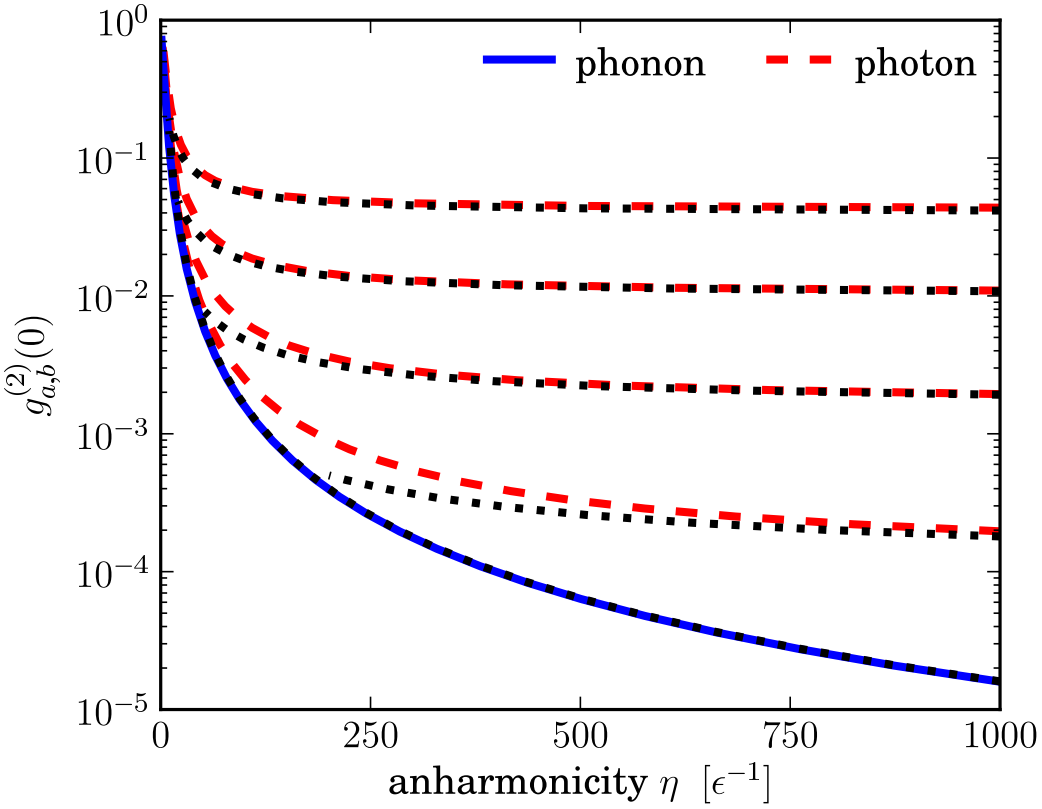

Figure 6.3: Second order correlation functions $g^{(2)}_{a,b}(0)$ of the NMR (solid line) and the SMR (dashed lines) as a function of the Kerr non-linearity for different values of the coupling. From top to bottom, $g/2\pi = 1,\ 2,\ 5,\ 20\,\mathrm{MHz}$ respectively. The correlation of the NMR is essentially coupling-independent while for large η the correlation of the SMR saturates to a constant value $(2\epsilon/g)^2$. The corresponding solutions Eq. (6.9) in the limit $\eta \gg g$ are plotted in dotted lines.

where $y = a$ or b. The value of $g^{(2)}_{a,b}(\tau)$ is comprised between 0 and 2 and tends towards unity for long time difference, where the coherence is lost. The value at coinciding times $\tau = 0$ reflects the statistics of the field: a value of $g^{(2)}_a(0) \ll 1$ is the signature of phonon blockade.

To understand how to induce and detect phonon blockade, we look at the energy spectrum of the undriven Hamiltonian H in the Fock basis $|n_r, n_c\rangle$, where $n_{r,c}$ is the phonon and photon number respectively. The total number of excitation $a^\dagger a + b^\dagger b$ being conserved, the spectrum can be decomposed on the subspaces defined by a given number $n = n_r + n_c$ of excitations $\{|k, n-k\rangle,\ k = 0, \ldots, n\}$. For one excitation $n = 1$, the eigenstates are the

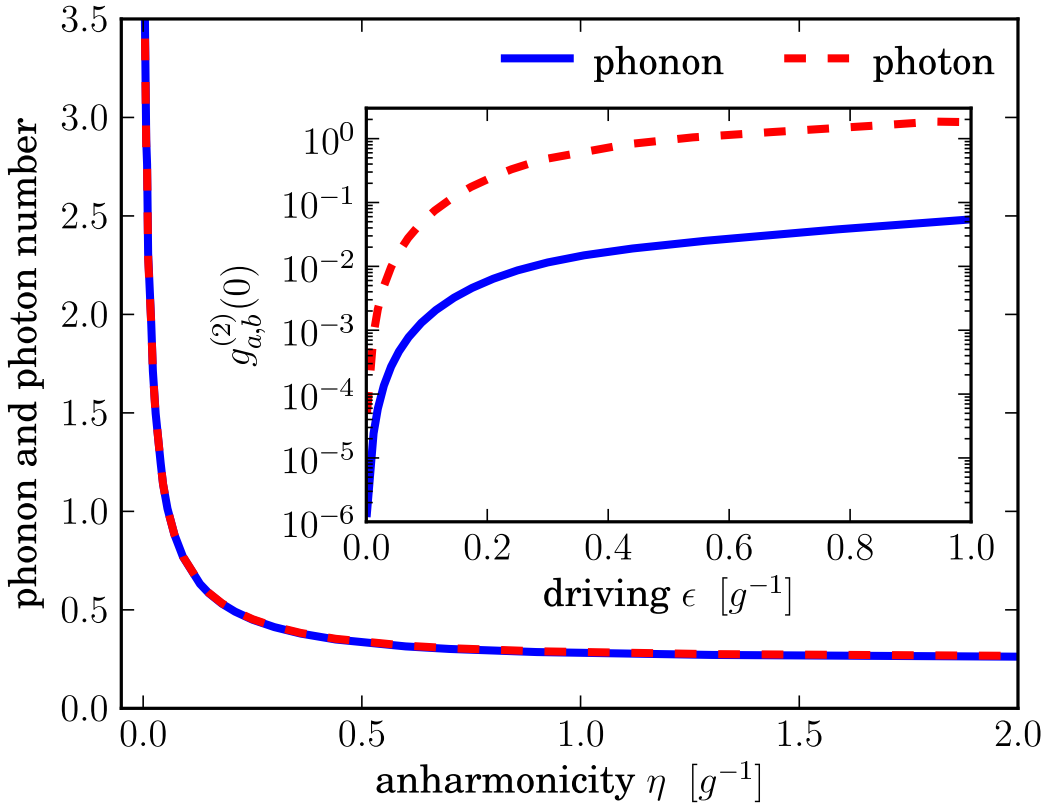

Figure 6.4: Steady state phonon number (solid line) and photon number (dashed line) as a function of the Kerr non-linearity. The Bell state $|\Psi^-\rangle$ ensures a perfect match between the phonon and photon numbers. Many excitations are generated when the non-linearity is comparable with the damping rates of the resonators, where the excitations are not anti-bunched anymore. Inset: Correlation as a function of the driving amplitude ϵ. For a strong driving, states with more than one photon are excited.

maximally entangled Bell states

$$|\Psi^{\pm}\rangle = \tfrac{1}{\sqrt{2}}\left(|0,1\rangle \pm |1,0\rangle\right), \tag{6.7}$$

with the energy $\hbar\omega_0 \pm \hbar g$. For higher excitation numbers the ladder structure depends on the ratio η/g between the anharmonicity and the coupling. In the limit of a strong non-linearity $\eta \gg g$, the spectrum is composed of two entangled states $|0,n\rangle \pm |1,n-1\rangle$ at $\omega_0 \pm \sqrt{n}g$ and $n-1$ pure states $|2,n-2\rangle, \ldots, |n,0\rangle$ located at $\hbar\omega_0 + m(m-1)\eta$, see Fig. 6.1. This non-linear spectrum allows for excitation blockade, since the energy of the state $|\Psi^{\pm}\rangle$ is not resonant with higher states. If the system is excited at the frequency $\omega_d = \omega_0 \pm g$, only one excitation is created, symmetrically shared between

the NMR and the SMR. The eigenstate being the maximally entangled Bell state $|\Psi^{\pm}\rangle$, the photons have the same dynamics as the phonons and the cavity constitutes consequently a reliable measurement device for detecting the state of the resonator through the photon statistics (see Fig. 6.4).

The energy spectrum can be probed with the response of the system to the driving current when the driving frequency is tuned, as depicted in Fig. 6.2. In order to excite states with one phonon such as $|1, n-1\rangle$, the driving frequency is fixed to $\omega_d = \omega_0 \pm g/\sqrt{n}$. These values correspond to the peaks in the excitation numbers of Fig. 6.2. Compared with the dependence of the $g^{(2)}_{a,b}(0)$ on ω_d (see the inset) it shows that blockade occurs at $\omega_d - \omega_0 = \pm g$ where the second order correlation function is minimized. This minimum protects the blockade phenomenon against slow fluctuations of the gate voltage V_g, or equivalently the coupling g. Indeed, if the driving is kept at a fixed frequency $\omega_d = \omega_0 \pm g$ and one looks at the dependence of $g^{(2)}_{a,b}(0)$ on a coupling $\tilde{g}$ fluctuating around g, one obtains a behavior analogous to the inset of Fig. 6.2, namely a minimum at $\tilde{g} = g$. The averaged value of the second order correlation function over a Gaussian distribution of coupling strengths is not affected and both phonon and photon blockade is thus insensitive to slow gate voltage fluctuations at first order. For higher values of n, the photon number increases and the second order correlation function of the cavity $g^{(2)}_b(0)$ tends to 2, indicating photon bunching.

When the anharmonicity is very large, the NMR behaves like a two-level system and can be described with the ladder operators $\sigma_+ = |1\rangle\langle 0|$ and $\sigma_- = |0\rangle\langle 1|$. The Hamiltonian is then reduced to an effective Jaynes-Cummings model

$$H_{\eta\infty} = \tfrac{1}{2}\hbar\omega_0\sigma_z + \hbar\omega_0 b^\dagger b + \hbar g(\sigma_- b^\dagger + \sigma_+ b) + \hbar\epsilon(\sigma_+ e^{-i\omega_d t} + \sigma_- e^{i\omega_d t}), \quad (6.8)$$

where $\sigma_z = [\sigma_+, \sigma_-]$. At lowest order in g/η, the asymptotic expression of the second order correlation functions is given by

$$g^{(2)}_a(0) = (4\epsilon/\eta)^2 \quad \text{and} \quad g^{(2)}_b(0) = (2\epsilon/g)^2(1 + 4g/\eta). \quad (6.9)$$

The comparison with the numerical results is presented in Fig. 6.3, where the correlation functions are plotted as a function of the anharmonicity for different values of the coupling. For a sufficiently large anharmonicity the properties of the SMR become η-independent with a strong reduction of the phonon correlation function $g^{(2)}_a(0)$. Photon blockade is enhanced when the coupling increases. In the opposite limit of a small anharmonicity, the driving generates many excitations. The transition from photon anti-bunching to photon bunching is also observed when, for a fixed anharmonicity, the coupling decreases or the driving amplitude increases. The former is due to

the degeneracy of the Bell states for small coupling $g \lesssim \gamma_{r,c}$ and the latter to an effective level broadening due to the driving.

In conclusion, we have shown that coupling a SMR to a NMR is a powerful tool to detect phonon blockade. The main reason is the formation of Bell states between the two resonators, ensuring a perfect match between the phonon dynamics and the photon statistics. Our simulations, obtained in the framework of the quantum master equations, demonstrate that our proposal is compatible with the current experimental capabilities.

Part III

Appendices

Appendix A

Keldysh formalism and perturbative evaluation of the current

In order to compute the current in the three terminal set-up, we adopt the Keldysh formalism [56], suitable to account for out-of-equilibrium properties. According to Eq. (2.14), the current at position x (located in the source or in drain leads) and time t can be written as

$$I(x,t) = \frac{ev_{\mathrm{W}}}{2} \sum_{\eta=\pm} \left\langle j^{(\eta)}(x,t) \right\rangle \tag{A.1}$$

where

$$j^{(\eta)}(x,t) = \sum_{r=\pm} r :\Psi_r^{\dagger\,(\eta)}(x,t)\Psi_r^{(\eta)}(x,t): \quad . \tag{A.2}$$

Here $\eta = +$ ($\eta = -$) corresponds to the upper (lower) branch of the Keldysh contour depicted in Fig. A.1. The current $I(x,t)$ and various other quantities introduced below also depend on the injection point x_0 and the impurity positions x_1 and x_2. These variables will frequently be suppressed to simplify notation.

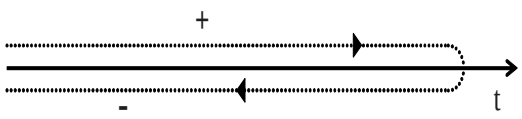

Figure A.1: Keldysh contour along the time axis.

In the Keldysh interaction picture with

$$\mathcal{H}_0 = \mathcal{H}_{\mathrm{kin,W}} + \mathcal{H}_U + \mathcal{H}_{\mathrm{kin,T}} \tag{A.3}$$

and

$$\mathcal{H}_{\rm I} = \mathcal{H}_\lambda + \mathcal{H}_{\rm tun} + \mathcal{H}_{\mu_{\rm W}} + \mathcal{H}_{\mu_{\rm T}}\,, \tag{A.4}$$

one obtains

$$\begin{aligned} & I(x,t) \qquad\qquad (A.5)\\ &= \frac{ev_{\rm W}}{2}\sum_{\eta=\pm}\left\langle T_{\rm K}\left[j^{(\eta)}(x,t)\mathrm{e}^{-\frac{i}{\hbar}\sum_{\eta'=\pm}\eta'\int_{-\infty}^{\infty}dt'\mathcal{H}_{\rm I}^{(\eta')}(t')}\right]\right\rangle_0 \end{aligned}$$

where $\langle\ldots\rangle_0$ denotes the average with respect to the equilibrium state determined by the Hamiltonian $\mathcal{H}_0$, and $T_{\rm K}$ is the Keldysh time-ordering operator. Expanding the exponent in Eq. (A.5) perturbatively in terms of γ and λ, one obtains the current to the desired order. Below we sketch the calculation of $I_{\gamma^2\lambda}$, *i.e.*, the contribution of order $\gamma^2\lambda$ to $I(x,t)$. With the abbreviations

$$\begin{aligned} \mathcal{U}_{\rm W} &= \mathrm{e}^{-\frac{i}{\hbar}\sum_{\eta'=\pm}\eta'\int_{-\infty}^{\infty}dt'\mathcal{H}_{\mu_{\rm W}}^{(\eta')}(t')}\\ \mathcal{U}_{\rm T} &= \mathrm{e}^{-\frac{i}{\hbar}\sum_{\eta'=\pm}\eta'\int_{-\infty}^{\infty}dt'\mathcal{H}_{\mu_{\rm T}}^{(\eta')}(t')} \end{aligned} \tag{A.6}$$

one obtains[56]

$$\begin{aligned} I_{\gamma^2\lambda}(x,t) &= \frac{iev_{\rm W}^3v_{\rm T}}{4}\sum_{i=1,2}\sum_{r_1,r_2=\pm}\lambda_i\gamma_{r_1}\gamma_{r_2}\iiint dt_1dt_2dt_3\\ &\quad\sum_{\eta,\eta_1,\eta_2,\eta_3=\pm}\eta_1\eta_2\eta_3\Bigg\langle T_{\rm K}\Bigg\{j^{(\eta)}(x,t)\,\mathcal{U}_{\rm W}\,\mathcal{U}_{\rm T}\\ &\times\ \left[\mathrm{e}^{-i(r_1-r_2)k_{\rm W}x_0}\Psi_{r_1}^{\dagger\,(\eta_1)}(x_0,t_1)\,c^{(\eta_1)}(0,t_1)\,c^{\dagger\,(\eta_2)}(0,t_2)\,\Psi_{r_2}^{(\eta_2)}(x_0,t_2)\right.\\ &\quad\left.+\,\mathrm{e}^{i(r_1-r_2)k_{\rm W}x_0}c^{\dagger\,(\eta_1)}(0,t_1)\,\Psi_{r_1}^{(\eta_1)}(x_0,t_1)\,\Psi_{r_2}^{\dagger\,(\eta_2)}(x_0,t_2)\,c^{(\eta_2)}(0,t_2)\right]\\ &\times\ \sum_{r_3=\pm}\mathrm{e}^{-2ir_3k_{\rm W}x_i}\Psi_{r_3}^{\dagger\,(\eta_3)}(x_i,t_3)\,\Psi_{-r_3}^{(\eta_3)}(x_i,t_3)\Bigg\}\Bigg\rangle_0\\ &= -\frac{ev_{\rm W}^3v_{\rm T}}{2}\sum_{i=1,2}\sum_{r_1,r_2=\pm}\lambda_i\gamma_{r_1}\gamma_{r_2}\iiint dt_1dt_2dt_3\sum_{\eta,\eta_1,\eta_2,\eta_3=\pm}\eta_1\eta_2\eta_3\\ &\quad\Im\Bigg\langle T_{\rm K}\Bigg\{j^{(\eta)}(x,t)\,\mathcal{U}_{\rm W}\,\mathcal{U}_{\rm T}\\ &\times\ \left[\mathrm{e}^{-i(r_1-r_2)k_{\rm W}x_0}\Psi_{r_1}^{\dagger\,(\eta_1)}(x_0,t_1)\,c^{(\eta_1)}(0,t_1)\,c^{\dagger\,(\eta_2)}(0,t_2)\,\Psi_{r_2}^{(\eta_2)}(x_0,t_2)\right]\\ &\times\ \sum_{r_3=\pm}\mathrm{e}^{-2ir_3k_{\rm W}x_i}\Psi_{r_3}^{\dagger\,(\eta_3)}(x_i,t_3)\,\Psi_{-r_3}^{(\eta_3)}(x_i,t_3)\Bigg\}\Bigg\rangle_0 \end{aligned} \tag{A.7}$$

where we have used the properties

$$\begin{aligned}\left\langle T_{\mathrm{K}}\left[A^{(\eta_A)}(t_A)B^{(\eta_B)}(t_B)\ldots Z^{(\eta_Z)}(t_Z)\right]\right\rangle^* = \\ \left\langle T_{\mathrm{K}}\left[Z^{\dagger\,(-\eta_Z)}(t_Z)\ldots B^{\dagger\,(-\eta_B)}(t_B)A^{\dagger\,(-\eta_A)}(t_A)\right]\right\rangle\end{aligned} \tag{A.8}$$

and

$$\mathcal{U}_{\mathrm{W,T}} = \left(\mathrm{e}^{-\frac{i}{\hbar}\sum_{\eta'=\pm}\eta'\int_{-\infty}^{\infty}dt'\mathcal{H}^{(-\eta')}_{\mu_{\mathrm{W,T}}}(t')}\right)^{\dagger} \quad . \tag{A.9}$$

Since the electron-electron interaction (2.8) contains only forward scattering terms, all non-vanishing wire correlation functions must involve an even number of operators with a given chirality r. This yields $r_2 = -r_1 = r_3$, so that

$$\begin{aligned}I_{\gamma^2\lambda}(x,t) = &-\frac{ev_{\mathrm{W}}^3 v_{\mathrm{T}}}{2}\gamma_+\gamma_-\sum_{i=1,2}\lambda_i\iiint dt_1dt_2dt_3 \\ &\sum_{\eta,\eta_1,\eta_2,\eta_3=\pm}\eta_1\eta_2\eta_3\sum_{r_3=\pm}\Im\Big\{\mathrm{e}^{2ir_3k_{\mathrm{W}}(x_0-x_i)} \\ &\Big\langle T_{\mathrm{K}}\Big[j^{(\eta)}(x,t)\,\mathcal{U}_{\mathrm{W}}\,\mathcal{U}_{\mathrm{T}}\Psi^{\dagger\,(\eta_1)}_{-r_3}(x_0,t_1)\,c^{(\eta_1)}(0,t_1)\,c^{\dagger\,(\eta_2)}(0,t_2) \\ &\Psi^{(\eta_2)}_{r_3}(x_0,t_2)\,\Psi^{\dagger\,(\eta_3)}_{r_3}(x_i,t_3)\Psi^{(\eta_3)}_{-r_3}(x_i,t_3)\Big]\Big\rangle_0\Big\}\end{aligned} \tag{A.10}$$

The term with $r_3 = +$ can be shown to yield the same contribution as the term with $r_3 = -$. To see this explicitly, one makes use of $\Im(z) = -\Im(z^*)$, exploits Eqs. (A.8) and (A.9), and renames variables according to $\eta \to -\eta$, $\eta_i \to -\eta_i$ $(i = 1, 2, 3)$ and $t_1 \leftrightarrow t_2$. One can then write

$$\begin{aligned}&I_{\gamma^2\lambda}(x,t) = \\ &= -ev_{\mathrm{W}}^3 v_{\mathrm{T}}\,\gamma_+\gamma_-\sum_{i=1,2}\lambda_i\iiint dt_1dt_2dt_3\sum_{\eta_1,\eta_2,\eta_3=\pm}\eta_1\eta_2\eta_3 \\ &\quad\Im\Big\{\mathrm{e}^{-2ik_W(x_0-x_i)}\,\mathrm{W}^{\eta_1\eta_2\eta_3}_{\gamma^2\lambda,i}(t_1,t_2,t_3)\,\mathrm{T}^{\eta_1\eta_2}_{\gamma^2}(t_1,t_2)\Big\}\end{aligned} \tag{A.11}$$

where

$$\begin{aligned}\mathrm{W}^{\eta_1\eta_2\eta_3}_{\gamma^2\lambda,i}(t_1,t_2,t_3) = \sum_{\eta=\pm}\Big\langle T_{\mathrm{K}}\Big[j^{(\eta)}(x,t)\,\mathcal{U}_{\mathrm{W}} \\ \Psi^{\dagger\,(\eta_1)}_{+}(x_0,t_1)\,\Psi^{(\eta_2)}_{-}(x_0,t_2)\,\Psi^{\dagger\,(\eta_3)}_{-}(x_i,t_3)\,\Psi^{(\eta_3)}_{+}(x_i,t_3)\Big]\Big\rangle_0\end{aligned} \tag{A.12}$$

contains correlation functions of wire operators, while

$$\mathrm{T}^{\eta_1\eta_2}_{\gamma^2}(t_1,t_2) = \left\langle T_{\mathrm{K}}\left[\mathcal{U}_{\mathrm{T}}\,c^{(\eta_1)}(t_1)\,c^{\dagger\,(\eta_2)}(t_2)\right]\right\rangle_0 \tag{A.13}$$

is a correlation function of the tip. These correlation functions are evaluated in App. B starting with Eq. (B.7) and (B.23), respectively. Inserting these results, one obtains

$$
\begin{aligned}
I_{\gamma^2\lambda}(x,t) = 2ev_{\mathrm{W}} \left(\frac{v_{\mathrm{W}}}{2\pi a_{\mathrm{W}}}\right)^2 \frac{v_{\mathrm{T}}}{2\pi a_{\mathrm{T}}}\, \gamma_+\gamma_- \sum_{i=1,2} \lambda_i \iiint dt_1 dt_2 dt_3 \\
\Re\Big\{ \mathrm{e}^{ie[(V_{\mathrm{S}}+V_{\mathrm{D}}-2V_{\mathrm{T}})(t_1-t_2)+(V_{\mathrm{S}}-V_{\mathrm{D}})(t_1-t_3+t_2-t_3)]/2\hbar} \\
\times \mathrm{e}^{-2i[k_{\mathrm{W}}+g^2e(V_{\mathrm{S}}+V_{\mathrm{D}}-2V_{\mathrm{G}})/\hbar v_{\mathrm{W}}](x_0-x_i)} \sum_{\eta_1,\eta_2,\eta_3=\pm} \eta_1\eta_2\eta_3 \mathrm{F}_{\mathrm{W}}^{\eta_1\eta_2\eta_3}(t_1-t_2,t_2-t_3) \\
\times \mathrm{F}_{\mathrm{T}}^{\eta_1\eta_2}(t_1-t_2)\, \mathrm{b}_{\mathrm{W},\gamma^2\lambda,i}^{\eta_1\eta_2\eta_3}(t_1-t_3,t_2-t_3)\, \mathrm{b}_{\mathrm{T},\gamma^2}^{\eta_1\eta_2}(t_1-t_2) \qquad \text{(A.14)} \\
\times \Big[\langle \partial_x\Theta(x,t)\Phi_+(x_0,t_1)\rangle_0^{\mathrm{Kel}} + \eta_1 \langle \partial_x\Theta(x,t)\Phi_+(x_0,t_1)\rangle_0^{\mathrm{ret}} + \\
+ \langle \partial_x\Theta(x,t)\Phi_-(x_0,t_2)\rangle_0^{\mathrm{Kel}} + \eta_2 \langle \partial_x\Theta(x,t)\Phi_-(x_0,t_2)\rangle_0^{\mathrm{ret}} \\
- \langle \partial_x\Theta(x,t)\Phi(x_i,t_3)\rangle_0^{\mathrm{Kel}} - \eta_3 \langle \partial_x\Theta(x,t)\Phi(x_i,t_2)\rangle_0^{\mathrm{ret}} + \\
+ \frac{1}{\pi\hbar} \iint dx'dt' \mu_{\mathrm{W}}(x') \langle T_{\mathrm{K}} \left[\partial_x\Theta(x,t)\partial_{x'}\Phi(x',t')\right]\rangle_0^{\mathrm{ret}} \Big] \Big\}
\end{aligned}
$$

where, for any pair of bosonic operators A and B, the following definitions hold

$$\langle A(t_A)B(t_B)\rangle^{\mathrm{Kel}} = \langle \{A(t_A),B(t_B)\}\rangle \qquad \text{(A.15)}$$

$$\langle A(t_A)B(t_B)\rangle^{\mathrm{ret}} = \theta(t_A-t_B)\langle [A(t_A),B(t_B)]\rangle \qquad \text{(A.16)}$$

$$\langle A(t_A)B(t_B)\rangle^{\mathrm{adv}} = -\theta(t_B-t_A)\langle [A(t_A),B(t_B)]\rangle \quad . \qquad \text{(A.17)}$$

We now observe that the last term in Eq. (A.14) can be dropped. Indeed, since it depends neither on η_i nor on t_i ($i=1,2,3$), it can be singled out of the sums $\sum_{\eta_i}$ and integrals $\int dt_i$; the remaining sums and integrations yield a vanishing result, since the corresponding expression equals the term of order $\gamma^2\lambda$ of an expansion of

$$\left\langle T_{\mathrm{K}} \left[\mathrm{e}^{-\frac{i}{\hbar}\sum_{\eta'=\pm}\eta' \int_{-\infty}^{\infty} dt' \mathcal{H}_{\mathrm{I}}^{(\eta')}(t')} \right] \right\rangle_0 \equiv 1\,. \qquad \text{(A.18)}$$

Simple transformations of the integration variables of Eq. (A.14), and use of the relations

$$\int_{-\infty}^{\infty} dt\, \langle \partial_x\Theta(x,t)\Phi_r(x_0,0)\rangle_0^{\mathrm{Kel}} = 0 \qquad \text{(A.19)}$$

$$\int_{-\infty}^{\infty} dt\, \langle \partial_x\Theta(x,t)\Phi_r(x_0,0)\rangle_0^{\mathrm{ret}} = \frac{i}{4v_{\mathrm{W}}}\left[1 + r\,\mathrm{sgn}(x-x_0)\right] \qquad \text{(A.20)}$$

obtained from the correlation functions provided in App. C, yield

$$\begin{aligned} I_{\gamma^2\lambda}(x,t) &= -\frac{ev_{\mathrm{W}}^3 v_{\mathrm{T}}}{16\pi^3 a_{\mathrm{T}} a_{\mathrm{W}}^2}\,\gamma_+\gamma_- \sum_{i=1,2}\lambda_i \iint dt_1 dt_2 \\ &\quad \Im\Big\{ \mathrm{e}^{ie[(V_{\mathrm{S}}+V_{\mathrm{D}}-2V_{\mathrm{T}})(t_1-t_2)+(V_{\mathrm{S}}-V_{\mathrm{D}})(t_1-t_3+t_2-t_3)]/2\hbar} \\ &\qquad \times \mathrm{e}^{-2i[k_{\mathrm{W}}+g^2 e(V_{\mathrm{S}}+V_{\mathrm{D}}-2V_{\mathrm{G}})/\hbar v_{\mathrm{W}}](x_0-x_i)} \\ &\qquad \times \sum_{\eta_1,\eta_2,\eta_3=\pm} \eta_1\eta_2\eta_3\; \mathrm{F}_{\mathrm{W}}^{\eta_1\eta_2\eta_3}(t_1,t_2)\,\mathrm{F}_{\mathrm{T}}^{\eta_1\eta_2}(t_1-t_2) \\ &\qquad \times \mathrm{b}_{\mathrm{W},\gamma^2\lambda,i}^{\eta_1\eta_2\eta_3}(t_1,t_2)\,\mathrm{b}_{\mathrm{T},\gamma^2\lambda,i}^{\eta_1\eta_2}(t_1-t_2) \\ &\qquad \times \left[\eta_1+\eta_2-2\eta_3+\mathrm{sgn}(x-x_0)(\eta_1-\eta_2)\right] \Big\}. \end{aligned} \tag{A.21}$$

Taking into account Eqs. (B.8), (B.16), (B.24), and (B.26), we now observe that upon reversal of Keldysh contour indices $\eta_i \to -\eta_i$ $(i=1,2,3)$,

$$\mathrm{F}_{\mathrm{W}}^{\eta_1\eta_2\eta_3}(t_1,t_2) \;\to\; \mathrm{F}_{\mathrm{W}}^{\eta_1\eta_2\eta_3}(t_1,t_2) \tag{A.22}$$

$$\mathrm{F}_{\mathrm{T}}^{\eta_1\eta_2}(t_1-t_2) \;\to\; -\mathrm{F}_{\mathrm{T}}^{\eta_1\eta_2}(t_1-t_2) \tag{A.23}$$

$$\mathrm{b}_{\mathrm{W},\gamma^2\lambda,i}^{\eta_1\eta_2\eta_3}(t_1,t_2) \;\to\; \left[\mathrm{b}_{\mathrm{W},\gamma^2\lambda,i}^{\eta_1\eta_2\eta_3}(t_1,t_2)\right]^* \tag{A.24}$$

$$\mathrm{b}_{\mathrm{T},\gamma^2}^{\eta_1\eta_2}(t_1-t_2) \;\to\; \left[\mathrm{b}_{\mathrm{T},\gamma^2}^{\eta_1\eta_2}(t_1-t_2)\right]^*, \tag{A.25}$$

implying that in Eq. (A.21) the contribution for $\eta_3 = -$ is conjugate to the one stemming from $\eta_3 = +$. Thus

$$\begin{aligned} I_{\gamma^2\lambda}(x,t) &= -\frac{ev_{\mathrm{W}}^3 v_{\mathrm{T}}}{8\pi^3 a_{\mathrm{T}} a_{\mathrm{W}}^2}\,\gamma_+\gamma_- \sum_{i=1,2}\lambda_i \iint dt_1 dt_2 \\ &\quad \Im\Big\{ \mathrm{e}^{ie[(V_{\mathrm{S}}+V_{\mathrm{D}}-2V_{\mathrm{T}})(t_1-t_2)+(V_{\mathrm{S}}-V_{\mathrm{D}})(t_1+t_2)]/2\hbar} \\ &\qquad \times \mathrm{e}^{-2i[k_{\mathrm{W}}+g^2 e(V_{\mathrm{S}}+V_{\mathrm{D}}-2V_{\mathrm{G}})/\hbar v_{\mathrm{W}}](x_0-x_i)} \\ &\qquad \times \sum_{\eta_1,\eta_2=\pm} \mathrm{F}_{\mathrm{W}}^{\eta_1\eta_2+}(t_1,t_2)\,\mathrm{F}_{\mathrm{T}}^{\eta_1\eta_2}(t_1-t_2)\,\mathrm{b}_{\mathrm{W},\gamma^2\lambda,i}^{\eta_1\eta_2+}(t_1,t_2)\,\mathrm{b}_{\mathrm{T},\gamma^2}^{\eta_1\eta_2}(t_1-t_2) \\ &\qquad \times \left[\eta_2+\eta_1-2\eta_1\eta_2+\mathrm{sgn}(x-x_0)(\eta_2-\eta_1)\right] \Big\}. \end{aligned} \tag{A.26}$$

The term $\mathrm{sgn}(x-x_0)$ appearing in the last line is positive (negative) for a measurement point x located in the drain (source) lead. Recalling that the current can be written as in Eqs. (2.16), (2.17), it is easily seen that those terms that are multiplied by $\mathrm{sgn}(x-x_0)$ yield $I_{\mathrm{T}}/2$, whereas the other ones

yield $I_{\rm M}$. Inserting Eqs. (B.8), (B.16), (B.24), and (B.26) into Eq. (A.26), and changing to dimensionless integration variables $\tau_i = tv_{\rm W}/gL$, the result (2.69) is obtained.

Similar procedures can be applied to evaluate the terms of order λ^2, λ^3 and γ^2. We find

$$I_{\lambda^2}(x,t) = -\frac{ev_{\rm W}^3}{2} \sum_{i,j=1,2} \lambda_i\lambda_j \iint dt_1 dt_2 \sum_{\eta_1,\eta_2=\pm} \eta_1\eta_2 \, \Re\left\{ {\rm W}^{\eta_1\eta_2}_{\lambda^2,ij}(t_1,t_2) e^{-2ik_{\rm W}(x_i-x_j)} \right\} , \tag{A.27}$$

$$I_{\lambda^3}(x,t) = -\frac{ev_{\rm W}^4}{2} \sum_{i,j,k=1,2} \lambda_i\lambda_j\lambda_k \iiint dt_1 dt_2 dt_3 \sum_{\eta_1,\eta_2=\pm} \eta_1\eta_2 \, \Im\left\{ {\rm W}^{\eta_1\eta_2}_{\lambda^3,ijk}(t_1,t_2,t_3) e^{-2ik_{\rm W}(x_i-x_j)} \right\} \tag{A.28}$$

and

$$I_{\gamma^2}(x,t) = -\frac{ev_{\rm W}^2 v_{\rm T}}{2} \sum_{r=\pm} \gamma_r^2 \iint dt_1 dt_2 \sum_{\eta_1,\eta_2=\pm} \eta_1\eta_2 \, \Re\left\{ {\rm W}^{\eta_1\eta_2}_{\gamma^2,r}(t_1,t_2) \, {\rm T}^{\eta_1\eta_2}_{\gamma^2}(t_1,t_2) \right\} \tag{A.29}$$

where

$${\rm W}^{\eta_1\eta_2}_{\lambda^2,ij}(t_1,t_2) = \sum_{\eta=\pm} \Big\langle T_{\rm K} \Big[j^{(\eta)}(x,t) \, \mathcal{U}_{\rm W} \times \Psi_+^{\dagger\,(\eta_1)}(x_i,t_1) \, \Psi_-^{(\eta_1)}(x_i,t_1) \, \Psi_-^{\dagger\,(\eta_2)}(x_j,t_2) \, \Psi_+^{(\eta_2)}(x_j,t_2) \Big] \Big\rangle_0 , \tag{A.30}$$

$${\rm W}^{\eta_1\eta_2}_{\lambda^3,ijk}(t_1,t_2,t_3) = \sum_{\eta,\eta_3,r=\pm} \eta_3 \Big\langle T_{\rm K} \Big[j^{(\eta)}(x,t) \, \mathcal{U}_{\rm W} \Psi_+^{\dagger\,(\eta_1)}(x_i,t_1) \, \Psi_-^{(\eta_1)}(x_i,t_1) \, \Psi_-^{\dagger\,(\eta_2)}(x_j,t_2) \, \Psi_+^{(\eta_2)}(x_j,t_2) \rho_r^{(\eta_3)}(x_k,t_3) \Big] \Big\rangle_0 , \tag{A.31}$$

and

$${\rm W}^{\eta_1\eta_2}_{\gamma^2,r}(t_1,t_2) = \sum_{\eta=\pm} \big\langle T_{\rm K} \big[j^{(\eta)}(x,t) \, \mathcal{U}_{\rm W} \, \Psi_r^{\dagger\,(\eta_1)}(x_0,t_1) \Psi_r^{(\eta_2)}(x_0,t_2) \big] \big\rangle_0 \quad . \tag{A.32}$$

Appendix B

Evaluation of W and T-factors by Bosonization

The Hamiltonian (A.3) of the interaction picture decomposes into commuting wire and tip parts, *i.e.*, $\mathcal{H}_0 = \mathcal{H}_{0,\mathrm{W}} + \mathcal{H}_{0,\mathrm{T}}$. For a non-interacting wire $\mathcal{H}_{0,\mathrm{W}} = \mathcal{H}_{\mathrm{kin,W}}$, and the wire correlation functions W introduced in Eqs. (A.12), (A.30), (A.31) and (A.32) can be factorized into products of single-particle electron correlators using Wick's theorem. In this case the W's can be evaluated straightforwardly, and the results for the contributions (A.11), (A.27), (A.28) and (A.29) to the current coincide with the corresponding terms of an expansion of the current obtained from the scattering matrix formalism. In the interacting case, however, $\mathcal{H}_{0,\mathrm{W}} = \mathcal{H}_{\mathrm{kin,W}} + \mathcal{H}_U$, and Wick's theorem cannot be applied. In this appendix we evaluate the wire correlators W using the bosonization technique.[4] We first summarize a few results of Chapter 1 for reader's convenience, and then illustrate how to compute the quantities needed for our study. The wire field operators can be represented as

$$\Psi_r(x) = \frac{\kappa_r}{\sqrt{2\pi a_{\mathrm{W}}}}\, \mathrm{e}^{ir\sqrt{4\pi}\Phi_r(x)} \tag{B.1}$$

where the fields $\Phi_\pm$ describe particle-hole excitations, and κ_r are Klein factors represented as Majorana fermions.[4] Finally, a_{W} is a cut-off length of the order of the lattice spacing.
Introducing Eq. (B.1) into Eqs. (2.3) and (2.13), one obtains

$$\mathcal{H}_{0,\mathrm{W}} = \frac{\hbar v_{\mathrm{W}}}{2} \int_{-\infty}^{\infty} dx \left\{ :\Pi^2(x) + \frac{1}{g^2(x)} \left[\partial_x \Phi(x)\right]^2 : \right\} \tag{B.2}$$

where $\Phi = \Phi_+ + \Phi_-$ and $\Pi = -\partial_x(\Phi_+ - \Phi_-)$ are conjugate bosonic fields, *i.e.*, $[\Phi(x,t), \Pi(y,t)] = i\delta(x-y)$. Finally,

$$g(x) = \begin{cases} 1 & \text{for} \quad |x| > L/2 \\ \left(1 + \frac{U}{\pi\hbar v_{\rm W}}\right)^{-1/2} & \text{for} \quad |x| < L/2 \end{cases} \tag{B.3}$$

is the inhomogeneous interaction parameter. Notice that $0 \leq g \leq 1$, where $g = 1$ describes the non-interacting case present in the leads. The limit $g \to 0$ corresponds to strongly repulsive interaction. The wire current operator Eq. (2.14) is expressed in terms of the dual field $\Theta = \Phi_+ - \Phi_-$ as

$$I(x,t) = ev_{\rm W}\langle \partial_x \Theta(x,t)\rangle \,. \tag{B.4}$$

Further, with the help of the relation

$$\rho_r(x,t) \, = \frac{\partial_x \Phi_r(x,t)}{\sqrt{\pi}} \,, \tag{B.5}$$

the term (2.6) of the Hamiltonian can be written as

$$\mathcal{H}_{\mu_{\rm W}} = \frac{1}{\sqrt{\pi}} \int_{-\infty}^{+\infty} dx \mu_{\rm W}(x) \partial_x \Phi(x) \,. \tag{B.6}$$

We start by discussing the derivation of $\mathrm{W}^{\eta_1\eta_2\eta_3}_{\gamma^2\lambda,i}(t_1,t_2,t_3)$. Inserting Eqs. (B.1), (B.4) and (B.5) into Eq. (A.11), one obtains

$$\begin{aligned} &\mathrm{W}^{\eta_1\eta_2\eta_3}_{\gamma^2\lambda,i}(t_1,t_2,t_3) = \\ &= \frac{1}{(2\pi a_{\rm W})^2} \mathrm{F}^{\eta_1\eta_2\eta_3}_{\rm W}(t_1-t_3, t_2-t_3)\, \mathrm{B}^{\eta_1\eta_2\eta_3}_{\mathrm{W},\gamma^2\lambda,i}(t_1,t_2,t_3) \end{aligned} \tag{B.7}$$

Here

$$\begin{aligned} \mathrm{F}^{\eta_1\eta_2\eta_3}_{\rm W}(t_1-t_3,t_2-t_3) &= \left\langle T_{\rm K}\left[\kappa_+^{(\eta_1)}(t_1)\kappa_-^{(\eta_2)}(t_2)\kappa_-^{(\eta_3)}(t_3)\kappa_+^{(\eta_3)}(t_3)\right]\right\rangle_0 \\ &= \theta(t_3-t_1)\theta(t_3-t_2)\eta_1\eta_2 + \theta(t_1-t_3)\theta(t_2-t_3) \\ &\quad - \theta(t_2-t_3)\theta(t_3-t_1)\eta_1\eta_3 - \theta(t_1-t_3)\theta(t_3-t_2)\eta_2\eta_3 \end{aligned} \tag{B.8}$$

accounts for the correlation function of fermionic Klein factors, whereas

$$\begin{aligned} &\mathrm{B}^{\eta_1\eta_2\eta_3}_{\mathrm{W},\gamma^2\lambda,i}(t_1,t_2,t_3) = \\ &= \sum_{\eta=\pm} \frac{\delta}{\delta J^{(\eta)}_\Theta(x,t)} \Bigg\langle T_{\rm K}\Bigg\{ \exp\Bigg(-\frac{i}{\hbar}\sum_{\eta'=\pm}\eta' \int d\mathbf{x}' \mu_{\rm W}(x') \frac{\partial_{x'}\Phi^{(\eta')}(\mathbf{x}')}{\sqrt{\pi}} \\ &\quad + \sum_{\eta''=\pm} \int d\mathbf{x}'' J^{(\eta'')}_\Theta(\mathbf{x}'') \frac{\partial_x \Theta^{(\eta'')}(\mathbf{x}'')}{\sqrt{\pi}} \\ &\quad - i\sqrt{4\pi}\left[\Phi_+^{(\eta_1)}(x_0,t_1) + \Phi_-^{(\eta_2)}(x_0,t_2) - \Phi^{(\eta_3)}(x_i,t_3)\right]\Bigg)\Bigg\}\Bigg\rangle_0 \Bigg|_{J_\Theta \equiv 0} \end{aligned} \tag{B.9}$$

correlates bosonic vertex operators. Also, we have introduced the notation $\mathbf{x} = (x, t)$. The expression (B.9) can straightforwardly be evaluated taking into account that for a functional

$$\zeta[J] = \left\langle T_{\rm K} \left\{ \exp\left(A + \sum_{\eta=\pm} \int d\mathbf{x} J^{(\eta)}(\mathbf{x}) B^{(\eta)}(\mathbf{x}) \right) \right\} \right\rangle_0 , \tag{B.10}$$

where A and B are linear combinations of bosonic operators, one has[4]

$$\left. \frac{\delta\zeta[J]}{\delta J^{(\eta)}(\mathbf{x})} \right|_{J=0} = \left\langle T_{\rm K} \left[A\, B^{(\eta)}(\mathbf{x}) \right] \right\rangle_0 \, \exp\left\{ \left\langle T_{\rm K} \left(A^2 \right) \right\rangle_0 \right\} . \tag{B.11}$$

Furthermore, it can be shown that $\mathcal{H}_{\mu_{\rm W}}$, *i.e.* the first term appearing in the exponent of Eq. (B.9), simply yields a shift in the operators $\Phi_\pm$ according to

$$\Phi_r^{(\eta)}(x,t) \to \Phi_r^{(\eta)}(x,t) + \Phi_{0,r}(x,t) \qquad r = \pm \quad , \tag{B.12}$$

where the zero modes

$$\Phi_{0,r}(x,t) = -\frac{1}{4\sqrt{\pi}} \frac{e\left[V_{\rm S} - V_{\rm D} + r(V_{\rm S} + V_{\rm D})\right]}{\hbar}\, t + \frac{e}{4\sqrt{\pi}\,\hbar v_{\rm W}} \tag{B.13}$$

$$\times \begin{cases} -(V_{\rm S} - V_{\rm D}) \left[(1-r)x + \dfrac{L}{2} \right] - g^2 (V_{\rm S} + V_{\rm D} - 2V_{\rm G}) \dfrac{L}{2} & \text{for } x \le -L/2 \\ \left[g^2 (V_{\rm S} + V_{\rm D} - 2V_{\rm G}) + r(V_{\rm S} - V_{\rm D}) \right] x & \text{for } |x| \le L/2 \\ (V_{\rm S} - V_{\rm D}) \left[(1+r)x - \dfrac{L}{2} \right] + g^2 (V_{\rm S} + V_{\rm D} - 2V_{\rm G}) \dfrac{L}{2} & \text{for } x \ge L/2 \end{cases}$$

fulfill the equation

$$\Phi_{0,r}(\mathbf{x}) - \Phi_{0,r}(\mathbf{y}) = \frac{-i}{\sqrt{\pi}\hbar} \int d\mathbf{x}'\, \mu_{\rm W}(\mathbf{x}') \, \left[\langle \Phi_r(\mathbf{x}) \partial_x \Phi(\mathbf{x}') \rangle^{\rm ret} - \langle \Phi_r(\mathbf{y}) \partial_x \Phi(\mathbf{x}') \rangle^{\rm ret} \right] . \tag{B.14}$$

After lengthy but straightforward algebra one obtains

$$\begin{aligned} &{\rm B}^{\eta_1\eta_2\eta_3}_{{\rm W},\gamma^2\lambda,i}(t_1,t_2,t_3) = \\ &= -2i\, e^{(ie/\hbar)\left[V_{\rm S}(t_1-t_3) - V_{\rm D}(t_2-t_3) - g^2(V_{\rm S}+V_{\rm D}-2V_{\rm G})(x_0-x_i)/v_{\rm W}\right]} \, b^{\eta_1\eta_2\eta_3}_{{\rm W},\gamma^2\lambda,i}(t_1-t_3, t_2-t_3) \\ &\quad \times \Big\{ \langle \partial_x\Theta(x,t)\Phi_+(x_0,t_1)\rangle_0^{\rm Kel} + \eta_1 \langle \partial_x\Theta(x,t)\Phi_+(x_0,t_1)\rangle_0^{\rm ret} \\ &\qquad + \langle \partial_x\Theta(x,t)\Phi_-(x_0,t_2)\rangle_0^{\rm Kel} + \eta_2 \langle \partial_x\Theta(x,t)\Phi_-(x_0,t_2)\rangle_0^{\rm ret} \\ &\qquad - \langle \partial_x\Theta(x,t)\Phi(x_i,t_3)\rangle_0^{\rm Kel} - \eta_3 \langle \partial_x\Theta(x,t)\Phi(x_i,t_2)\rangle_0^{\rm ret} \\ &\qquad + \frac{1}{\pi\hbar} \int d\mathbf{x}' \mu_{\rm W}(x') \langle T_{\rm K} \left[\partial_x\Theta(x,t) \partial_{x'}\Phi(\mathbf{x}') \right] \rangle_0^{\rm ret} \Big\} , \end{aligned} \tag{B.15}$$

where

$$
\begin{aligned}
& b^{\eta_1\eta_2\eta_3}_{\mathrm{W},\gamma^2\lambda,i}(t_1,t_2) \qquad\qquad\qquad\

where $\varphi(y)$ is a chiral (right-moving) boson field, and $\kappa_{\rm T}$ and $a_{\rm T}$ are the Klein factor and cutoff length of the tip, respectively. By way of example, we evaluate here the T-factor (A.13) appearing in the calculation of $I_{\gamma^2\lambda}$. Inserting Eqs. (B.21) and (B.22) into Eqs. (A.6) and (A.13), one obtains

$$\mathrm{T}^{\eta_1\eta_2}_{\gamma^2}(t_1-t_2) = \frac{1}{2\pi a_{\rm T}} \mathrm{F}^{\eta_1\eta_2}_{\rm T}(t_1-t_2)\, \mathrm{B}^{\eta_1\eta_2}_{{\rm T},\gamma^2}(t_1-t_2) \tag{B.23}$$

where, similar to the wire case,

$$\mathrm{F}^{\eta_1\eta_2}_{\rm T}(t_1-t_2) = \left\langle T_{\rm K}\left[\kappa^{(\eta_1)}_{\rm T}(t_1),\kappa^{(\eta_2)}(t_2)\right]\right\rangle_0 = -\eta_1\theta(t_2-t_1)+\eta_2\theta(t_1-t_2) \tag{B.24}$$

accounts for the correlation function of fermionic Klein factors, whereas the correlator of bosonic vertex operators reads

$$\begin{aligned}\mathrm{B}^{\eta_1\eta_2}_{{\rm T},\gamma^2}(t_1-t_2) &= \left\langle T_{\rm K}\left[\exp\left(-\frac{i}{\hbar}\sum_{\eta'=\pm}\eta'\int d\mathbf{y}'\mu_{\rm T}(y')\,\frac{\partial_{y'}\varphi(\mathbf{y}')}{\sqrt{\pi}}\right.\right.\right. \\ &\qquad \left.\left.\left. + i\sqrt{4\pi}\left[\varphi^{(\eta_1)}(0,t_1)-\varphi^{(\eta_2)}(0,t_2)\right]\right)\right]\right\rangle_0 .\end{aligned} \tag{B.25}$$

It is easily verified that the first term in the exponential function, which originates from the term (2.12) in the Hamiltonian, merely yields a time-dependent phase factor, so that

$$\mathrm{B}^{\eta_1\eta_2}_{{\rm T},\gamma^2}(t_1-t_2) = \mathrm{e}^{-(ie/\hbar)V_{\rm T}(t_1-t_2)}\, b^{\eta_1\eta_2}_{{\rm T},\gamma^2}(t_1-t_2) \tag{B.26}$$

where

$$\begin{aligned} b^{\eta_1\eta_2}_{{\rm T},\gamma^2}(t_1-t_2) &= \exp\left\{-2\pi\left\langle T_{\rm K}\left[\left(\varphi^{(\eta_1)}(0,t_1)-\varphi^{(\eta_2)}(0,t_2)\right)^2\right]\right\rangle_0\right\} \\ &= \exp\left\{4\pi\left[\mathcal{R}_{\rm T}(\tau_1-\tau_2) + i\,\mathcal{I}^{\eta_1\eta_2}_{\rm T}(\tau_1-\tau_2)\right]\right\} . \end{aligned} \tag{B.27}$$

The functions $\mathcal{R}_{\rm T}(\tau)$ and $\mathcal{I}^{\eta_1\eta_2}_{\rm T}(\tau)$ are given in App. C, see Eqs. (C.11) and (C.12).

Appendix C

Correlation functions

This appendix collects properties of correlation functions appearing in Eqs. (2.60) and (2.69), as well as in Eqs. (B.16) and (B.27). The transport properties of the wire are expressed in terms of the functions

$$\begin{aligned}\mathcal{R}_{\rm W}(\xi_0;\xi_i;\tau_1;\tau_2) =& \mathcal{R}_{\rm reg}^{\Phi_+\Phi_+}(\xi_0;\xi_i;\tau_1) + \mathcal{R}_{\rm reg}^{\Phi_-\Phi_-}(\xi_0;\xi_i;\tau_2) \\ &+ \mathcal{R}^{\Phi_+\Phi_-}(\xi_0;\xi_i;\tau_1) + \mathcal{R}^{\Phi_-\Phi_+}(\xi_0;\xi_i;\tau_2) \\ &- \mathcal{R}^{\Phi_+\Phi_-}(\xi_0;\xi_0;\tau_1-\tau_2) - \mathcal{R}^{\Phi_-\Phi_+}(\xi_i;\xi_i;0) \end{aligned} \tag{C.1}$$

$$\begin{aligned}\mathcal{I}_{\rm W}^{\eta_1\eta_2\eta_3}(\xi_0;\xi_i;\tau_1;\tau_2) =& \sum_{r=\pm}\Big\{\left[\eta_3\theta(\tau_1)-\eta_1\theta(-\tau_1)\right]\mathcal{I}^{\Phi_+\Phi_r}(\xi_0;\xi_i;\tau_1) \\ &+ \left[\eta_3\theta(\tau_2)-\eta_2\theta(-\tau_2)\right]\mathcal{I}^{\Phi_-\Phi_r}(\xi_0;\xi_i;\tau_2)\Big\} \\ &- \left[\eta_2\theta(\tau_1-\tau_2)-\eta_1\theta(\tau_2-\tau_1)\right]\mathcal{I}^{\Phi_+\Phi_-}(\xi_0;\xi_0;\tau_1-\tau_2)\,. \end{aligned} \tag{C.2}$$

where the functions $\mathcal{R}_{\rm reg}^{\Phi_r\Phi_r}(\xi;\xi';\tau)$ and $\mathcal{I}^{\Phi_r\Phi_r}(\xi;\xi';\tau)$ are the real and imaginary parts, respectively, of the auto-correlation functions of the bosonic fields Φ_r. Specifically

$$\mathcal{R}_{\rm reg}^{\Phi_r\Phi_r}(\xi;\xi';\tau) = \Re\left\{\left\langle \Phi_r(x,t)\Phi_r(x',0) - \frac{1}{2}\left[\Phi_r^2(x,t)+\Phi_r^2(x',0)\right]\right\rangle_0\right\} \tag{C.3}$$

$$\mathcal{I}^{\Phi_r\Phi_r}(\xi;\xi';\tau) = \Im\left\{\langle\Phi_r(x,t)\Phi_r(x',0)\rangle_0\right\} \tag{C.4}$$

Likewise, the real and imaginary parts of the cross-correlation functions of fields with different chirality r read

$$\mathcal{R}^{\Phi_r\Phi_{-r}}(\xi;\xi';\tau) = \Re\left\{\langle\Phi_r(x,t)\Phi_{-r}(y,0)\rangle_0\right\} \tag{C.5}$$

$$\mathcal{I}^{\Phi_r\Phi_{-r}}(\xi;\xi';\tau) = \Im\left\{\langle\Phi_r(x,t)\Phi_{-r}(y,0)\rangle_0\right\} \tag{C.6}$$

Notice that the real part of the correlation functions of fields with the same chirality needs to be defined with an infrared regularization as in Eq. (C.3).

The above equations are given in terms of the dimensionless time and space variables $\tau = tv_{\mathrm{W}}/gL$ and $\xi = x/L$ introduced previously. From the inhomogeneous Luttinger liquid model one obtains at zero temperature:

$$
\begin{aligned}
\mathcal{R}^{\Phi_r\Phi_r}_{\rm reg}(\xi,\xi',\tau) \;=\; & -\frac{1}{32\pi}\Bigg\{\big(g+g^{-1}-2r\big)\sum_{m\in Z_{\rm even}}\rho^{|m|}\ln\frac{\alpha_{\rm W}^2+(\tau+\xi_r+m)^2}{\alpha_{\rm W}^2+m^2} \\
& +\big(g+g^{-1}+2r\big)\sum_{m\in Z_{\rm even}}\rho^{|m|}\ln\frac{\alpha_{\rm W}^2+(\tau-\xi_r-m)^2}{\alpha_{\rm W}^2+m^2} \\
& +\big(g-g^{-1}\big)\sum_{m\in Z_{\rm odd}}\rho^{|m|}\Bigg(\ln\frac{\alpha_{\rm W}^2+(\tau+\xi_R+m)^2}{\alpha_{\rm W}^2+(\xi_R+m)^2}+\ln\frac{\alpha_{\rm W}^2+(\tau-\xi_R-m)^2}{\alpha_{\rm W}^2+(\xi_R+m)^2} \\
& \qquad +\ln\frac{[\alpha_{\rm W}^2+(\xi_R+m)^2]^2}{[\alpha_{\rm W}^2+(2\xi+m)^2][\alpha_{\rm W}^2+(2\xi'+m)^2]}\Bigg)\Bigg\}
\end{aligned}
\tag{C.7}
$$

$$
\begin{aligned}
\mathcal{I}^{\Phi_r\Phi_r}(\xi,\xi',\tau) \;=\; & -\frac{1}{16\pi}\Bigg\{\big(g+g^{-1}-2r\big)\sum_{m\in Z_{\rm even}}\rho^{|m|}\arctan\left(\frac{\tau+\xi_r+m}{\alpha_{\rm W}}\right) \\
& +\big(g+g^{-1}+2r\big)\sum_{m\in Z_{\rm even}}\rho^{|m|}\arctan\left(\frac{\tau-\xi_r-m}{\alpha_{\rm W}}\right) \\
& +\big(g-g^{-1}\big)\sum_{m\in Z_{\rm odd}}\rho^{|m|}\left[\arctan\left(\frac{\tau+\xi_R+m}{\alpha_{\rm W}}\right)+\arctan\left(\frac{\tau-\xi_R-m}{\alpha_{\rm W}}\right)\right]\Bigg\}
\end{aligned}
\tag{C.8}
$$

and

$$\begin{aligned}
\mathcal{R}^{\Phi_r\Phi_{-r}}(\xi;\xi';\tau) &= -\frac{1}{32\pi}\Bigg\{\left(g-g^{-1}\right)\sum_{m\in Z_{\rm even}}\rho^{|m|}\left[\ln\left(\frac{\alpha_{\rm W}^2+(\tau+\xi_r+m)^2}{\alpha_{\rm W}^2+m^2}\right)+\ln\left(\frac{\alpha_{\rm W}^2+(\tau-\xi_r-m)^2}{\alpha_{\rm W}^2+m^2}\right)\right] \\
&\quad+\left(g+g^{-1}-2r\right)\sum_{m\in Z_{\rm odd}}\rho^{|m|}\ln\left(\frac{\alpha_{\rm W}^2+(\tau+\xi_R+m)^2}{\alpha_{\rm W}^2+(\xi_R+m)^2}\right) \\
&\quad+\left(g+g^{-1}+2r\right)\sum_{m\in Z_{\rm odd}}\rho^{|m|}\ln\left(\frac{\alpha_{\rm W}^2+(\tau-\xi_R-m)^2}{\alpha_{\rm W}^2+(\xi_R+m)^2}\right) \\
&\quad+\left(g+g^{-1}\right)\sum_{m\in Z_{\rm odd}}\rho^{|m|}\ln\frac{\left[\alpha_{\rm W}^2+(\xi_R+m)^2\right]^2}{[\alpha_{\rm W}^2+(2\xi+m)^2][\alpha_{\rm W}^2+(2\xi'+m)^2]} \\
&\quad-\frac{1}{2}\left(g-g^{-1}\right)\sum_{m\in Z_{\rm even}}\rho^{|m|}\left[\ln\left(\frac{[\alpha_{\rm W}^2+(2\xi+1+m)^2][\alpha_{\rm W}^2+(2\xi'+1+m)^2]}{(\alpha_{\rm W}^2+m^2)^2}\right)\right. \\
&\qquad\left.+\ln\left(\frac{[\alpha_{\rm W}^2+(2\xi-1+m)^2][\alpha_{\rm W}^2+(2\xi'-1+m)^2]}{(\alpha_{\rm W}^2+m^2)^2}\right)\right]\Bigg\}
\end{aligned} \tag{C.9}$$

and

$$\begin{aligned}
\mathcal{I}^{\Phi_r\Phi_{-r}}(\xi;\xi';\tau) &= -\frac{1}{16\pi}\Bigg\{\left(g-g^{-1}\right)\sum_{m\in Z_{\rm even}}\rho^{|m|}\left[\arctan\left(\frac{\tau+\xi_r+m}{\alpha_{\rm W}}\right)+\arctan\left(\frac{\tau-\xi_r-m}{\alpha_{\rm W}}\right)\right] \\
&\quad+\left(g+g^{-1}-2r\right)\sum_{m\in Z_{\rm odd}}\rho^{|m|}\arctan\left(\frac{\tau+\xi_R+m}{\alpha_{\rm W}}\right) \\
&\quad+\left(g+g^{-1}+2r\right)\sum_{m\in Z_{\rm odd}}\rho^{|m|}\arctan\left(\frac{\tau-\xi_R-m}{\alpha_{\rm W}}\right)\Bigg\}\,.
\end{aligned} \tag{C.10}$$

Here we have introduced $\xi_r = \xi - \xi'$, $\xi_R = \xi + \xi'$, and the dimensionless cutoff length $\alpha_{\mathrm{W}} = a_{\mathrm{W}}/gL$, as well as the Andreev-type reflection coefficient $\rho = (1-g)/(1+g)$.

The correlation functions for the non-interacting tip can directly be obtained from the above results. The tip is described by a single chiral mode, and we need the correlation function only for coordinates at the injection point $y = 0$. From Eqs. (C.7) and (C.8) we find for $\xi = \xi' = 0$ by taking the limit $g \to 1$ and replacing α_{W} by α_{T}

$$\mathcal{R}_{\mathrm{T}}(\tau) = \mathcal{R}^{\varphi\varphi}_{\mathrm{reg}}(0;0;\tau) = \mathcal{R}^{\Phi_+\Phi_+}_{\mathrm{reg}}(0;0;\tau)\Big|_{\substack{g\to 1\\ \alpha_{\mathrm{W}}\to\alpha_{\mathrm{T}}}} = -\frac{1}{8\pi}\ln\frac{\alpha_{\mathrm{T}}^2+\tau^2}{\alpha_{\mathrm{T}}^2} \tag{C.11}$$

$$\begin{aligned}\mathcal{I}^{\eta_1\eta_2}_{\mathrm{T}}(\tau) &= \mathrm{F}^{\eta_1\eta_2}_{\mathrm{T}}(\tau)\,\mathcal{I}^{\varphi\varphi}(0;0;\tau) = \mathrm{F}^{\eta_1\eta_2}_{\mathrm{T}}(\tau)\,\mathcal{I}^{\Phi_+\Phi_+}(0;0;\tau)\Big|_{\substack{g\to 1\\ \alpha_{\mathrm{W}}\to\alpha_{\mathrm{T}}}} \\ &= -\frac{\eta_2\theta(\tau)-\eta_1\theta(-\tau)}{4\pi}\arctan\left(\frac{\tau}{\alpha_{\mathrm{T}}}\right).\end{aligned} \tag{C.12}$$

Appendix D

Superconducting Quantum Interference Devices

Quantum interference in superconductors is the basic working principle of a widely used type of devices that go under the name of *Superconducting Quantum Interference Devices*, or SQUIDs. These are loops of a superconducting material interrupted by one or more Josephson junctions and connected to an external circuit. Taking the line integral of the gradient of the complex phase φ of the superconducting order parameter must yield an integer multiple of 2π, for the order parameter to be a single-valued complex function throughout the superconductor. However in principle phase drops can occur at each of the Josephson junctions and in this case a supercurrent flows through them, according to the first Josephson relation $I_s = I_c \sin \Delta\varphi$. The supercurrent is a gauge-invariant quantity, whereas the complex phase of the order parameter changes under a gauge transformation $\boldsymbol{A} \to \boldsymbol{A} + \boldsymbol{\nabla}\Lambda$ ($\boldsymbol{A}$ is the vector potential of the magnetic field and Λ is a real function) in the same way as the phase of a wave function of a particle of charge $2e$: $\varphi \to \varphi - (2e/\hbar)\Lambda(x)$; therefore the supercurrent through the Josephson junction must depend not only on the difference in the complex phase of the order parameter, but on a gauge-invariant quantity called the gauge-invariant phase:

$$\gamma = \varphi + \frac{2e}{\hbar} \int \boldsymbol{A} \cdot \boldsymbol{dl} \tag{D.1}$$

The fact that the order parameter is single-valued results in a condition on the total gauge-invariant phase drop:

$$\Delta\gamma_1 + \ldots + \Delta\gamma_n = \Delta\varphi_{\text{tot}} + \frac{2e}{\hbar} \int_{\text{loop}} \boldsymbol{A} \cdot \boldsymbol{dl} = 2k\pi + 2\pi \frac{2e}{h} \Phi \simeq 2\pi \frac{2e\Phi}{h} \tag{D.2}$$

where $\Delta\gamma_i$ is the gauge-invariant phase drop across the i-th Josephson junction and Φ is the total magnetic flux threading the loop.

It is clear that the dynamics of the phase drop across the SQUID loop is strictly connected with the value of the total magnetic flux Φ. If a part of the superconducting loop is free to oscillate in the presence of a static magnetic field, then the area of the loop, and hence the magnetic flux Φ, depends on the position of the geometric center of the oscillating arm; this can be used to couple the dynamics of the mechanical and electrical degrees of freedom.

However SQUIDs are well known to be excellent detectors of magnetic flux. The reason can be understood from Eq. (D.2): since all the phases are defined up to integer multiples of 2π, we can expect that many dynamical quantities be periodic with respect to the magnetic flux with period

$$\Phi_0 = \frac{h}{2e} \tag{D.3}$$

Since this is a very small flux (called the *flux quantum*), SQUIDs have been proposed as a basis for a metrological standard; in fact they have provided us with the most accurate measurement of the ratio e/h.

Conclusions

In the first part of our work we have addressed the study of transport in an interacting quantum wire. The interaction has been taken into account within the inhomogeneous Luttinger liquid model. It is known that for a clean interacting wire the conductance is the same as for a non-interacting one. However, if impurities are present, the differential conductance exhibits fluctuations as a function of the bias voltage. These fluctuations have been shown to be a consequence of a partial reflection of the charge density at the contact between the leads and the wire (Andreev-type reflections). In realistic wires, the contacts may introduce some backscattering in a similar fashion as an isolated would impurity. It is therefore interesting to study the conductance of an interacting quantum wire in the presence of contact impurities in order to see the effect of interaction. For this kind of device, however, the differential conductance is expected to already show Fabry-Pérot oscillations for a non-interacting wire. In order to distinguish between oscillations due to Andreev-type reflections and Fabry-Pérot oscillations, we have proposed a three-terminal setup comprised of a quantum nanowire and a tunneling tip facing it as a third terminal. We showed that this third terminal produces a modulation in the oscillating differential conductance, typical of Fabry-Pérot intereference, and that such modulation can be interpreted as a peculiar effect of the interaction via the inhomogeneous-Luttinger-liquid model. We have further taken into consideration the possibility of a selective injection of electrons through the third terminal, since asymmetric current injection has been recently realized for a very similar setup. Our analysis allows us to exploit asymmetric tunneling to measure the phenomenological parameters that characterize the setup, thus allowing for a full account of the measurements.

The second part of our work begins with the study of the coupled dynamics of a SQUID and a mechanical degree of freedom representing the motion of a suspended arm of the SQUID itself: since the oscillations modify the total area of the loop, a constant magnetic field perpendicular to the plane of the oscillations can be used to modify the total magnetic flux through the

SQUID in accordance with the oscillator's position. We have focused on two different regimes, namely the classical and the quantum regime. The study of a classical SQUID NEMS has revealed that the highly nonlinear current-voltage relation due to the physics of Josephson junctions can be used to extract some useful information about the mechanical oscillator. Indeed the electromotive force induced by the oscillations produces step-like features in the I-V curve of the SQUID, similar to what happens in ac-driven Josephson junctions (the so-called *Shapiro's steps*). What is relevant in this fact is that the height of the steps depends only the oscillator frequency and not on the amplitude of the oscillations; this is important, because such amplitude is usually very small. We also studied the interplay between the signal induced by the motion of the suspended arm and a further ac signal flowing through the SQUID, and we found that by this means the width of the steps can be enhanced. We investigated the effect of thermal noise on the efficiency of this characterization scheme and found that it can be detrimental. In view of an experimental demonstration of coherent coupled dynamics in this device, we have also performed a preliminary study of the quantum regime of a SQUID NEMS. We have focused our attention on the feasibility of detection based on standard spectroscopic techniques applied to quantum SQUIDs (such as phase and flux qubits); with these techniques it is possible to detect small changes in the energy spectrum of quantum SQUIDS and, in principle, a mechanical degree of freedom coupled to the SQUID should be detectable by a change in the spectrum. This change, however, is of at least second order in the small coupling unless the proper frequencies of the resonator and of the quantum SQUID are brought into resonance. Our study shows that this can be achieved by appropriately tuning the control parameters of the SQUID, taking into consideration the dissipation in both the mechanical oscillator and in the SQUID. Finally, we studied a feasible scheme to demonstrate phonon blockade in a non-linear mechanical resonator by coupling it to a superconducting microwave cavity. The idea is to couple the (conducting) mechanical oscillator capacitively to the central conductor of the superconducting cavity, while keeping the oscillator at a finite voltage difference with respect to ground: this produces an effective linear coupling between the mechanical degree of freedom and the electrical degree of freedom of the cavity. In the regime of resonant coupling, the first two excited states of the system are a doublet of Bell states entangling the state with one phonon and no photon with the state with no phonon and one photon. Due to the non-linearity of the mechanical oscillator, states with a higher number of excitations have different energy spacing with respect to the energy of the first excitation; because of this, applying a drive which is resonant with the first transition results in the generation of no more than one phonon. We

showed that this behavior can be detected by measuring the two-particle time correlation function of the electromagnetic field in the microwave cavity, in the same way as has recently been demonstrated; the reason is that in the Bell states there is perfect correlation between the number of photons and the number of phonons. We also showed that the finite quality factor of the oscillator or of the cavity or the noise introduced by the gate voltage is not detrimental for this scheme.

List of publications

S. Pugnetti, F. Dolcini, D. Bercioux and H. Grabert, Phys. Rev. B **79**, 035121 (2009);

S. Pugnetti, Ya. M. Blanter, F. Dolcini and R. Fazio, Phys. Rev. B **79**, 174516(2009);

S. Pugnetti, Ya. M. Blanter and R. Fazio, Europhys. Lett. **90**, 48007 (2010).

N. Didier, S. Pugnetti, Ya. M. Blanter and R. Fazio, arXiv:1007.4714 (2010).

Acknowledgements

Several people deserve acknowledgment, as their contribution, both on the scientific and the human side, has been of the greatest importance to the realization of this work.

The very fact that this thesis has been produced and delivered is due to the constant support, encouragement and drive that my PhD advisor, prof. Rosario Fazio, has given me during the last four years. There would likely be no need to mention my feelings of gratitude towards him for this, for the invaluable scientific experience that working with him and with his group has provided me and for all that I have learned; all the same, I yet feel the urge to write this down.

In addition, my collaboration with Dr. Fabrizio Dolcini has also been substantial. The long and frequent discussions both about the physics of the setups we were studying and about the way to present it have been very instructing and stimulating. Moreover, much of the work developed in the first part of this thesis has its roots located deep within his previous works.

The first part of this thesis has also greatly benefited from scientific discussions with prof. Hermann Grabert, whose vast experience and deep physical insight have often been enlightening. Dr. Dario Bercioux has also largely contributed to this part, double-checking the analytical results for the non-interacting case and taking care of the numerics.

The second part of this work was developed in collaboration with prof. Yaroslav M. Blanter, partly during a two-month visit to the Theoretical Physics group at the Delft University of Technology, whose kind hospitality I would like to acknowledge. The opportunity to work with prof. Blanter has been very important for my scientific education. This visit was also an opportunity to interact with the experimental group of prof. Herre van der Zant, where I learned much about experimental issues related to the setups we have been studying; discussions with Menno Poot, Samir Etaki, Harold Meerwaldt and Ben Schneider are gratefully acknowledged. The useful stay in Delft was made also very pleasant by the cheerful company of Giorgi, Chris, Stefan, Jeroen, Marnix and Fabian.

The work presented in chapter 6 was done in collaboration with Dr. Nicolas Didier, who did the numerics and some analytical calculations.

Finally, Kyle Hall has kindly accepted to proof-read the manuscript and has provided a very useful contribution to the readability of the text.

Bibliography

[1] S. Datta. *Electronic Transport in Mesoscopic Systems* (1995).

[2] M. Bockrath, D. H. Cobden, J. Lu, A. G. Rinzler, R. E. Smalley, L. Balents and P. L. McEuen, *Nature* **397**, 598 (1999).

[3] J. von Delft and H. Schoeller, *Ann. der Phys.* **7**, 225 (1998).

[4] A. O. Gogolin, A. A. Nersesyan and A. M. Tsvelik. *Bosonization and Strongly Correlated Systems* (1998).

[5] G. D. Mahan. *Many-Particle Physics* (1990).

[6] S. Tarucha, T. Honda and T. Saku, *Solid State Commun.* **94**, 413 (1995).

[7] I. Safi and H. J. Schulz, *Phys. Rev. B* **52**, R17040 (1995).

[8] D. L. Maslov and M. Stone, *Phys. Rev. B* **52**, R5539 (1995).

[9] V. V. Ponomarenko, *Phys. Rev. B* **52**, R8666 (1995).

[10] F. Dolcini, H. Grabert, I. Safi and B. Trauzettel, *Phys. Rev. Lett.* **91**, 266402 (2003).

[11] Z. Zhang and C. M. Lieber, *Applied Physics Letters* **62**, 2792 (1993).

[12] J. W. G. Wilder, L. C. Venema, A. G. Rinzler, R. E. Smalley and C. Dekker, *Nature* **391**, 59 (1998).

[13] T. W. Odom, J.-L. Huang, P. Kim and C. M. Lieber, *Nature* **391**, 62 (1998).

[14] M. A. Topinka, B. J. LeRoy, S. E. J. Shaw, E. J. Heller, R. M. Westervelt, K. D. Maranowski and A. C. Gossard, *Science* **289**, 2323 (2000). http://www.sciencemag.org/cgi/reprint/289/5488/2323.pdf.

[15] B. J. LeRoy, I. Heller, V. K. Pahilwani, C. Dekker and S. G. Lemay, *Nano Letters* **7**, 2937 (2007).

[16] A. Yazdani, B. A. Jones, C. P. Lutz, M. F. Crommie and D. M. Eigler, *Science* **275**, 1767 (1997). http://www.sciencemag.org/cgi/reprint/275/5307/1767.pdf.

[17] S. H. Pan, E. W. Hudson and J. C. Davis, *Applied Physics Letters* **73**, 2992 (1998).

[18] T. Proslier, A. Kohen, Y. Noat, T. Cren, D. Roditchev and W. Sacks, *EPL (Europhysics Letters)* **73**, 962 (2006).

[19] A. Kohen, T. Proslier, T. Cren, Y. Noat, W. Sacks, H. Berger and D. Roditchev, *Phys. Rev. Lett.* **97**, 027001 (2006).

[20] B. J. van Wees, K.-M. H. Lenssen and C. J. P. M. Harmans, *Phys. Rev. B* **44**, 470 (1991).

[21] A. F. Volkov, *Phys. Rev. Lett.* **74**, 4730 (1995).

[22] F. K. Wilhelm, G. Schön and A. D. Zaikin, *Phys. Rev. Lett.* **81**, 1682 (1998).

[23] J. J. A. Baselmans, A. F. Morpurgo, B. J. van Wees and T. M. Klapwijk, *Nature* **397**, 43 (1999).

[24] P. Samuelsson, J. Lantz, V. S. Shumeiko and G. Wendin, *Phys. Rev. B* **62**, 1319 (2000).

[25] F. Giazotto, T. T. Heikkilä, A. Luukanen, A. M. Savin and J. P. Pekola, *Rev. Mod. Phys.* **78**, 217 (2006).

[26] M. T. Woodside and P. L. McEuen, *Science* **296**, 1098 (2002). http://www.sciencemag.org/cgi/reprint/296/5570/1098.pdf.

[27] A. Naik, O.Buu, M. D. LaHaye, A. D. Armour, A. A. Clerk, M. P. Blencowe and K. C. Schwab, *Nature* **443**, 193 (2006).

[28] R. Ruskov, K. Schwab and A. N. Korotkov, *Phys. Rev. B* **71**, 235407 (2005).

[29] M. Büttiker, Y. Imry and M. Y. Azbel, *Phys. Rev. A* **30**, 1982 (1984).

[30] F. Marquardt and C. Bruder, *Phys. Rev. B* **70**, 125305 (2004).

[31] F. Marquardt, *Phys. Rev. B* **74**, 125319 (2006).

[32] C. Texier and M. Büttiker, *Phys. Rev. B* **62**, 7454 (2000).

[33] S. Pilgram, P. Samuelsson, H. Förster and M. Büttiker, *Phys. Rev. Lett.* **97**, 066801 (2006).

[34] H. Förster, P. Samuelsson and M. Bttiker, *New Journal of Physics* **9**, 117 (2007).

[35] A. Yacoby, H. L. Stormer, K. W. Baldwin, L. N. Pfeiffer and K. W. West, *Solid State Communications* **101**, 77 (1997).

[36] R. de Picciotto, H. L. Stormer, L. N. Pfeiffer, K. W. Baldwin and K. W. West, *Nature* **411**, 51 (2001).

[37] C. T. White and T. N. Todorov, *Nature* **393**, 240 (1998).

[38] W. Liang, M. Bockrath, D. Bozovic, J. H. Hafner, M. Tinkham and H. Park, *Nature* **411**, 665 (2001).

[39] A. Yacoby, H. L. Stormer, N. S. Wingreen, L. N. Pfeiffer, K. W. Baldwin and K. W. West, *Phys. Rev. Lett.* **77**, 4612 (1996).

[40] O. M. Auslaender, A. Yacoby, R. de Picciotto, K. W. Baldwin, L. N. Pfeiffer and K. W. West, *Phys. Rev. Lett.* **84**, 1764 (2000).

[41] O. M. Auslaender, H. Steinberg, A. Yacoby, Y. Tserkovnyak, B. I. Halperin, K. W. Baldwin, L. N. Pfeiffer and K. W. West, *Science* **308**, 88 (2005). `http://www.sciencemag.org/cgi/reprint/308/5718/88.pdf`.

[42] H. Steinberg, O. M. Auslaender, A. Yacoby, J. Qian, G. A. Fiete, Y. Tserkovnyak, B. I. Halperin, K. W. Baldwin, L. N. Pfeiffer and K. W. West, *Phys. Rev. B* **73**, 113307 (2006).

[43] Z. Yao, H. W. C. Postma, L. Balents and C. Dekker, *Nature* **402**, 273 (1999).

[44] N. Y. Kim, P. Recher, W. D. Oliver, Y. Yamamoto, J. Kong and H. Dai, *Phys. Rev. Lett.* **99**, 036802 (2007).

[45] S. Eggert, *Phys. Rev. Lett.* **84**, 4413 (2000).

[46] I. Ussishkin and L. I. Glazman, *Phys. Rev. Lett.* **93**, 196403 (2004).

[47] A. Crépieux, R. Guyon, P. Devillard and T. Martin, *Phys. Rev. B* **67**, 205408 (2003).

[48] A. V. Lebedev, A. Crépieux and T. Martin, *Phys. Rev. B* **71**, 075416 (2005).

[49] F. Wu, P. Queipo, A. Nasibulin, T. Tsuneta, T. H. Wang, E. Kauppinen and P. J. Hakonen, *Phys. Rev. Lett.* **99**, 156803 (2007).

[50] L. G. Herrmann, T. Delattre, P. Morfin, J.-M. Berroir, B. Plaçais, D. C. Glattli and T. Kontos, *Phys. Rev. Lett.* **99**, 156804 (2007).

[51] H. Steinberg, G. Barak, A. Yacoby, L. N. Pfeiffer, K. W. West, B. I. Halperin and K. Le Hur, *Nat Phys* **4**, 116 (2008).

[52] C. S. Peça, L. Balents and K. J. Wiese, *Phys. Rev. B* **68**, 205423 (2003).

[53] P. Recher, N. Y. Kim and Y. Yamamoto, *Phys. Rev. B* **74**, 235438 (2006).

[54] K. L. Hur, B. I. Halperin and A. Yacoby, *Annals of Physics* **323**, 3037 (2008).

[55] M. Buttiker, *Journal of Physics: Condensed Matter* **5**, 9361 (1993).

[56] L. V. Keldysh, *Zh. Eksp. Teor. Fiz.* **47**, 1515 (1964).

[57] F. Dolcini, B. Trauzettel, I. Safi and H. Grabert, *Phys. Rev. B* **71**, 165309 (2005).

[58] P. Fendley, A. W. W. Ludwig and H. Saleur, *Phys. Rev. B* **52**, 8934 (1995).

[59] R. Egger and H. Grabert, *Phys. Rev. Lett.* **79**, 3463 (1997).

[60] I. Safi, *Ann. Phys. Fr.* **22**, 463 (1997).

[61] K.-V. Pham, M. Gabay and P. Lederer, *Phys. Rev. B* **61**, 16397 (2000).

[62] K.-I. Imura, K.-V. Pham, P. Lederer and F. Piéchon, *Phys. Rev. B* **66**, 035313 (2002).

[63] K. Le Hur, *Phys. Rev. Lett.* **95**, 076801 (2005).

[64] M. Fisher and L. Glazman. *Mesoscopic Electron Transport*, volume E345 of *NATO ASI Series*. Sohn,L.L. and Kouwenhoven, L.P. and Schön, G. (1997).

[65] Y. V. Nazarov, A. A. Odintsov and D. V. Averin, *EPL (Europhysics Letters)* **37**, 213 (1997).

[66] R. E. Slusher, L. W. Hollberg, B. Yurke, J. C. Mertz and J. F. Valley, *Phys. Rev. Lett.* **55**, 2409 (1985).

[67] E. Waks, E. Diamanti and Y. Yamamoto, *New Journal of Physics* **8**, 4 (2006).

[68] M. Hofheinz, H. Wang, M. Ansmann, R. C. Bialczak, E. Lucero, M. Neeley, A. D. O'Connell, D. Sank, J. Wenner, J. M. Martinis and A. N. Cleland, *Nature* **459**, 546 (2009).

[69] A. D. O'Connell, M. Hofheinz, M. Ansmann, R. C. Bialczak, M. Lenander, E. Lucero, M. Neeley, D. Sank, H. Wang, M. Weides, J. Wenner, J. M. Martinis and A. N. Cleland, *Nature* **464**, 697 (2010).

[70] C. M. Caves, *Phys. Rev. Lett.* **54**, 2465 (1985).

[71] C. M. Caves, K. S. Thorne, R. W. P. Drever, V. D. Sandberg and M. Zimmermann, *Rev. Mod. Phys.* **52**, 341 (1980).

[72] B. Abbott and et al, *New J. Phys.* **11**, 072032 (2009).

[73] Y. Hadjard, P. F.Cohadon, C. G. Aminoff, M. Pinard and A. Heidmann, *Europhys. Lett.* **47**, 545 (1999).

[74] C. Höhberger Metzger and K. Karrai, *Nature* **432**, 1002 (2004).

[75] O. Arcizet, P.-F. Cohadon, T. Briant, M. Pinard and A. Heidmann, *Nature* **444**, 71 (2006).

[76] M. W. Pruessner, T. H. Stievater and W. S. Rabinovich, *App. Phys. Lett.* **92**, 081101 (2008).

[77] I. Favero, C. Metzger, S. Camerer, D. König, H. Lorenz, J. P. Kotthaus and K. Karrai, *App. Phys. Lett.* **90**, 104101 (2007).

[78] G. Anetsberger, O. Arcizet, Q. P. Unterreithmeier, R. Riviere, A. Schliesser, E. M. Weig, J. P. Kotthaus and T. J. Kippenberg, *Nat Phys* **5**, 909 (2009).

[79] J. Yao, S. Arney and N. MacDonald, *Microelectromech. Sys* **1**, 14 (1992).

[80] A. N. Cleland and M. L. Roukes, *Applied Physics Letters* **69**, 2653 (1996).

[81] A. A. Clerk, M. H. Devoret, S. M. Girvin, F. Marquardt and R. J. Schoelkopf, *Rev. Mod. Phys.* **82**, 1155 (2010).

[82] J. D. White, *Jpn. J. Appl. Phys.* **32**, L1571 (1993).

[83] R. G. Knobel and A. N. Cleland, *Nature* **424**, 291 (2003).

[84] M. D. LaHaye, O.Buu, B. Camarota and K. C. Schwab, *Science* **304**, 74 (2004).

[85] J. M. Martinis, M. H. Devoret and J. Clarke, *Phys. Rev. B* **35**, 4682 (1987).

[86] E. Buks and M. P. Blencowe, *Phys. Rev. B* **74**, 174504 (2006).

[87] X. Zhou and A. Mizel, *Phys. Rev. Lett.* **97**, 267201 (2006).

[88] F. Xue, Y. X. Liu, C. P. Sun and F. Nori, *Phys. Rev. B* **76**, 064305 (2007).

[89] M. P. Blencowe and E. Buks, *Phys. Rev. B* **76**, 014511 (2007).

[90] Y.-D. Wang, K. Semba and H. Yamaguchi, *New J. Phys.* **10**, 043015 (2008).

[91] S. Etaki, M. Poot, I. Mahboob, K. Onomitsu, H. Yamaguchi and H. S. J. van der Zant, *Nat. Phys.* **4**, 785 (2008).

[92] P. Reimann, *Phys. Rep.* **361**, 57 (2002).

[93] I. Zapata, R. Bartussek, F. Sols and P. Hänggi, *Phys. Rev. Lett.* **77**, 2292 (1996).

[94] X. M. H. Huang, C. A. Zorman, M. Mehregany and M. L. Roukes, *Nature* **421**, 496 (2003).

[95] S. Sapmaz, Y. M. Blanter, L. Gurevich and H. S. J. van der Zant, *Phys. Rev. B* **67**, 235414 (2003).

[96] A. N. Cleland and M. R. Geller, *Phys. Rev. Lett.* **93**, 070501 (2004).

[97] A. D. Armour, M. P. Blencowe and K. C. Schwab, *Phys. Rev. Lett.* **88**, 148301 (2002).

[98] I. Martin, A. Shnirman, L. Tian and P. Zoller, *Phys. Rev. B* **69**, 125339 (2004).

[99] P. Rabl, A. Shnirman and P. Zoller, *Phys. Rev. B* **70**, 205304 (2004).

[100] L. F. Wei, Y. xi Liu, C. P. Sun and F. Nori, *Phys. Rev. Lett.* **97**, 237201 (2006).

[101] A. D. Armour and M. P. Blencowe, *New J. Phys.* **10**, 095004 (25pp) (2008).

[102] J. Hauss, A. Fedorov, S. André, V. Brosco, C. Hutter, R. Kothari, S. Yeshwanth, A. Shnirman and G. Schön, *New Journal of Physics* **10**, 095018 (17pp) (2008).

[103] B. R. Trees, Y. H. Helal, J. S. Schiffrin and B. M. Siller, *Phys. Rev. B* **76**, 224513 (2007).

[104] J. Q. Liao and L. M. Kuang, *Eur. Phys. J. B* **63**, 79 (2008).

[105] M. D. LaHaye, J. Suh, P. M. Echternach, K. C. Schwab and M. L. Roukes, *Nature* **459**, 960 (2009).

[106] X. Zhou and A. Mizel, *Phys. Rev. Lett.* **97**, 267201 (2006).

[107] J. Zhang, Y. xi Liu and F. Nori, *Phys. Rev. A* **79**, 052102 (2009).

[108] J. E. Mooij, T. P. Orlando, L. Levitov, L. Tian, C. H. van der Wal and S. Lloyd, *Science* **285**, 1036 (1999). http://www.sciencemag.org/cgi/reprint/285/5430/1036.pdf.

[109] I. Schuster, A. Kubanek, A. Fuhrmanek, T. Puppe, P. W. H. Pinkse, K. Murr and G. Rempe, *Nat Phys* **4**, 382 (2008).

[110] J. M. Fink, M. Goppl, M. Baur, R. Bianchetti, P. J. Leek, A. Blais and A. Wallraff, *Nature* **454**, 315 (2008).

[111] P. Bertet, I. Chiorescu, G. Burkard, K. Semba, C. J. P. M. Harmans, D. P. DiVincenzo and J. E. Mooij, *Phys. Rev. Lett.* **95**, 257002 (2005).

[112] A. J. Leggett, *Progress of Theoretical Physics Supplement* **69**, 80 (1980).

[113] A. J. Leggett, *J. Phys.:Cond. Mat.* **14**, R415 (2002).

[114] M. H. Devoret, J. M. Martinis and J. Clarke, *Phys. Rev. Lett.* **55**, 1908 (1985).

[115] D. D. Awschalom, J. F. Smyth, G. Grinstein, D. P. DiVincenzo and D. Loss, *Phys. Rev. Lett.* **68**, 3092 (1992).

[116] K. C. Schwab and M. L. Roukes, *Physics Today* **58**, 36 (2005).

[117] A. K. Hüttel, G. A. Steele, B. Witkamp, M. Poot, L. P. Kouwenhoven and H. S. J. van der Zant, *Nano Letters* **9**, 2547 (2009). PMID: 19492820, http://pubs.acs.org/doi/pdf/10.1021/nl900612h.

[118] J. D. Teufel, T. Donner, M. A. Castellanos-Beltran, J. W. Harlow and K. W. Lehnert, *Nat. Nano.* **4**, 820 (2009).

[119] R. Miller, T. E. Northup, K. M. Birnbaum, A. Boca, A. D. Boozer and H. J. Kimble, *Journal of Physics B: Atomic, Molecular and Optical Physics* **38**, S551 (2005).

[120] S. M. Girvin, M. H. Devoret and R. J. Schoelkopf, *Physica Scripta* **2009**, 014012 (2009).

[121] Y. xi Liu, A. Miranowicz, Y. B. Gao, J. Bajer, C. P. Sun and F. Nori. "Qubit-induced phonon blockade as a signature of quantum behavior in nanomechanical resonators" (2009).

[122] A. Imamoğlu, H. Schmidt, G. Woods and M. Deutsch, *Phys. Rev. Lett.* **79**, 1467 (1997).

[123] S. Rebic, S. M. Tan, A. S. Parkins and D. F. Walls, *Journal of Optics B: Quantum and Semiclassical Optics* **1**, 490 (1999).

[124] K. M. Birnbaum, A. Boca, R. Miller, A. D. Boozer, T. E. Northup and H. J. Kimble, *Nature* **436**, 87 (2005).

[125] A. Wallraff, D. I. Schuster, A. Blais, L. Frunzio, R.-S. Huang, J. Majer, S. Kumar, S. M. Girvin and R. J. Schoelkopf, *Nature* **431**, 162 (2004).

[126] L. S. Bishop, J. M. Chow, J. Koch, A. A. Houck, M. H. Devoret, E. Thuneberg, S. M. Girvin and R. J. Schoelkopf, *Nat Phys* **5**, 105 (2009).

[127] A. Blais, R.-S. Huang, A. Wallraff, S. M. Girvin and R. J. Schoelkopf, *Phys. Rev. A* **69**, 062320 (2004).

[128] M. Wallquist, V. S. Shumeiko and G. Wendin, *Phys. Rev. B* **74**, 224506 (2006).

[129] C. A. Regal, J. D. Teufel and K. W. Lehnert, *Nat. Phys.* **4**, 555 (2008).

[130] T. Rocheleau, T. Ndukum, C. Macklin, J. B. Hertzberg, A. A. Clerk and K. C. Schwab, *Nature* **463**, 72 (2010).

[131] J. B. Hertzberg, T. Rocheleau, T. Ndukum, M. Savva, A. A. Clerk and K. C. Schwab, *Nat Phys* **6**, 213 (2010).

[132] D. Bozyigit, C. Lang, L. Steffen, J. M. Fink, M. Baur, R. Bianchetti, P. J. Leek, S. Filipp, M. P. da Silva, A. Blais and A. Wallraff. "Measurements of the correlation function of a microwave frequency single photon source", *arXiv:1002.3738v1* (2010).

[133] M. P. da Silva, D. Bozyigit, A. Wallraff and A. Blais. "Schemes for the observation of photon correlation functions in circuit qed with linear detectors", *arXiv:1004.3987v2* (2010).

[134] B. R. Johnson, M. D. Reed, A. A. Houck, D. I. Schuster, L. S. Bishop, E. Ginossar, J. M. Gambetta, L. DiCarlo, L. Frunzio, S. M. Girvin and R. J. Schoelkopf, *Nat Phys* **6**, 663 (2010).

[135] S. Rebić, J. Twamley and G. J. Milburn, *Phys. Rev. Lett.* **103**, 150503 (2009).

[136] K. Jacobs and A. J. Landahl, *Phys. Rev. Lett.* **103**, 067201 (2009).

[137] L. Tian, *Phys. Rev. B* **79**, 193407 (2009).

[138] M. O. Scully and M. S. Zubairy. *Quantum Optics* (1997).

[139] H. J. Carmichael. *Statistical methods in Quantum optics*, volume 1 (1998).

[140] Y. Makhlin, G. Schön and A. Shnirman, *Rev. Mod. Phys.* **73**, 357 (2001).

[141] L. Mandel and E. Wolf. *Optical Coherence and Quantum Optics* (1995).